EVALUATING THE FLEXURAL RESPONSE OF STEEL REINFORCED UHP-FRC BEAMS USING DISTRIBUTED SENSING

GIUSEPPE DOMENICO GARISTO

A THESIS SUBMITTED TO

THE FACULTY OF GRADUATE STUDIES

IN PARTIAL FULFILLMENT OF THE REQUIREMENTS

FOR THE DEGREE OF

MASTER OF APPLIED SCIENCE

GRADUATE PROGRAM IN CIVIL ENGINEERING

YORK UNIVERSITY

TORONTO, ONTARIO

DECEMBER 2023

Abstract

The interaction between the ultra-high-performance fibre-reinforced concrete (UHP-FRC) matrix and steel reinforcement with varying fibre contents and reinforcement ratios has a pronounced effect on the displacement ductility of UHP-FRC beams in flexure due to their influence on the spread plasticity along the steel reinforcement. Combining two ductile materials (steel and UHP-FRC) leads to a brittle failure mechanism due to crack localization. This is due to the bond mechanism and lack of strain penetration into the steel reinforcement away from cracks in UHP-FRC beams. Limitations in conventional point sensors such as strain gauges and external surface sensors such as digital image correlation (DIC) prevented prior research from fully studying this interaction. The emergence of distributed sensor technologies, namely, distributed fibre-optic sensors (DFOS), can provide the data required to study the effects of varying fibre content and reinforcement ratio on the displacement ductility of UHP-FRC beams in flexure. DFOS and strain gauges were used to study the distributed and discrete strains along the longitudinal reinforcement and top support wire while conducting four-point loading beam tests. The DFOS utilized Rayleigh backscattering based on optical frequency domain reflectometry (OFDR). Four beam specimens were tested with two fibre contents (v_f) (1% and 3%) and two reinforcement ratios (ρ) (1.5% and 2.3%). The quantity of fibres and steel reinforcement had an influence on the distributed strain readings along the longitudinal reinforcement, with a greater plastic length forming at a lower fibre content and reinforcement ratio. But the beam which consisted of a lower fibre content and higher reinforcement ratio demonstrated a more ductile behaviour in comparison to all the beam specimens, which was a result of an increase in curvature due to an overall higher peak tensile strain along the length of the beam. Crack localization was the predominant failure mode for the 3% fibre content beams, which led to a brittle failure long before compressive crushing. The 1% fibre content beams demonstrated more localized cracks and microcracking within the constant moment region, resulting more pronounced increases in the strain gradient which led to higher strain peaks. 2-dimensional finite element modelling was conducted in ATENA-GID to predict the behaviour of the experimental beam specimens using nominal UHP-FRC material properties at 28 days. The models provided an underestimation of the experimental response, requiring further improvements to the material properties in tension.

Acknowledgements

The past two years of my Masters were two of the most enjoyable and challenging years of my life, as I dedicated this time to studying a topic I am truly interested in. Most of my lessons were under the guidance of three of the professors who had the greatest influence on the trajectory of my academic career, since my undergraduate studies: Professor Pantazopoulou, Professor Butler, and Professor Gales. I would like to thank Professor Pantazopoulou and Professor Butler for their support and mentorship during these two years and for reinforcing my passion to learn. The knowledge and skills I gained from them surpassed what I developed during my entire undergraduate degree. They fundamentally reshaped my thought processes and problem-solving approach in engineering. Without their vast wisdom, the experimental program would have been much harder to implement successfully. A special acknowledgement goes to Professor Gales for providing his insightful perspective on issues regarding the experimental program. I would like acknowledge Professor Gales' influence on my academic career. It was his Civil Engineering Materials course during my second year which ignited my passion for structural engineering. From travelling to the Corktown Common and Queen Richmond Centre to take selfies for assignments to a fun and intriguing final exam, that Fall 2018 semester was one of the most enjoyable learning experiences I ever had. I express my deepest gratitude to Amer, Zoi, Ismail, Alex, Austin, Mario, Farah, Roberto, and Riad for their efforts in implementing the experimental program and sharing their invaluable knowledge.

Much of what carried me through the most challenging times over these past two years rests upon my friends and family. My Zio Franco, in particular, has been a significant influence, instilling upon me the value of learning and helping others with the knowledge I have acquired. I want to acknowledge my close friends JJ, Julius, Abraham, Sammy, Xavier, Placide, Jeff, and Justin. Their competitiveness and unwavering support have been instrumental in providing me with the will and drive to be better not only academically, but as a person. We have grown together, and their presence at every step has brought me to this point in my academic journey. Finally, I would like to thank everyone at the gym who showed support and took an interest in my research, being thankful would be a total understatement for how much that meant to me.

Table of Contents

List of Tables

List of Figures

Chapter 1: Introduction

1.1 Background

Reinforced concrete (RC) is currently the most prevalent material used in new infrastructure development. It is a composite material comprising of a conventional concrete matrix and strategically placed steel reinforcement to mitigate the effects of concrete's cracking under tension. Reinforced concrete components combine the advantageous qualities of the constituent materials which are complementary – e.g., slenderness of bars in compression is complemented by the robustness of concrete, whereas the poor performance of concrete in tension is complemented by the favourable tensile strength of the reinforcement. The brittle nature of concrete in tension and the formation of cracks encourages the onset of degradation due to the ingress of aggressive agents that can cause deterioration of steel reinforcement, carbonation, and spalling of concrete; directly impacting the service life of RC structures. As this has been going on for almost a century, the market for concrete repairs is extensive and it is expected to increase further as climate change exacerbates the implications of environmental exposure on structures. In 2021, the global concrete restoration market was valued at USD 15 billion and is projected to grow to USD 20.4 billion by 2026 (Market and Markets, 2022), projecting an increase in demand for repair measures. Accompanying the increasing cost of repair for RC structures, is their environmental impact. RC structures are built with the overconsumption of materials and natural resources, including fine and coarse aggregates, water, and cement in concrete and iron used in steel reinforcement. Approximately 8% of the global CO_2 emissions results from concrete production which uses up to one tenth of the global industrial water withdrawals (Miller et al., 2018).

The emergence of ultra-high-performance fibre-reinforced concrete (UHP-FRC) highlights the development of new prospects in construction that may in time bypass completely the shortcomings of the limited durability of conventional concrete structures. For one, owing to its spectacular strength, UHP-FRC enables leaner construction in terms of material usage, while the strain-hardening property of this class of materials in tension provides internal confinement and control of formation and propagation of cracking, thereby providing improved durability. The enhanced strength of UHP-FRC allows for the design of thinner and thus, lighter structural members, with reduced transverse reinforcement detailing. For some states of stress, this results in enhanced resistance to short-term and long-term loads, whereas the control of cracking enables prolonged service life for the structure, so that service times of 150 years or more may now be possible in RC Construction. However, there are several uncertainties in the structural performance of UHP-FRC where ductility is a driving consideration, as in the case of seismic loading or in limit states design, where plastic rotation capacity and formation of plastic hinges is a requirement. It is a paradox that by embedding ductile reinforcement in tension hardening (i.e., ductile) concrete, brittle response has been observed to occur, marked by localized reinforcement rupture. It is believed that this undesirable form of response is owing to the high bond that the UHP-FRC cover provides to the bars, which prevents the spread of strains beyond the crack locations and leads to localization of damage.

To study this type of response, and the extent to which deflections may be limited by the tensile strength and strain capacity of UHP-FRC, an experimental campaign was undertaken, where fibre-reinforced concrete matrices of different tensile stress-strain properties were considered. The beams were loaded in flexure under four-point loading and were reinforced with longitudinal reinforcement at two different ratios in order to observe the interaction of these two parameters (steel reinforcement ratio and concrete tensile hardening response) on the response of UHP-FRC flexural members. To facilitate close monitoring of the spread of inelasticity on the reinforcement in the critical region of maximum moment, distributed fibre-optic sensors were used to measure performance in terms of deformations or damage. Traditional instrumentation comprised point-wise installation of strain gauges and spring-loaded potentiometers, which however, can only provide measurements at discrete points. In the last few years digital image correlation (DIC) has been used to measure surface strains on concrete whereas recent advents in sensing technologies have resulted in the development of DFOS. DFOS have the capability of producing continuous measurements of mechanical and thermal strain, providing an innovative next step in the testing of materials and their implementation in structural engineering. This technology was used in the present study in order to monitor the reinforcement strains over the entire length of the structural specimens, which, combined with conventional instrumentation provided significant insights towards understanding how the bond in UHP-FRC matrices and steel reinforcement ratio together control the displacement ductility and mode of failure of the specimens.

1.2 Motivation of the Research

The primary motivation for this research is to further build upon the knowledge surrounding the interaction between the tension hardening characteristics of UHP-FRC, which are controlled by the volumetric fibre content, and the steel reinforcement ratio in the cross section – the maximum value of which is guided by the requirement of tension yielding prior to crushing in the compression zone of the member. It was stated earlier that this interaction may be interpreted through the effects of strain penetration and enhanced bond of reinforcement embedded in a UHP-FRC matrix, with consequent implications on the ductility that may be attained in the flexural behaviour of UHP-FRC beams.

It was noted in the introduction that combining a relatively ductile material such as UHP-FRC (in comparison to its predecessor in conventional concrete) with a ductile material such as steel reinforcement to develop reinforced UHP-FRC beams, results in an unexpected brittle failure. An inherent issue is imposed by the increase in tensile strength and corresponding bond strength between the cementitious matrix of UHP-FRC and steel reinforcement. Higher tensile strengths in UHP-FRC limit the distribution of cracks within the tensile zone of UHP-FRC beams. This results in crack localization – i.e., formation of only a few cracks of increasing width as the imposed deflection increases. Accompanying the higher tensile strengths of UHP-FRC is a corresponding increase in bond strength, which limits the "penetration" of reinforcement strain away from cracks. Reducing the number of cracks and the ability to distribute steel strains between cracks minimizes the spread of plasticity, causing severe damage to take place at localized points within the steel reinforcement. This prevents the favourable ductile behaviour with steel yielding near concrete crushing due to the premature rupturing of steel reinforcement. Decreasing the volumetric fibre content, and thus, the tensile strength and bond strength of UHP-FRC in combination with higher reinforcement ratios can lead to a more favourable ductile behaviour, providing significant warning before failure. The interaction between varying volumetric fibre content and steel reinforcement ratio is directly linked to plastic hinge formation and plastic hinge length, which are difficult properties to measure through experimental testing. The advancements made in sensing technologies such as DFOS provide the tools necessary to measure continuous strains along reinforcement lengths; thus, resulting in the opportunity to gather data pertaining to plastic hinge formation and plastic hinge length while considering the interaction between strain penetration and bond strength.

The use of UHP-FRC in structural and architectural elements is increasing. Engineers are able to design and develop smaller structural elements to resist greater loads, pushing the limits of material minimization with optimized performance. The current design code, namely the Canadian code, Annex A8.1 of CSA-S6 (2019), which specifies the requirements for the design of Fibre-Reinforced Concrete (FRC) structural elements requires further improvements to incorporate the latest findings of the current research. Specifically, further improvements are needed to the provisions pertaining to the flexural design process of UHP-FRC structural elements to define an appropriate reinforcement ratio domain that would secure adequate displacement ductility in UHP-FRC beams. The limited use of DFOS to measure steel strains in UHP-FRC beams under four-point loading tests highlights the opportunity that new sensing technologies provide, to further develop the knowledge and understanding obtained through prior research. This leads to the question of what is the key factor that leads to an increase in the displacement ductility UHP-FRC beams in flexure, whether it is the increase in strain magnitude, plastic length, strain penetration, or curvature; and how can DFOS be utilized to determine this? Therefore, the goal of this research is to provide further insights regarding the effects of varying fibre content and steel reinforcement ratio on strain penetration, the spread of plasticity in steel reinforcement, and the overall ductile response of UHP-FRC beams in flexure which could be considered in design.

1.3 Objectives and Scope of Thesis

Prior research has studied the effects of varying fibre contents and reinforcement ratios on the ductility of reinforced UHP-FRC beams. Primarily, they looked at the spread of plasticity using strain gauges along the length of longitudinal reinforcement. The sensor installation methods required to install strain gauges are quite intrusive, creating points of discontinuity over the concrete-bar interface, whereas the readings they provide refer to few discrete points. The scope of this research primarily explores the continuous (lengthwise) interaction between steel reinforcement and concrete, and its influence on bond and strain penetration using distributed strain data to capture the spatial impact of this interaction. By incorporating distributed strain measurements (i.e., every 2.6 mm), this research aims to provide novel insights that were not possible in past studies due to the limitations of the sensing technologies used.

The objectives of this thesis thereby include:

1. Further develop the understanding of the effects of varying fibre contents and steel reinforcement ratios on the ductile behaviour of UHP-FRC beams.
2. Providing insights relating to the spread of plasticity in the steel reinforcement of UHP-FRC beams with varying reinforcement ratios and fibre contents.
3. Exploring the effects of varying fibre contents on strain penetration of steel reinforcement.
4. Providing insights for which the current design code regarding the design of UHP-FRC members can use to further improve the provisions pertaining to flexural design.

1.4 Outline of Thesis

The thesis structure is composed of six chapters in the following format:

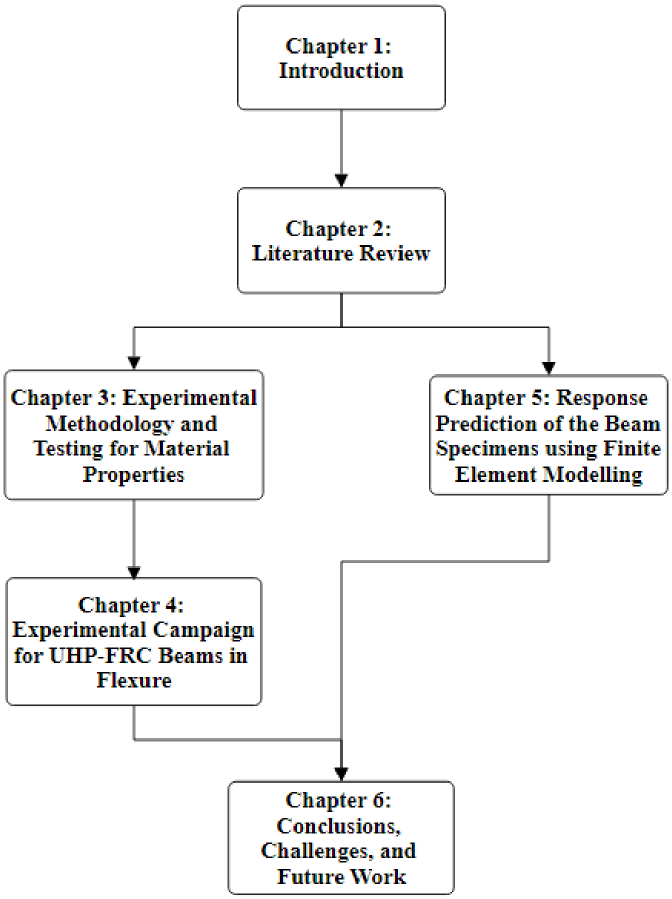

Figure 1-1. Thesis Structure

Chapter 1: Introduction provides a brief background to UHP-FRC and how its emergence addresses the current infrastructure needs resulting from using conventional RC elements. It further discusses the motivation of the performed research study and its corresponding objectives and scope.

Chapter 2: Literature Review assesses the current state of the Canadian, American, and European design codes regarding UHP-FRC flexural design. The characteristic behavior and material properties of UHP-FRC are discussed and their implications on the flexural behaviour and displacement ductility are outlined. Additionally, the chapter reviews the most relevant research regarding the interaction between volumetric fibre content and steel reinforcement ratio on flexural behaviour and context is provided as to how distributed fibre-optic sensing technology operates and can contribute to furthering the findings of these past studies.

Chapter 3: Methodology and Testing for Material Properties discusses the tasks required to complete the experimental research program. In this chapter, the methodology undertaken to construct the UHP-FRC beam specimens, the executed casting methods, and the testing of the material properties of the UHP-FRC mixtures and rebar used in the construction of the beam specimens.

Chapter 4: Experimental Campaign for UHP-FRC Beams in Flexure summarizes the experimental methodology undertaken to test the beams under four-point loading and the corresponding findings of the tests. This chapter highlights the load displacement results while correlating the strain data obtained through both the strain gauges and DFOS instrumented on the steel reinforcement. The results presented in this chapter are used to identify the effects of volumetric fibre content and steel reinforcement ratio on the ductile performance of UHP-FRC beams, through investigating the interaction between strain penetration and spread of plasticity in steel reinforcement.

Chapter 5: Response Prediction of the Beam Specimens using Finite Element Modelling provides the methodology and results of the finite element analysis which was conducted to predict the load-deflection response of the beams specimens prior to testing.

Chapter 6: Conclusions, Challenges, and Future Work summarizes the findings of the executed experimental campaign and finite element analysis. It describes the challenges faced during the undertaken research and the future work that can be conducted utilizing the findings of this thesis.

Chapter 2: Literature Review

The literature review provides an informative background on UHP-FRC, with emphasis on the current state of design standards and their implementation in flexural design. Additionally, this chapter explores the interplay between volumetric fibre content and various properties of UHP-FRC. The effect of fibre content is in flexural design and its impact in determining the appropriate reinforcement requirements to secure adequate ductile performance are studied. The chapter also presents a review of sensing technology applications - such as distributed fibre-optic sensors (DFOS), in measuring continuous strain data and assisting interpretation of the flexural response of reinforced UHP-FRC structural elements subjected to loading.

2.1 UHP-FRC Composition

UHP-FRC is a state-of-the-art construction material which is known for its high strength and durability. The foundation to its exceptional qualities rests upon several key elements: dense particle packing, low water-to-cementitious materials ratio (less than 0.25), (FHWA, 2018), reduced porosity, and most notably, the addition of fibre reinforcement. In standard proprietary design mixes, UHP-FRC comprises of fundamental constituents such as Portland cement, silica fume, metakaolin, and fly ash (Graybeal, 2013). Coarse aggregates are often excluded from UHP-FRC mixes to provide an enhanced particle packing, improve flowability, reduce permeability, and provide a more uniform/homogeneous material.

2.1.1 Steel Fibres

UHP-FRC's exceptional properties are attributed to the inclusion of distributed reinforcement in the form of steel fibres. The fibres augment the tensile and compressive strength, post-cracking tensile strain capacity, flexural strength, ductility, and overall durability. Furthermore, the fibers arrest crack propagation, prolonging the service life of reinforced concrete structures (Habel, 2004).

There are different types of steel fibres which are typically incorporated in UHP-FRC mixes, including straight fibres, hooked fibres, and twisted fibers. Predominantly, straight fibres are incorporated in UHP-FRC because of their larger surface area, which leads to improved bond with the cementitious matrix, greater shear resistance, reduced variability in mixing that leads to a more uniform distribution, and overall are simpler to produce. The steel fibres have a high modulus of elasticity in the order of 200GPa and a high tensile strength of around 2000MPa. Typical volumetric fibre contents, as defined by industry range between 2% to 5% to achieve tension hardening post-cracking behaviour of UHP-FRC.t Typical fibres are 5 mm to 30 mm long, whereas diameters range between 0.1mm and 0.5mm, with the ratio of the two being the aspect ratio (fibre length to fibre diameter).

2.2 Classification of UHP-FRC

UHP-FRC is classified by the material mechanical properties so that it could be relevant to design calculations. Compressive and tensile strengths are controlled by a multitude of factors including mix proportions, chemical admixtures, the inclusion of fibre reinforcement and their orientation, casting methods, and curing regime. Research has been conducted and some preliminary design guidelines are in place to aid in the material characterization for preapproval of the commercially available proprietary mixes so that these may be used in design. A commonly used classification system proposed by Naaman and Reinhardt (2006) for FRC composites considers the following types of behaviour: 1. Strain-hardening, 2. Strain-softening, 3. Deflection-hardening, and 4. Deflection-Softening. According to this classification, a strain-hardening material leads to deflection-hardening behaviour, whereas a strain-softening material can lead to both deflection-hardening and deflection-softening behaviour, with deflection-hardening behaviour a favourable property where bending dominates design (Naaman & Reinhardt, 2006).

Several standards are in place to impose classification systems similar to the scheme discussed by Naaman and Reinhardt (2006), to specify the quality of UHP-FRC being produced for structural engineering applications. Such standards include the Canadian and French provisons. The Canadian standard comprises CSA A23.1 Annex U (2019) "Materials and Methods of Construction" and CSA S6 Annex A8.1 (2019) "Structural Design of Bridges with FRC". The French Standard is organized into NF P 18-470 (2016), providing the rules for the selection of raw materials, testing methods, and quality control requirements to determine fresh and hardened properties and NF P 18-710 (2016), which provides the rules for structural design of civil engineering structures containing UHP-FRC.

2.2.1 Canadian Standard (CSA A23.1:19 Annex U, 2019), (CSA S6:19 Annex A8.1, 2019), (CSA S6:19 Annex A8.1 Commentary, 2019)

CSA A23.1:19 Annex U (2019) provides classification requirements for UHP-FRC. The minimum required compressive strength at 28 days for UHP-FRC is 120MPa UHP-FRC, for curing at ambient conditions (23±2°C, in > 95% relative humidity). Cylinder specimens for measuring the compressive strength are 75mm in diameter by 150mm height and are tested at a load rate of 1.0 ± 0.1 MPa/s. UHP-FRC is further characterized in tension as either strain-hardening or strain-softening, based on the results from flexural prism testing followed by inverse analysis, or direct tension tests. For UHP-FRC to be classified as strain hardening, it requires a cracking strength ($f_{t,cr}$) > 5MPa, hardening ratio ($f_{t,u}/f_{t,cr}$) > 1.1, and a minimum ultimate tensile strain ($\varepsilon_{t,u}$) > 0.1%. Furthermore, to be classified as tension-softening, UHP-FRC requires a cracking strength greater than 4 MPa. Following the AASHTO standard (AASHTO T397, 2022) for uniaxial testing of UHP-FRC, tension prisms have a 50mm square cross-section, 425mm length (with transfer plates), 100mm gauge length, and tested at a loading rate of 10 ± 3 MPa/min.

Figure 2-1 a) and b) display the multilinear stress-strain response of tension-softening and tension-hardening FRC materials. The tensile response curves for TSFRC and THFRC consist of the stress-strain domain and the stress-crack width domain, which are considered in separate aspects of design. The stress-strain domain considers the behaviour of FRC in tension prior to failure, and in the case of THFRC, the material can undergo large deformations and exhibit considerable energy absorption within this domain. The stress-crack width domain refers to the extent at which cracks can form in UHP-FRC after tensile failure or localization, which is important for meeting durability and serviceability requirements of structural members. CSA S6:19 Annex A8.1 (2019) defines limits to crack widths after failure, ensuring the integrity of structural members composed of UHP-FRC.

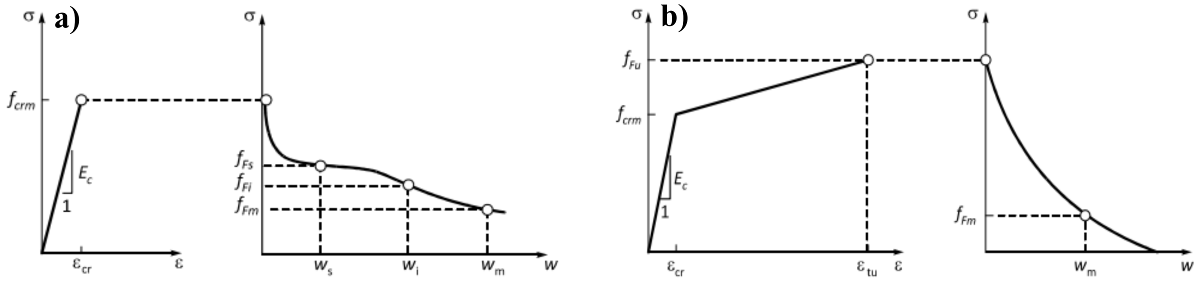

Figure 2-1. a) Tension-Softening Behaviour and b) Tension-Hardening Behaviour (CSA S6:19 Annex A8.1, 2019)

2.2.2 French Standard (AFNOR NF P 18-470, 2016), (AFNOR NF P 18-710, 2016)

The French standard, AFNOR NF P 18-470 (2016) provides the rules and requirements for determining the fresh and hardened properties of UHP-FRC. It provides classification of UHP-

FRC based on the durability and strength properties, with multiple categories of UHP-FRC ranging from compressive strengths of 130MPa (minimum compressive strength) to 250MPa. It classifies UHP-FRC as Type M for metallic fibres or Type A for other fibres (such as organic fibres). Strength requirements refer to the characteristic strength at 28 days, which is measured using 110mm (diameter) x 220mm (height) cylindrical specimens. Compressive strength classes include BFUP 130/145, BFUP 150/165, BFUP 175/190, BFUP 200/215, BFUP 225/240, and BFUP250/265 (first number refers to cylinder strength and second number refers to cube strength). AFNOR NF P 18-710 (2016) primarily considers the design of structures using a UHP-FRC with a compressive strength of 150MPa or greater, considering UHP-FRC with non-metallic fibres and compressive strengths lower than 150MPa to be unconventional. Thus, they are excluded from the scope of NF P 18-710; removing BFUP130/145, leaving five categories of UHP-FRC are specified with compressive strengths greater than 150MPa. There are three classes for UHP-FRC in tension based on the ratio of ultimate tensile strength to cracking strength ($f_{fctf}/f_{ct,el}$) similar to the Canadian standard. The three classes are as follows, considering a minimum value of the elastic limit (or cracking strength of 6 MPa at 28 days:

- T1 (strain-softening): $f_{fctf}/1.25<f_{ct,el}$ for mean and characteristic curves.
- T2 (limited strain hardening): $f_{fctf}/1.25\geq f_{ct,el}$ for mean curve but $f_{fctf}/1.25<f_{ct,el}$ for characteristic curve.
- T3 (significant strain hardening): $f_{fctf}/1.25\geq f_{ct,el}$ for both mean and characteristic curves.

2.3 Mechanical Properties of UHP-FRC

The enhanced mechanical properties of UHP-FRC have pushed the limits of structural design with cementitious materials, ushering a new era of design and innovation. This is with regards to strength, ductility, durability, and more. Mechanical properties such as compressive strength, elastic modulus, Poisson’s ratio, tensile strength, and hardening range are heavily influenced by the unique mixture designs for UHP-FRC and the addition of fibres. Significantly higher compressive strengths and stiffness are often attained with UHP-FRC in comparison to conventional concrete; the inclusion of fibres induces internal confinement which leads to lower values of Poisson’s ratio, higher tensile strengths after cracking with strain-hardening characteristics and improved ductility.

2.3.1 Compressive Strength

UHP-FRC attains a high compressive strength due to its high density and particle packing. The addition of steel fibres greatly increases the maximum tensile strain ductility and the corresponding tensile strength. As previously mentioned, the compressive strength required to classify a material as UHP-FRC varies according to different design codes. For instance, CSA S6:19 Annex A8.1 (2019) classifies UHP-FRC as a material with a minimum compressive strength of 120 MPa but is often capable of reaching strengths up to 200 MPa, with some materials exhibiting compressive strengths up to 250 MPa (Amran et al., 2022). The strain at peak compressive stress of UHP-FRC varies between 0.003 to 0.005 (FHWA, 2018), depending on factors such as mix design, curing conditions, and the inclusion of fibres. Shao & Billington (2019) reported concrete crushing strains up to 0.0065. UHP-FRC exhibits exceptional toughness prior to failure and a near linear stress-strain response up to peak stress, with softening occurring immediately after (Figure 2-2 a)), which is controlled by the quantity and type of fibre. Fibre content has a reduced influence on the compressive strength of UHP-FRC in comparison to its role in tensile behaviour. For instance, Figure 2-2 b) demonstrates there is an increase in compressive strength with an increase in steel fibre content, but the rate of increase is less pronounced for fibre contents higher than two percent.

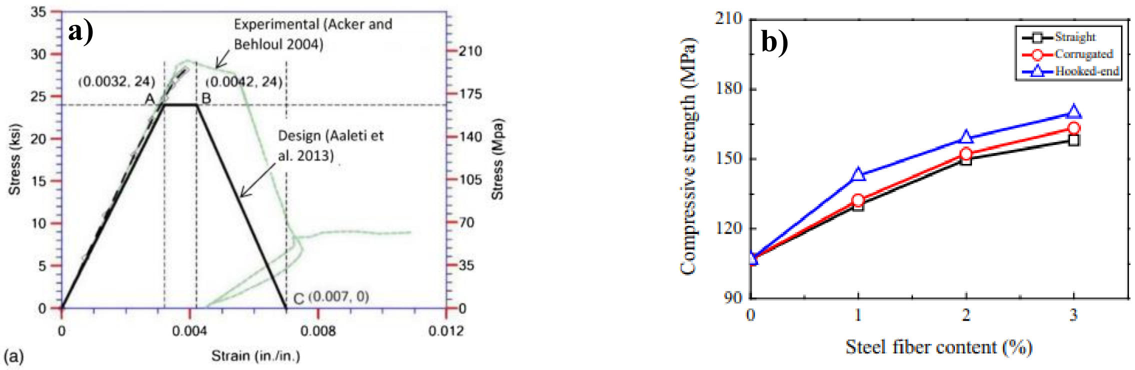

Figure 2-2. a) Compressive Behaviour of UHP-FRC (from Hung et al., 2021) and b) Compressive Strength vs Fibre Content (from Wu et al., 2016)

UHP-FRC develops a high early strength between 70 MPa to 95 MPa within the first 24 hours of curing (Hung et al., 2021). Compressive strength at 28 days is used as a benchmark for strength just as conventional concrete, but strength of UHP-FRC continues to develop well past this point (Figure 2-3 a)). Furthermore, UHP-FRC experiences a decrease in peak strain or localization strain as age increases (Figure 2-3 b)) corresponding to the material's increase in stiffness over time.

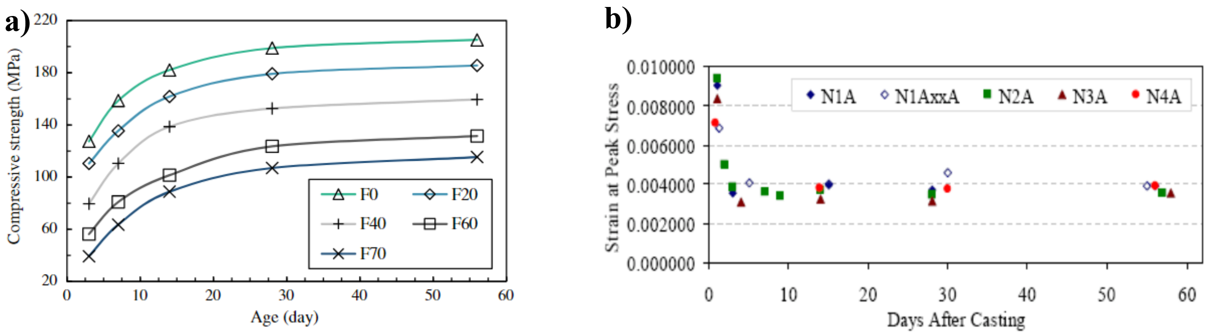

Figure 2-3. a) Compressive Strength vs Age (from Ahmed et al., 2021) and b) Peak Strain vs Age (from Graybeal, 2006)

2.3.2 Tensile Strength

UHP-FRC's superior tensile behaviour is a leading quality that has placed it at the forefront of materials-based research. UHP-FRC is classified as either tension-softening, exhibiting a decrease in tensile strength after cracking, or as tension-hardening, attaining an increase in tensile strength after cracking. Developments in UHP-FRC design mixes have shown tensile strengths greater than 20 MPa (Amran et al., 2022). Wille et al. (2014) demonstrated post-cracking tensile strengths up to 37 MPa, greatly exceeding that of conventional concrete, which fails in tension after cracking (occurring at approximately 4 to 8 MPa). Additionally, UHP-FRC has an exceptional ductility after cracking which is attributed to the inclusion of fibres. Figure 2-4 demonstrates the tensile behaviour of strain-softening (tension-softening) UHP-FRC and strain-hardening (tension-hardening) UHP-FRC. Strain-softening UHP-FRC exhibits a gradual decrease in load carrying capacity after crack localization with a single crack. Strain-hardening UHP-FRC develops higher tensile strength after initial cracking. Within the strain-hardening branch, UHP-FRC multiple cracks form up until the point of localization. During the hardening phase (or multiple cracking phase), UHP-FRC can be characterized by its stress versus strain tensile stress-strain response. After crack localization, and within the softening phase, UHP-FRC is characterized by stress versus crack opening values. The maximum crack opening in characterization standards is limited to ¼ of the characteristic length of the fibre.

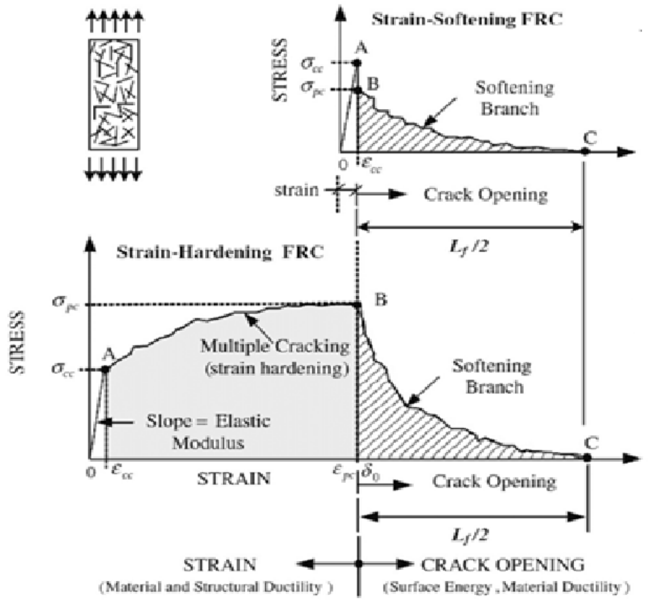

Figure 2-4. UHP-FRC in Tension (Adapted from Akeed et al., 2022)

Yang et al. (2022) conducted a series of tests on UHP-FRC prisms to study the effects of fibres on various mechanical properties of UHP-FRC. A portion of this study included studying the effects of varying the fibre content (between 0% and 3%) on the tensile parameters of UHP-FRC, including the initial cracking strength, the tensile strength, and the tensile strain at peak load. The study highlighted that increasing fibre content effected a more pronounced increase in the tensile strength and peak tensile strain as compared to the initial cracking strength as the fibre contribution increases after the initial cracking phase.

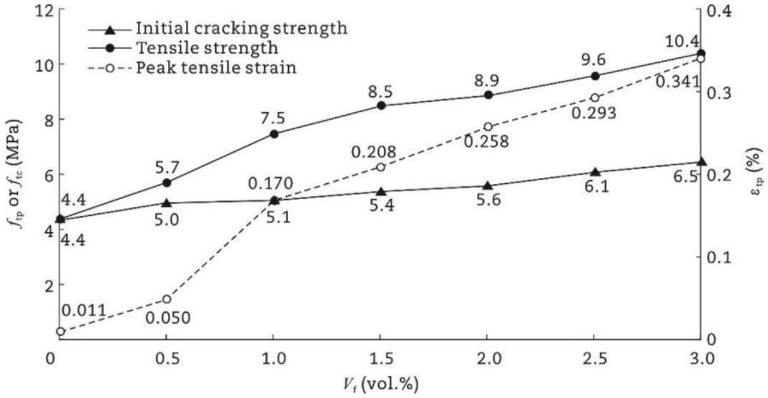

Figure 2-5. Effect of Fibre Content on Tensile Properties of UHP-FRC (from Yang et al., 2022)

Various testing methods for either direct or indirect characterization of UHP-FRC in tension have been proposed. These include direct tension tests (conducted on either prism or dog-bone shaped specimens), flexural prism tests, splitting tests, and punching; with the direct tension test being regarded as the better, but most difficult approach (Wille et al., 2014). These difficulties often result from a variety of factors which heavily influence the results achieved through direct tension tests, such as attaining an appropriate fibre dispersion within specimens, obtaining evenly distributed stresses throughout the cross-section of specimens, and appropriate gripping setup (boundary conditions).

A sample direct tension test setup is shown in Figure 2-6. (Voss et al., 2022) conducted direct tension tests following the FHWA method (Figure 2-6). Direct tension specimens used were 50mm by 50mm and consisted of tapered aluminum plates at the grips to avoid grip induced failure of the specimens. Furthermore, C-clamps were placed on the tapered portion of the aluminum plates (Graybeal & Baby, 2013) to evenly distribute the clamping force of the plates. A portion of the study included investigating the effects of varying the fibre content and fibre type on the tensile strengths measured through direct tension tests of UHP-FRC prisms. (Voss et al., 2022) reported that a slight misalignment led to a lower initial cracking stress, but if the material is strain-hardening, it compensates for the misalignment by bending and redistributing the load; these findings signify the sensitivity of results associated with conducting such tests.

Figure 2-6. Direct Tension Test Setup (From Voss et al., 2022)

2.3.3 Modulus of Elasticity

The elastic modulus, or Young's modulus, characterizes a material's stiffness and ability to undergo elastic deformation when loaded. UHP-FRC attains a high elastic modulus, surpassing that of conventional concrete. Research has consistently demonstrated that UHP-FRC exhibits an elastic modulus in the range of 30 GPa to 60 GPa (Figure 2-7). The inclusion of steel fibres is a key factor that influences the elastic modulus of UHP-FRC. Research has explored the effects of varying the fibre content on the elastic modulus of UHP-FRC. It has been observed that an increase in fiber content generally leads to an increase in the elastic modulus, which is attributed to the reinforcing capabilities of steel fibres that arrest the propagation of microcracks, enhancing the material's stiffness.

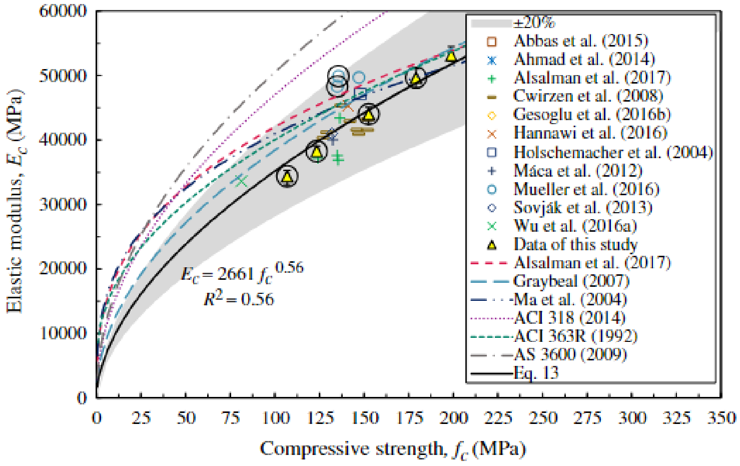

Figure 2-7. Relationship between Elastic Modulus and Compressive Strength (Ahmed et al., 2021)

In similar fashion to UHP-FRC compressive strength development with increasing age, the elastic modulus experiences a similar trend, with a higher rate of increase within the early phases of curing and a gradual plateauing. For instance, Figure 2-8 demonstrates a sharp increase in stiffness of various UHP-FRC mixes within the first 10 days after casting of the cylindrical specimens.

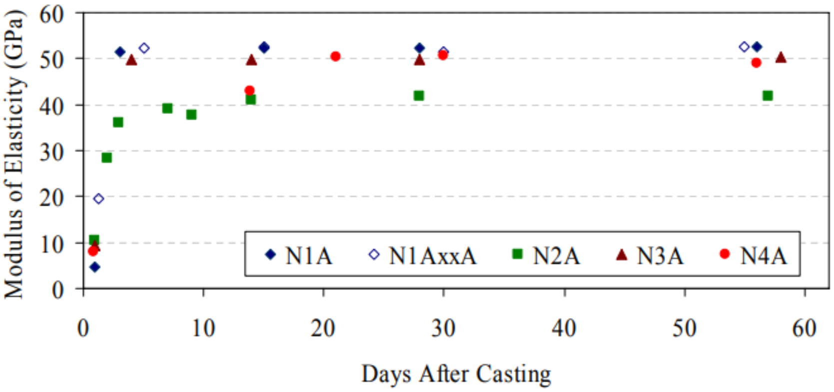

Figure 2-8. Elastic Modulus vs Age (Graybeal, 2006)

2.3.4 Poisson’s Ratio

Poisson’s ratio is the ratio of lateral strain to axial strain. For conventional concrete, Poisson’s ratio is between 0.15 to 0.25 (Popovics, 2008). Poisson’s ratio for UHP-FRC is slightly lower than that of conventional concrete, but still falls within this range. This is attributed to the mix design of UHP-FRC and the addition of fibres. Fibres induce confinement effects in UHP-FRC, restricting the lateral dilation of the material while it is axially loaded. Various studies were conducted to measure Poisson’s ratio for certain UHP-FRC mix designs. Table 2-1 shows a summary of data conducted from these studies demonstrating Poisson’s ratio for a given mix design being below 0.21, with an average value near 0.186. Another study by (Shehab El-Din et al., 2016) (Table 2-2) demonstrates Poisson’s ratio for a given mix design falling within the range of 0.19 to 0.21, with an average value of 0.199.

Table 2-1. Poisson's Ratio for UHP-FRC (Adapted from Graybeal, 2013)

Poisson's Ratio	Reference
0.2	Simon
0.16	Joh
0.21	Ahlborn
0.19	Bonneau
0.18	Graybeal
0.18	Ozyildirim

Table 2-2. Poisson's Ratio for UHP-FRC (Adapted from Shehab El-Din et al., 2016)

Group	Compressive Strength (MPa)	Modulus of Elasticity (GPa)	Poisson's Ratio
1	124	45.2	0.198
2	137	47.9	0.199
3	141	48.8	0.197
4	148	49	0.2
5	144	49.7	0.195
6	154	50.1	0.2
7	151	51	0.21

2.4 Bond Strength

Bond strength is the resistance to reinforcement slip in RC members. It is the combination of three contributors: 1. friction, 2. adhesion, and 3. interlock/bearing (Abed et al., 2021). Although adhesion and friction are present, they are quickly lost due to the decreasing diameter of steel reinforcement due to Poisson’s ratio. Therefore, the bond mechanism primarily relies upon the bearing of the concrete matrix on the ribs of steel reinforcement (Figure 2-9).

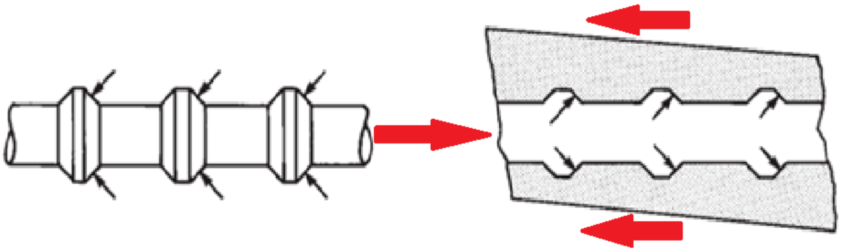

Figure 2-9. Bond Mechanism due to Interlock (Adapted from Wight & MacGregor, 2012)

Equations have been established to model bond strength and bond stress-slip relationship for conventional concrete (Equation 2.1 and Equation 2.2). Equation 2.1 is obtained from equilibrium of forces acting along a bonded length dx along a bar. It shows that bond stress is directly proportional to the change in tensile stress of the bar. Equation 2.2 defines slip as the relative translation between concrete and steel reinforcement. For conventional concrete, the tensile strain, ε_{ct} is neglected because of the low cracking strain of the material; this cannot be eliminated in the kinematics of a bar embedded in UHP-FRC due its relatively high tensile strain capacity.

$$\frac{df_s(x)}{dx} = -\frac{4}{D_b} f_b \tag{2.1}$$

$$\frac{ds(x)}{dx} = -(\varepsilon_s(x) - \varepsilon_{ct}(x)) \tag{2.2}$$

The general notion is that a higher tensile strength in UHP-FRC leads to a greater bond strength. For instance, Figure 2-10 illustrates the comparison of bond stress-slip behaviour for conventional concrete, concrete with spiral reinforcement, and HPFRCC. HPFRCC demonstrates a superior peak bond strength in comparison to conventional concrete. Steel fibres in FRC composites induce confinement effects in concrete, similar to adding passive reinforcement. Confinement effects have been shown to improve bond behaviour in reinforced concrete, as they reduce the expansion of concrete after cracking due to their crack bridging capabilities and provided that sufficient concrete cover is present.

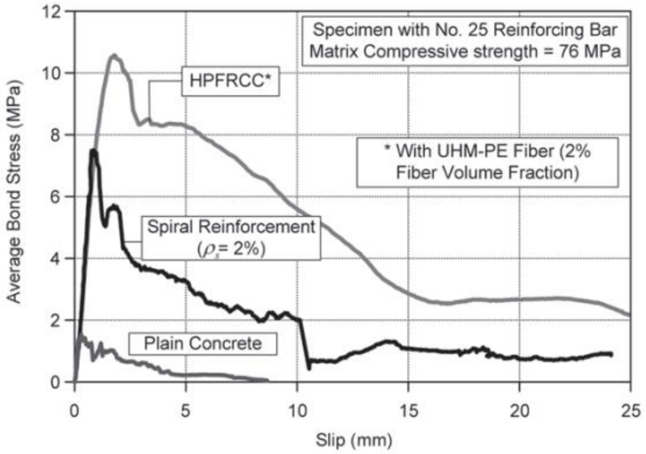

Figure 2-10. Comparison of Bond Stress-Slip Response under Monotonic Loading (Chao & Naaman, 2010)

In RC structural members, as cracking occurs, steel stresses are highest at the crack where concrete stresses are zero. Between the cracks, load is transferred to concrete through bond (Figure 2-11 a)). Looking at Figure 2-11 a), it is evident that bond stresses are directly proportional to the slope of the steel stress diagram. For instance, when the steel stress peaks, the bond stress is zero, and vice versa; hence, Equation 2.1. For FRC composites such as UHP-FRC, the stress distribution along an axially loaded prism considers the contribution of fibres at the cracks (Figure 1-1 b)).

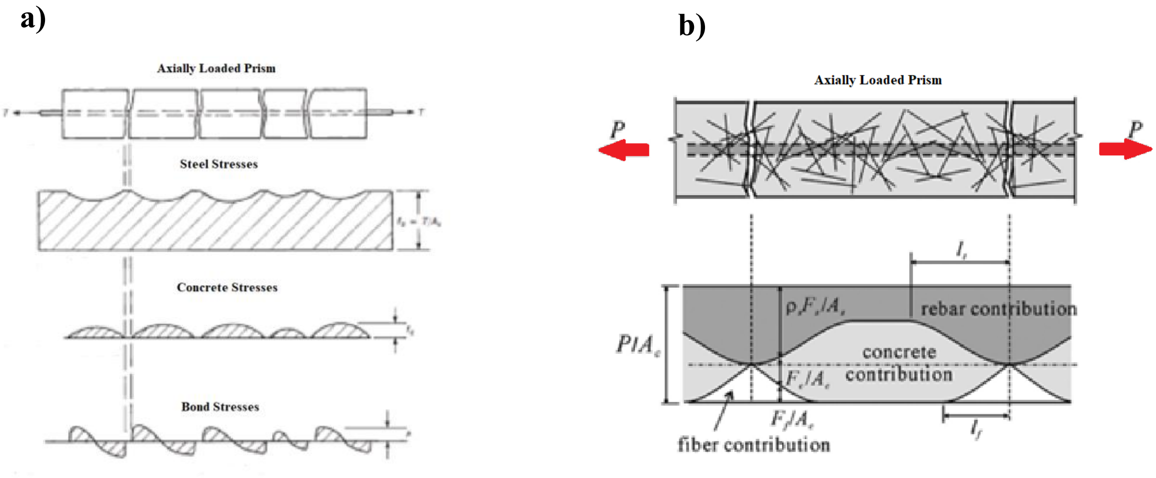

Figure 2-11. a) Stresses Acting in Cracked Prism of Conventional Concrete (Adapted from Wight & MacGregor, 2012) and b) Distribution of Stresses between Cracks in R/FRC (Adapted from Lee et al., 2013)

The analytical bond stress-slip relationship for RC shown in Figure 2-12 is separated into four phases, 1. ascending branch, 2. plateau, 3. descending branch, and 4. residual. Both cover splitting and yielding of reinforcement are associated with zero bond stress, which means that the reinforcement is de-bonded from the surrounding concrete cover. In the case of split cover, it cannot provide resistance to the bar slippage; in the case of the bar stress being within the yield plateau, the decreasing diameter due to the corresponding Poisson's ratio, aids in the debonding, whereas Equation 2.1 which is obtained from equilibrium can only be valid if f_b is zero to satisfy the requirement of the bar stress being constant and equal to f_y. The analytical bond stress-slip model in Figure 2-12 provides a fundamental reference point for which bond models for FRC and UHP-FRC are derived from.

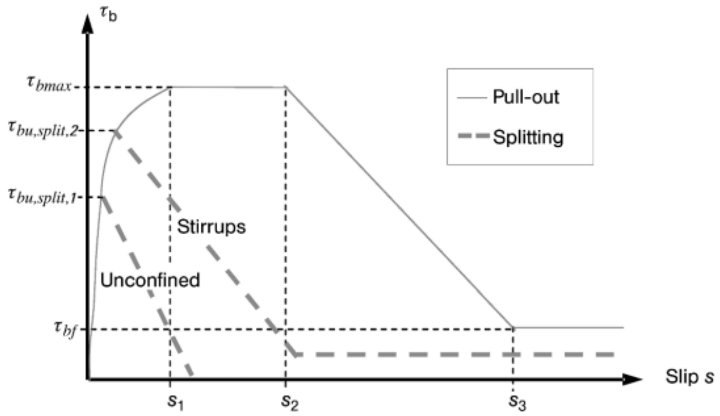

Figure 2-12. Analytical Bond Stress-Slip Relationship (fib Model Code, 2010)

2.5 Tension Stiffening

Tension stiffening is the ability for concrete to carry tension between cracks, which contributes to the stiffness of an RC structural member. It is a mechanism which relies on both the tensile strength and bond strength in RC. Tension stiffening effects are further amplified in R/FRC and R/UHP-FRC due to their enhanced tensile strength and bond strength, as illustrated in Figure 2-13. The figure demonstrates the differences in tensile behaviour of R/FRC in comparison to RC. After the RC member has cracked, its tensile response converges to that of the bare bar, with minimal increase in tensile strength and stiffness after yielding. Transitioning towards R/FRC and R/UHP-FRC, relatively higher tensile stresses can be resisted after cracking and yielding of reinforcement due to the contribution of the steel fibres.

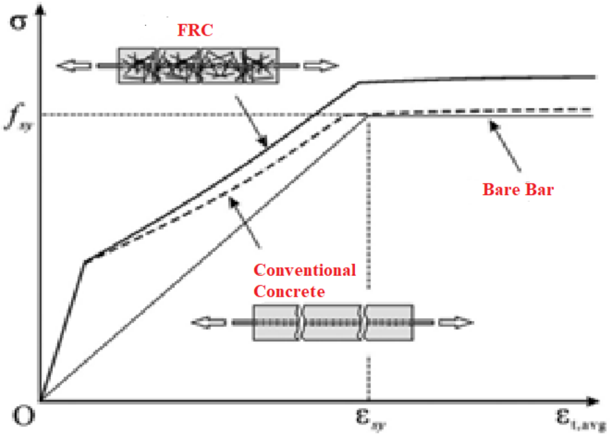

Figure 2-13. Tension Stiffening Effects in R/FRC and RC (Adapted from Lee et al., 2013)

Tension stiffening effects increase with higher reinforcement ratio for smaller diameter bars but decreases with higher volumetric fibre contents (Figure 2-14). This is because crack spacing localizes with an increase in fibre contribution (Lee et al., 2013).

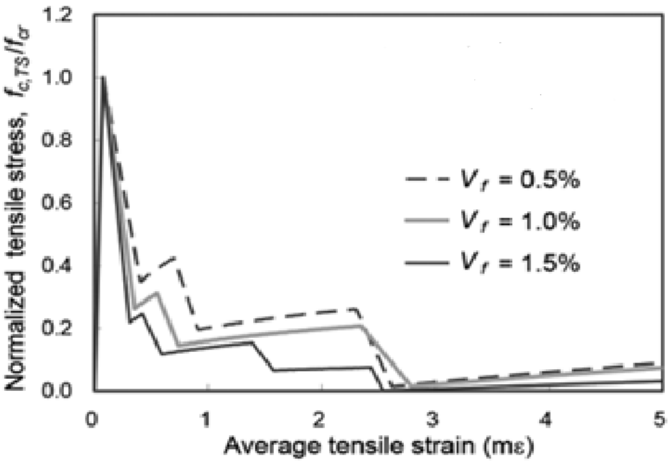

Figure 2-14. Numerical Results - Effect of Volumetric Fibre Content on Tension Stiffening (Adapted from Lee et al., 2013)

Lee et al (2013) developed a tension stiffening model for R/FRC structural elements using a crack analysis procedure which considers the tensile behaviour due to varying steel fibre contents and the bond-slip relationship between steel reinforcement and concrete matrix (Equation 2.3).

$$f_{c,TS} = \frac{f_{cr}}{1+\sqrt{(3.6C_f M\varepsilon_{t,avg})}} \qquad 2.3$$

(Lee et al., 2013)

Equation 2.3 shows the tension stiffening model developed by Lee et al (2013) which considers the effects of steel fibres using the following coefficients: c_f is the coefficient which considers the effects of steel fibres and M which is the bond parameter calculated from $M = A_c/(\Sigma d_b \Pi)$, where Π is the contact perimeter of the reinforcement. The higher c_f and M, the lower the tension stiffening effects of R/FRC members. c_f can be calculated using either Equation 2.4 for hooked fibres or Equation 2.5 for straight fibres, which signifies that increasing the fibre aspect ratio or volumetric fibre content, tensile strength, and decreasing the bond parameter, M, through higher reinforcement ratios comprising smaller bars, results in a greater fibre coefficient c_f.

$$c_f = 0.6 + \frac{1}{0.034}\frac{\left(\frac{l_f}{d_f}\right)\left(100V_f\right)^{1.5}}{M^{0.8}} \qquad 2.4$$

Hooked Fibres (Lee et al., 2013)

$$c_f = 0.6 + \frac{1}{0.058}\left(\frac{l_f}{d_f}\right)^{0.9}\frac{100V_f}{M^{0.8}} \tag{2.5}$$

Straight Fibres (Lee et al., 2013)

2.6 Flexural Design of UHP-FRC Beams (CSA S6:19 Annex A8.1, 2019), (CSA S6:19 Annex A8.1 Commentary, 2019)

CSA S6:19 Annex A8.1 (2019) provides provisions for the design of UHP-FRC beams in flexure for both TSFRC and THFRC. The basis of the flexural design process is to satisfy the ultimate limit state (ULS, or to ensure that $M_r \geq M_f$ while achieving satisfactory curvature ductility. Similar to designing RC beams in flexure using principles of mechanics, the same methods are applied to UHP-FRC beams with the addition of a tensile component on section equilibrium, contributed by concrete. At ULS, either a linear or equivalent rectangular stress block can be used to compute concrete compressive stresses along a cross-section. The compressive stress curve used for design depends on the value of strain being used, and on whether it is expected for the extreme compressive fibre within the elastic range (Figure 2-15 and Figure 2-16) or at the ultimate (Figure 2-17 and Figure 2-18). Two conditions are present for the tensile contribution of FRC: 1. Strain in the tension zone is less than the ultimate tensile strain of FRC (Figure 2-15 and Figure 2-17) and 2. Strain in the tension zone of the beam is greater than the ultimate tensile strain of FRC (Figure 2-16 and Figure 2-18). Once the tensile strain exceeds that of the ultimate value, the height of the stress block decreases starting from the extreme tension fiber.

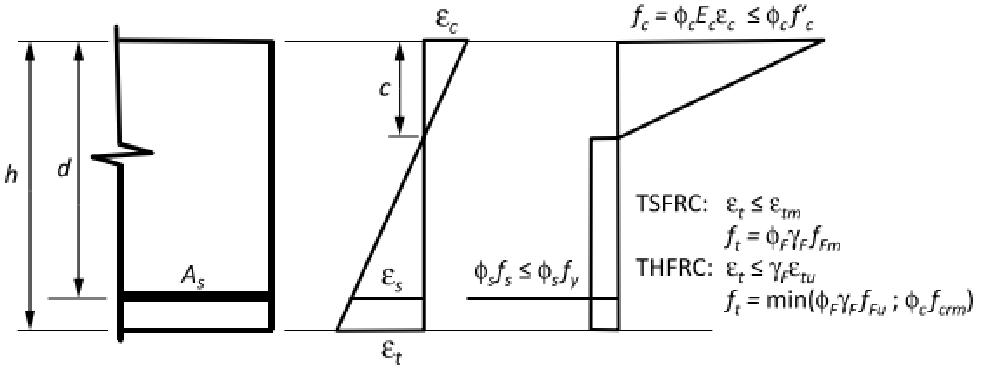

Figure 2-15. Elastic Compressive Stresses with Tensile Strain Below Ultimate (CSA S6:19 Annex A8.1 Commentary, 2019)

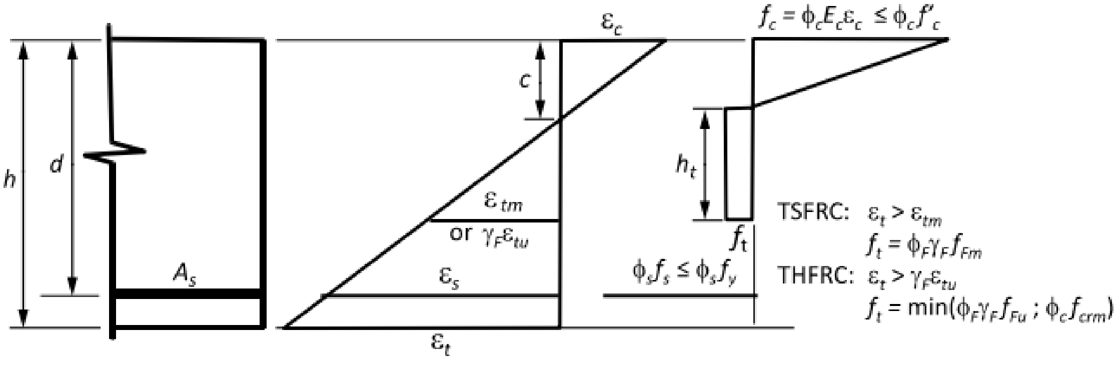

Figure 2-16. Elastic Compressive Stresses with Tensile Strain Beyond Ultimate (CSA S6:19 Annex A8.1 Commentary, 2019)

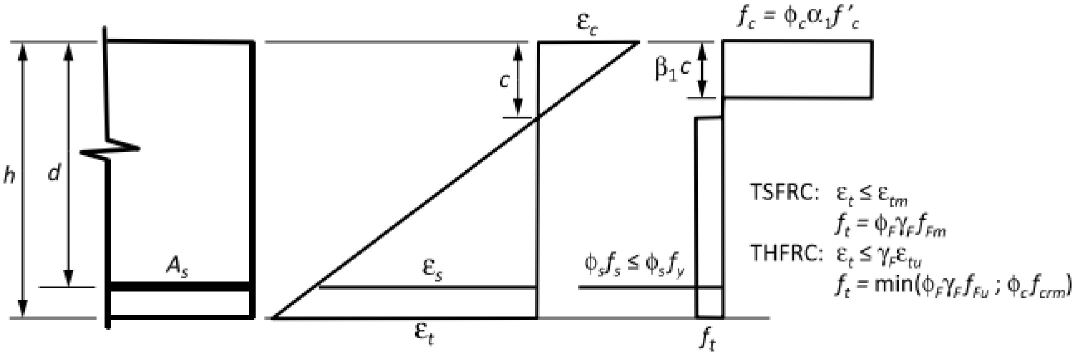

Figure 2-17. Plastic Compressive Stresses with Tensile Strain Below Ultimate (CSA S6:19 Annex A8.1 Commentary, 2019)

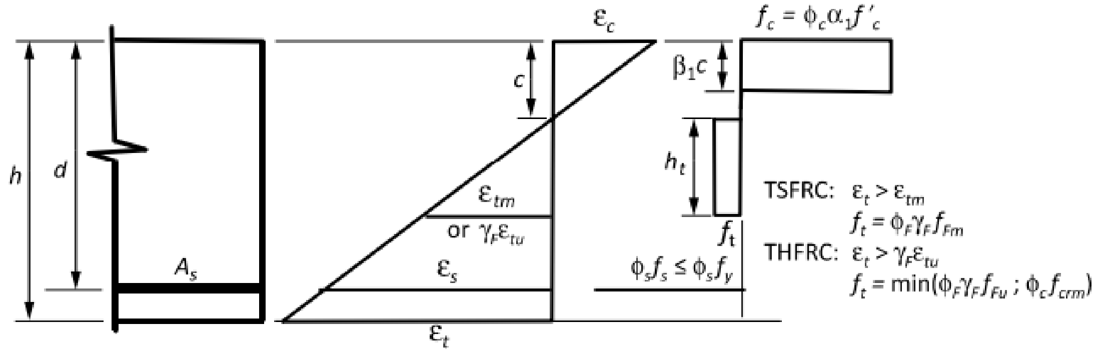

Figure 2-18. Plastic Compressive Stresses with Tensile Strain Beyond Ultimate (CSA S6:19 Annex A8.1 Commentary, 2019)

The flexural resistance is based on the calculation of three flexural resistance values: 1. M_{ry} at yielding of reinforcement, 2. M_{rm} when the extreme tension fibre reaches its ultimate value, and 3. M_{ru} when the extreme compression fibre reaches the ultimate compression strain. Figure 2-19 illustrates the factored flexural response incorporating the previously listed milestone points. A minimum curvature ductility ratio of 2.0 is defined to provide a minimum level of ductility. This is due to limitations in models to represent actual structural behaviour of UHP-FRC beams in flexure and to consider the simplification used in developing the design models. But, in some cases, the ductility ratio may need to be greater than 2, for instance, in scenarios where moment redistribution is considered. The following summarizes a recommended approach for determining the flexural capacity of UHP-FRC beams at ULS:

1. Calculate the flexural resistance, M_r and the corresponding curvature ψ at yield, at localization in tension, and when the extreme strain in compression reaches ultimate.
2. Determine the curvature ductility ratio which corresponds to the M_1, which is the maximum value of M_{ry}, M_{rm}, or M_{ru}. The curvature ductility ratio is taken to be $\mu=\psi_1/\psi_y$.
3. Determine the factored flexural resistance M_r:
   - $\mu \geq \mu_{min}$, $M_r=Max(M_{ry}; M_{r0})$
   - $\mu < \mu_{min}$, $M_r=Max(0.5M_1; M_{r0})$

   Where M_{r0} is the factored flexural resistance of the section without the contribution of fibres in tension.

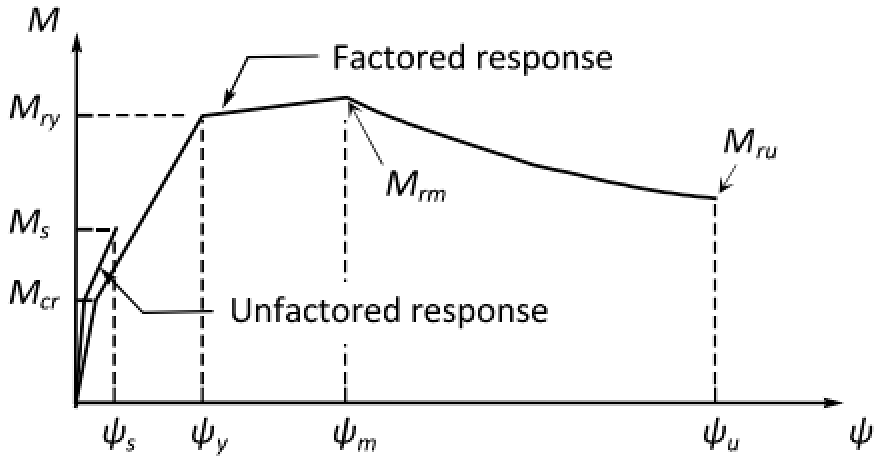

Figure 2-19. Factored Flexural Response (CSA S6:19 Annex A8.1 Commentary, 2019)

2.7 Longitudinal Reinforcement Requirements of UHP-FRC Beams in Flexure

The improved compressive strength, tensile strength, and ductility of UHP-FRC has transformed the design of RC structural members. This is especially evident in the design of UHP-FRC beams in flexure. RC structural members designed with conventional concrete consist of low reinforcement quantities to ensure tension-controlled behaviour (under-reinforced), with steel yielding prior to concrete crushing. Higher compressive strengths and strains have been achieved in UHP-FRC beams in flexure, changing the requirements for the under reinforced condition. Furthermore, as a byproduct of the high tensile strength and bond strength of UHP-FRC, crack localization poses an issue in the flexural behaviour and displacement ductility in UHP-FRC beams due to the minimal strain penetration which occurs away from cracks preventing the distribution of plasticity along longer beam lengths.

2.7.1 Tension-Controlled Behaviour in UHP-FRC Beams

The ultimate crushing strain of concrete in compression (ε_{cu}) used in design to define the requirements of tension-controlled behaviour is often taken to be 0.0035, which is specified in CSA S6:19 Annex A8.1 (2019) and ACI 239 (2018); not fully utilizing the compressive ductility of UHP-FRC which cannot precede in practice the occurrence of tension-controlled failure. Shao & Billington (2019) measured crushing strains up to 0.0065 in UHP-FRC beams, far exceeding the design value of 0.0035. Furthermore, Chao et al., 2019 conducted four-point loading beam tests on both RC and R/UHP-FRC beams to study the possibility of transitioning from prestressed concrete beams comprising conventional concrete to reinforced concrete beams composed of

UHP-FRC. A component of the study consisted of measuring concrete strain at the extreme compressive fibre and tensile strain at the level of reinforcement using DIC. The study demonstrated that at peak load, the compressive strain in the R/UHP-FRC specimen (Figure 2-20 b)) was nearly ten times that of the RC specimen composed of conventional concrete (Figure 2-20 a)), signifying that R/UHP-FRC required a considerable increase in longitudinal reinforcement to achieve a tension-controlled behaviour (Chao et al., 2019).

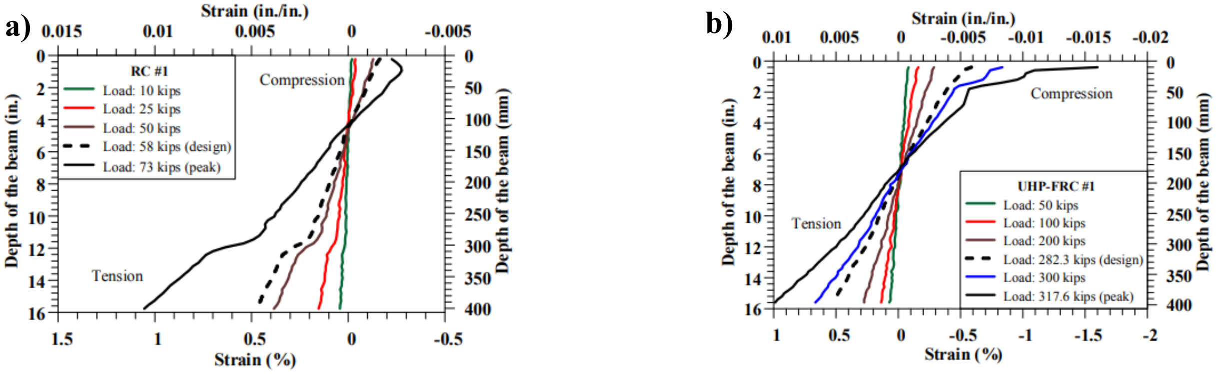

Figure 2-20. a) Strain Profile of RC Specimen and b) Strain Profile of R/UHP-FRC Specimen (Chao et al., 2019)

The greater amounts of reinforcement would lead to a corresponding decrease in reinforcement stresses, which would aid controlling cracks. Additionally, larger reinforcement ratios lead to greater tension-stiffening effects in reinforced structural members. By increasing the reinforcement quantities and thus, decreasing the reinforcement stresses at a given load, there is a corresponding restraint in the growth of crack widths due to the relationship between crack width and reinforcement stress.

As previously mentioned, Shao & Billington, 2019b studied the effect of increasing reinforcement ratio in R/UHP-FRC beams, in seeking to utilize the available compressive strength of UHP-FRC. Two tension reinforcement ratios were considered in the study, i.e., 0.96% and 2.10%. The specimen consisting of a reinforcement ratio of 0.96% failed in a brittle manner, with reinforcement rupturing significantly prior to concrete crushing. Figure 2-21 that compressive crushing did not occur in the 0.96% reinforcement ratio beam, illustrating the great reserves of compressive strength in the compression zone and the ductility of the UHP-FRC material. The specimen consisting of the 2.10% reinforcement ratio failed after gradual strain hardening in the load displacement envelope, with crushing of concrete in compression at peak load (Figure 2-22).

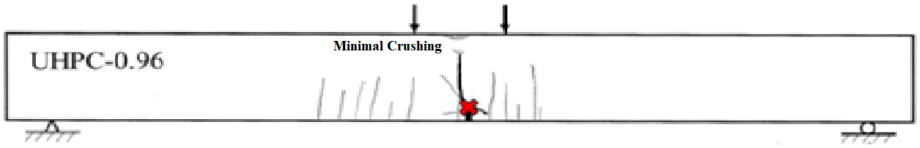

Figure 2-21. No Compressive Damage at Peak Load (Adapted from Shao & Billington, 2019b)

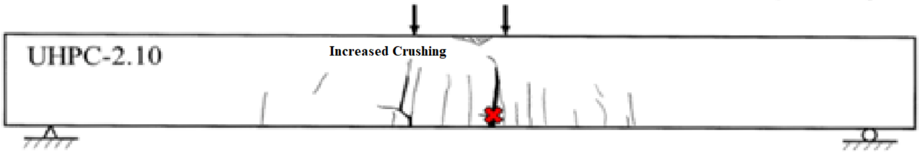

Figure 2-22. Compressive Crushing at Peak Load (Adapted from Shao & Billington, 2019b)

2.7.2 The Effect of Tensile Behaviour on UHP-FRC Beams in Flexure

Click or tap here to enter text.Strain-hardening (or tension-hardening) UHP-FRC is prone to crack localization, which signifies the onset of failure of UHP-FRC in tension. Crack localization is the phenomenon where cracks in a material become concentrated in a localized region rather than spreading uniformly along a length. The corresponding implications of such behaviour are severe, such as the localization of damage and induced stress concentrations in steel reinforcement in R/UHP-FRC structural members. Due to the high tensile and bond strength of UHP-FRC, strain penetration of steel reinforcement away from cracks is significantly reduced, inducing stress concentrations at localized cracks. The formation of localized cracks reduces the distribution of plasticity along beam lengths, causing the formation of plastic hinges at localized cracks. With plasticity forming within a small zone of a beam, the high stress formation in steel reinforcement leads to premature rupturing of steel reinforcement prior to concrete crushing, leading to an unfavourable brittle failure mode in R/UHP-FRC beams.

Shao & Billington (2022) demonstrated that by reducing the volumetric fibre content of UHP-FRC mix designs and increasing the steel reinforcement ratio in R/UHP-FRC beams, a favourable ductile response may be achieved, with noticeable deflections prior to failure. The reduction in fibre content leads to a weaker UHP-FRC material in tension, avoiding the issue of crack localization. Pokhrel et al. (2021) further demonstrated that the length of both major in minor cracks significantly increases when reducing the volumetric fibre content from 2% (Figure 2-24) to 1% (Figure 2-23). Although decreasing the fibre content increased the crack spacing, it showed little to no effect on crack widths (Shao & Billington, 2022).

Lower tensile strengths in UHP-FRC allow for a more distributed crack pattern along reinforced beam lengths, spreading plasticity along the length of a beam rather than at a localized spot. The increase in reinforcement ratio reduces the stress in steel reinforcement at the cracks, delaying the onset of plasticity towards when concrete crushing commences leading to a more brittle response. Figure 2-25 displays the load-drift response of R/UHP-FRC beams with varying fibre contents and reinforcement ratios. The main observation is that it is more effective to promote ductility in the reinforced beam response, to combine a lower fibre content and a higher reinforcement ratio For instance, Figure 2-25.a) shows that using a lower reinforcement ratio 0.96% and a fibre content of 2% leads to failure after crack localization. Figure 2-25 e) shows that a higher reinforcement ratio of 2.10% and a lower fibre content of 1%, leads to a gradual increase in load after crack localization.

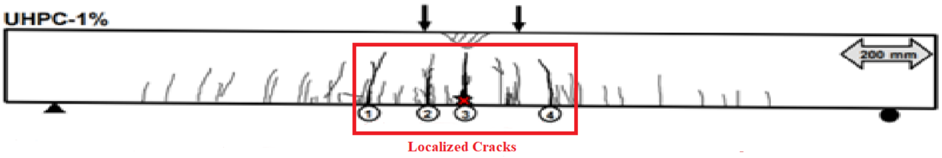

Figure 2-23. Crack Pattern in UHP-FRC Beam with 1% Fibre Content (Adapted from Pokhrel et al., 2021)

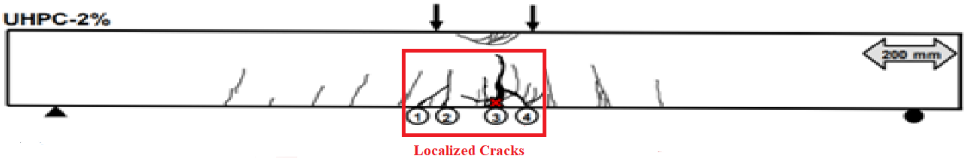

Figure 2-24. Crack Pattern in UHP-FRC Beam with 2% Fibre Content (Adapted from Pokhrel et al., 2021)

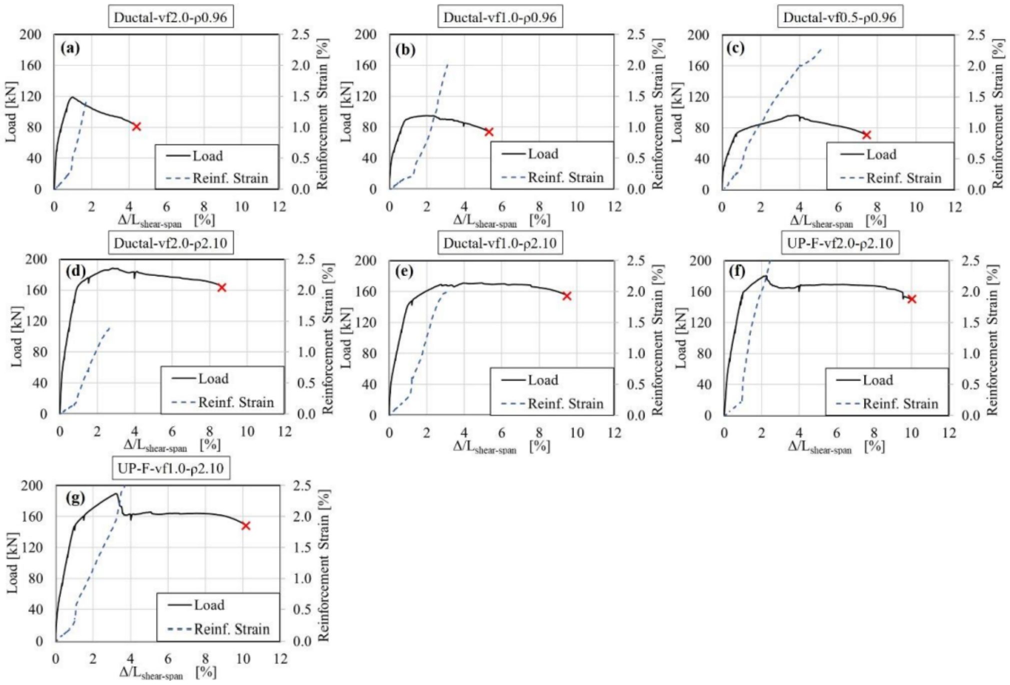

Figure 2-25. Load-Drift Response and Reinforcement Strain History of UHP-FRC Beams with Varying Fibre Content and Reinforcement Ratio a) Ductal-vf2.0-ρ0.96, b) Ductal-vf1.0-ρ0.96. c) Ductal-vf0.5-ρ0.96, d) Ductal-vf2.0-ρ2.10, e) Ductal-vf1.0-ρ2.10, f) UP-Fl-vf2.0-ρ2.10, g) Ductal-vf1.0-ρ2.10 (Shao & Billington, 2022)

Shao & Billington (2022) concluded that by increasing the post-yield strain hardening capacity of steel reinforcement, increasing the reinforcement ratio, or decreasing the load carrying capacity of UHP-FRC in tension, failure occurs after gradual strain hardening. This is summarized in Equation 2.6, which considers the ratio of the load carrying capacity of steel reinforcement to that of UHP-FRC. Shao & Billington (2022) developed an equation for a ratio, ω, can be used to determine if a UHP-FRC beam will demonstrate a brittle failure mechanism or demonstrate ductile behaviour. ω is defined by the ratio of the load carrying capacity if steel to the load carrying capacity of UHP-FRC in tension multiplied by the ratio of the effective depth and reinforcement ratio to the total height of the beam.

$$\omega = \frac{(f_{su} - f_{sy})A_s}{\alpha A_c f_t} = \frac{(f_{su} - f_{sy})A_s}{\alpha b h f_t} * \frac{d}{d} = \frac{(f_{su} - f_{sy})}{\alpha f_t} * \frac{d}{h}\rho \qquad 2.6$$

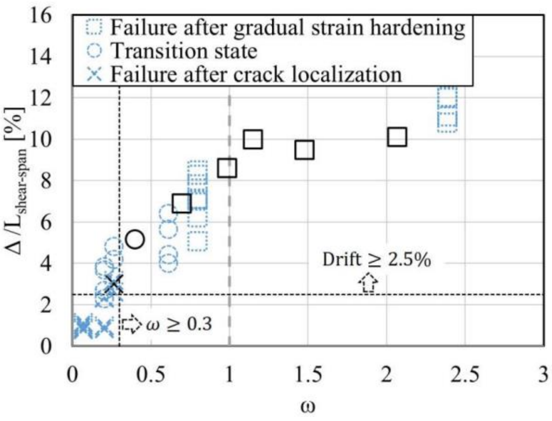

Figure 2-26. Drift Capacity vs ω (Shao & Billington, 2022)

Figure 2-26 illustrates that at higher values of ω, higher drift capacities at peak load are attained. Furthermore, it highlights that lower values of ω result in failure after crack localization. Limiting the value of ω to be greater than 1 is recommended to avoid crack localization and achieve ductile behaviour with failure occurring after gradual strain hardening in steel reinforcement.

2.7.3 Plastic Hinge Formation with Varying Fibre Contents

As mentioned in the prior section, there is a correlation between varying fibre content and the spread of plasticity in longitudinal reinforcement in UHP-FRC beams in flexure. The increased distribution of cracking when decreasing fibre content leads to plastic hinges forming at various locations along a beam's length, allowing for gradual strain hardening of the longitudinal reinforcement. Pokhrel et al. (2021) studied the effect of varying fibre content on plastic hinge formation in UHP-FRC beams. The study consisted of two doubly reinforced UHP-FRC beams with a single reinforcement ratio of 2.10% and two fibre contents of 1% and 2%. Five strain gauges were installed on the beam specimens, with one strain gauge at midspan, another strain gauge beneath the applied point load, and three strain gauges just outside the constant moment region spaced at 50mm (Figure 2-27).

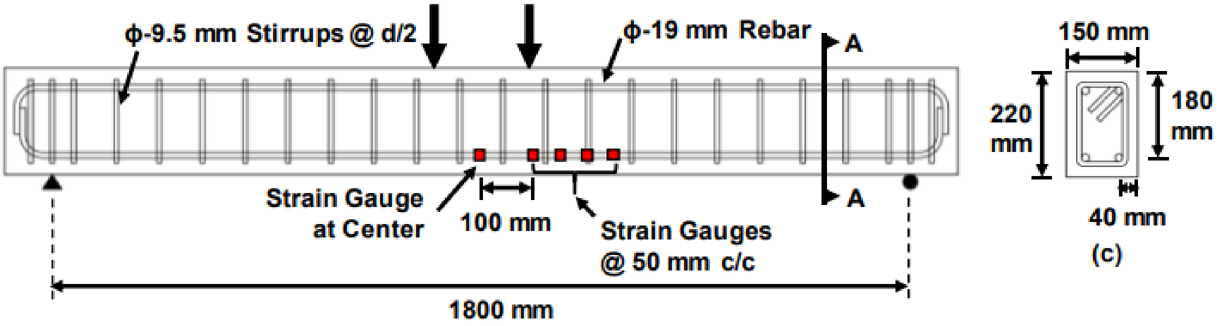

Figure 2-27. Instrumentation of Test Beam (Pokhrel et al., 2021)

During testing, strain readings were obtained at various drift levels. Figure 2-28.a displays the strain readings for the 1% fibre content beam specimen. At 8% drift, the yield length L_{py} was 290mm, whereas, in the 2% fibre content beam specimen, L_{py} was 230mm (Figure 2-28.b) suggesting that plastic hinges in beams with higher tensile strength and bond strength consist of smaller plastic hinge lengths than those with weaker tensile and bond parameters.

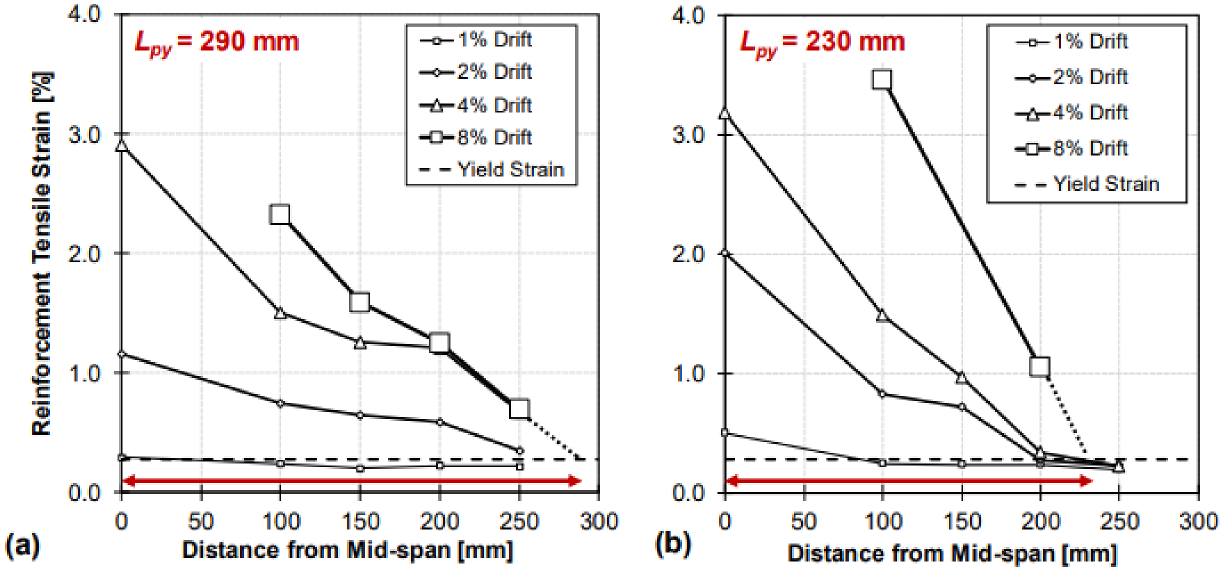

Figure 2-28. Reinforcement Strain vs Length a) 1% Fibre Content b) 2% Fibre Content (Pokhrel et al., 2021)

2.7.4 Defining an Appropriate Reinforcement Ratio

In light of the findings provided by Pokhrel et al. (2021), Shao & Billington (2022), and Chao et al. (2019), along with the improved properties of UHP-FRC including compressive strength, tensile strength, bond strength, and tension-stiffening effects, the requirements for flexural design of UHP-FRC beams have been altered. Higher reinforcement ratios are possible with the ability of the UHPFRC compression zone to be able to support high forces. Click or tap here to enter text.Equation 2.6 provided the bounds of minimum tolerable steel overstrength to avoid post cracking strength loss in the beam after the tensile contribution of the UHPFRC is lost; maximum amounts of steel reinforcement are linked to the so-called balanced failure, i.e., when compression crushing occurs at the onset of tension reinforcement yielding, which would constitute an undesirable type of response.

Husain (2021) defined a reinforcement ratio domain for R/UHP-FRC beams in flexure. This was with reference to a CPCI girder as seen in Figure 2-29. This included defining a model for minimum reinforcement ratio ρ_{min}, balanced reinforcement ratio $\rho_{s,bal}$, and the reinforcement ratio ρ_s within their enclosed domain. The equations were developed by establishing sectional equilibrium using the equivalent stress block approach for compression and tension (Figure 2-30). This method assumes tensile strength to be a function of compressive strength, where compressive strength is reduced by a factor, γ, to generate the tensile strength and corresponding stress block in tension. Husain (2021) defines γ to be between 5% and 20% of f'_c. Therefore, for the minimum compressive strength of 120MPa to be considered UHP-FRC (CSA S6:19 Annex A8.1, 2019), the corresponding minimum tensile strength would be 6MPa ($0.4\sqrt{f'c}$) Doing so required the use of an ultimate compressive strain of 0.0035 which is consistent with the recommendations of ACI 239 (2018) and CSA S6:19 Annex A8.1 Commentary (2019). Thus, maintaining α_1 and β_1 parameters Equations 2.7 and 2.8 which are limited to a compressive strength of 120MPa are defined.

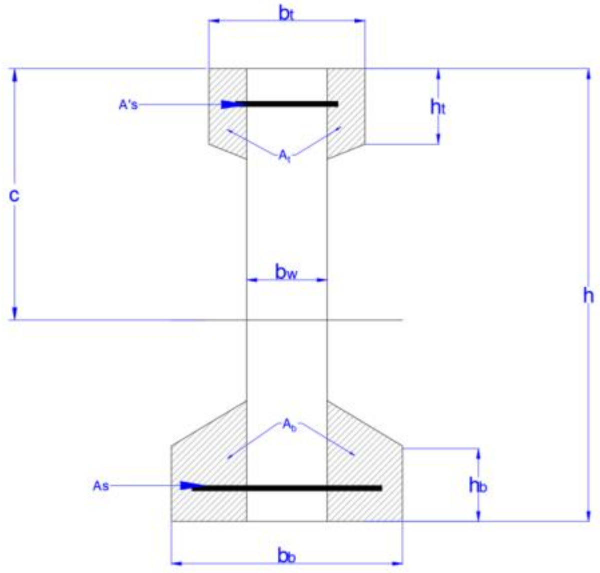

Figure 2-29. CPCI Girder Section Components (Husain, 2021)

$$\alpha_1 = 0.85 - 0.0015f'c \geq 0.67 \qquad 2.7$$

$$\beta_1 = 0.97 - 0.0025f'c \geq 0.67 \qquad 2.8$$

Parameter ρ_{min} (Equation 2.9) considers the condition of steel yielding when the extreme tension fibre reaches the ultimate tensile stress for UHP-FRC. The load contribution of UHP-FRC in tension and yielding of steel reinforcement is limited to being less than the ultimate strength of steel to ensure there is not a reduction in flexural strength of the beam when UHP-FRC has failed in tension.

$$T < T_{su}$$

$$f_t(A_b + (h-c)b_w) < A_s, \min\,(f_{su} - f_{sy})$$

$$A_s, \min > \frac{f_c\lambda}{f_{su} - f_{sy}}(A_b + (h-c)b_w)$$

$$\rho_{min} > \frac{f_c\lambda}{f_{su} - f_{sy}}\frac{(A_b + (h-c)b_w)}{A_{tot}} \qquad 2.9$$

Term ρ_s (Equation 2.10) is determined through equilibrium of forces within the cross-section of the member, considering steel yield has yielded and the ultimate strength of UHP-FRC in tension. This leads to reinforcement ratio, ρ_s, being directly proportional to depth of the neutral axis. $\rho_{s1,bal}$ (Equation 2.11) is determined in similar fashion as ρ_s, with the main difference being that the depth of the neutral axis, c, must be calculated for the balanced condition with steel yielding at concrete crushing. The combination of ρ_{min}, ρ_s, and $\rho_{s1,bal}$ define a domain of reinforcement ratios for a given depth of the neutral axis, a precursor to developing design tables for UHP-FRC in flexure.

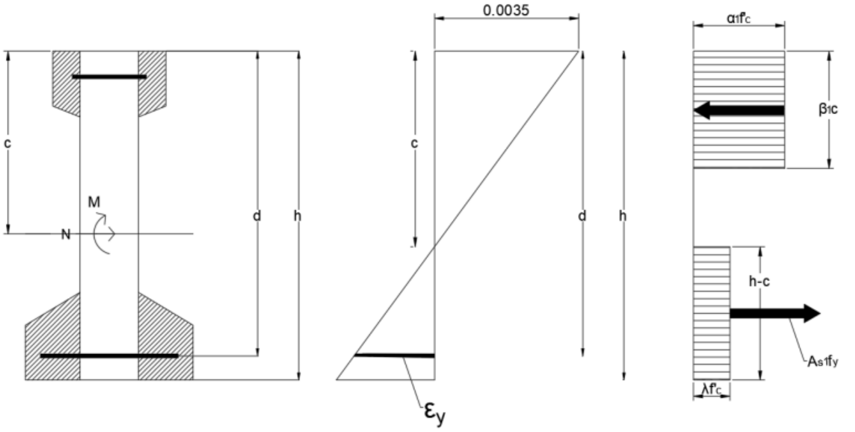

Figure 2-30. Definition of Terms for Sectional Equilibrium (Husain, 2021)

$$\Sigma F_x = 0$$

$$0 = \alpha_1 \beta_1 c - N - \lambda f'c(h - c)b$$

$$\rho_s = \left[\frac{\alpha_1 \beta_1 c}{d} - \lambda\left(\frac{h}{d} - \frac{c}{d}\right)\right]\frac{f'c}{f_{sy}} \qquad 2.10$$

$$\rho_{s1,bal} = \left[\frac{\alpha_1 \beta_1 c_{bal}}{d} - \lambda\left(\frac{h}{d} - \frac{c_{bal}}{d}\right)\right]\frac{f'c}{f_{sy}} \qquad 2.11$$

2.8 Background to Distributed Fibre-Optic Sensing

Fibre-optic technology was developed in the 1950s and has been the backbone of our communications infrastructure since the 1970s (Culshaw & Kersey, 2008). It relies on transmitting information/data as pulses of light through a glass cable. Figure 2-31 illustrates the typical structure of an optical fibre. The core at the centre of the optical fibre is composed of silica. This is where most of the light travels through. The region directly outside the core is called cladding, which has a lower index of refraction than the core to ensure light confinement. The entrapped light in the core travels along the sensor by reflecting off at the interfaces with the cladding, a process referred to as total internal reflection (Figure 2-32).

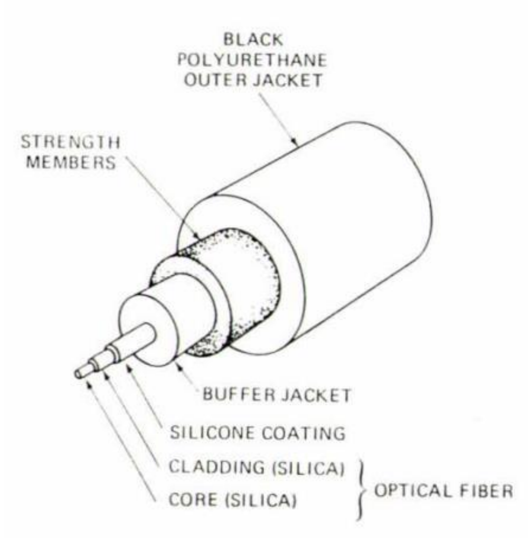

Figure 2-31. Components to Optical Fibre (Micron Optics, n.d.)

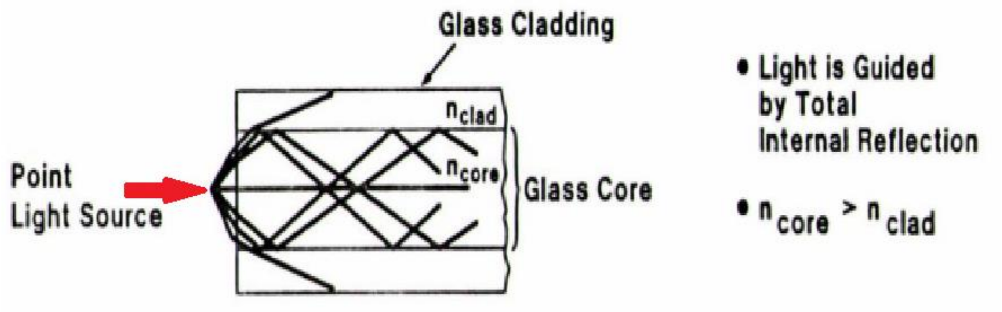

Figure 2-32. Basic Concept of Fibre-Optics (Adapted from Micron Optics, n.d.)

Advancements have been made in fibre-optic technology, eventually leading to its use for sensing applications. In particular, fibre-optic based sensors are now being used for structural health monitoring purposes (SHM), to monitor the performance of structures during their service life and to provide the means to diagnose damage. One such technology in measuring structural performance is the distributed fibre-optic sensor (DFOS), which has the capacity to measure distributed strain along a given length of fibre optical cable. DFOS primarily relies on three scattering phenomena, including Brillouin backscattering, Raman backscattering, and Rayleigh backscattering, which have been utilized in a multitude of studies measuring structural performance through reinforcement strains.

2.8.1.1 Rayleigh Backscattering

Strain sensing through DFOS relies on the return loss of light which occurs through scattering along the length of the cable, with three forms of backscattering occurring concurrently:

1. Raman scattering, which results from the thermal response of the glass molecules in the glass core of the fibre-optic cable as light travels through it, causing it to be extremely sensitive to changes in temperature.
2. Brillouin scattering arises through the interaction between light and acoustic waves generated by changes in density resulting from thermal changes and backscattered light.
3. Rayleigh scattering results from the elastic distribution of light in multiple directions when light encounters imperfections in the core of the fibre-optic cable. These imperfections are a product of the change in density and composition of the fibre core, leading to Rayleigh scattering being sensitive to mechanical strain and changes in temperature. Rayleigh scattering is based on Optical Frequency Domain Reflectometry (OFDR). OFDR uses Rayleigh scattering which takes place along the length of the fibre-optic cable and stores it as a signature of the fibre in an initial or reference condition. When the fibre is exposed to mechanical strain or temperature-based strain, the resulting Rayleigh scattering profile (time vs. position along fibre) is divided into discrete segments and then converted into the frequency domain using the Fourier transformation. The spectral shift of peak frequency is then calibrated to the mechanical or temperature-based strain subjected to the sensor. Figure 2-33 illustrates the principle of OFDR of Rayleigh backscattering.

Unlike other backscattering techniques, OFDR based strain sensing has the unique ability to capture dynamic measurements of distributed strains (i.e., up to 100 Hz depending on the overall sensing length and gauge distance between measurement points).

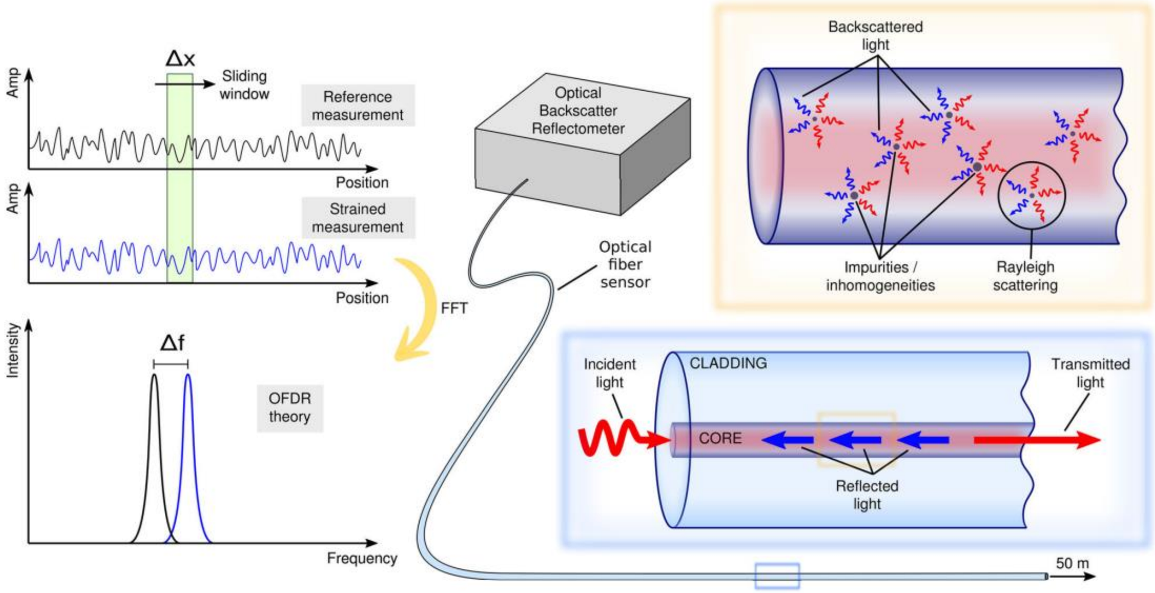

Figure 2-33. Rayleigh Backscattering Based on OFDR (Berrocal et al., 2021)

2.8.1.2 Applications of Distributed Fibre-Optic Sensing

DFOS has been implemented in reinforced concrete (RC) structural elements to measure mechanical strain along reinforcement lengths. Doing so can provide data regarding the status of the steel reinforcement, for instance, it can be monitored if a bar is near yielding at points along its length using DFOS. The capabilities of DFOS to provide strain data in structural applications has been explored in multiple studies. Pelecanos et al. (2018) conducted a set of pile tests with the use of fibre-optic sensors utilizing Brillouin Optical Time Domain Reflectometry (BOTDR) (Figure 2-34) to obtain the strain profile along a pile while it is loaded in order to understand pile performance, test design assumptions, and monitor any abnormalities in pile behaviour.

Figure 2-34. Reinforcement Cage Instrumented with Sensors (Pelecanos et al., 2018)

The study demonstrated the capabilities of fibre-optic sensors to provide in-situ performance data for piles. For instance, distributed strain data was obtained along the length of the piles (Figure 2-35 a)) which was used to calculate the corresponding displacement profile (Figure 2-35 b)). This data was in fair agreeance with the performance of the pile in the finite element model which was developed in parallel with the pile tests. Such findings provided insights which were not necessarily available without the use of fibre-optic technology. The displacement data obtained from the tests was utilized to calibrate key parameters used in finite element modelling of the piles.

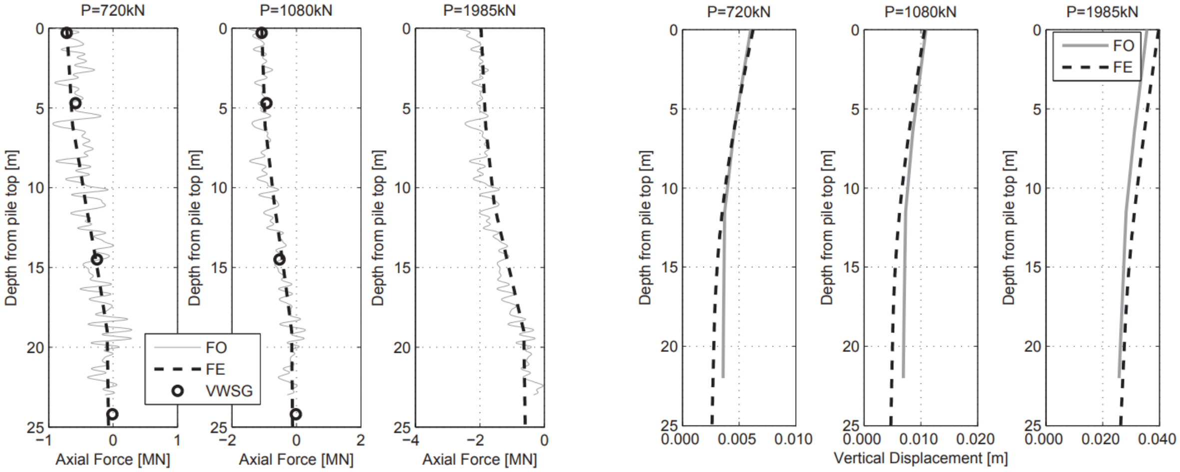

Figure 2-35. a) Strain Profile along Depth of Pile and b) Displacement Profile along Depth of Pile (Pelecanos et al., 2018)

Poldon et al. (2021) studied various behavioural mechanisms in large reinforced concrete beams with different shear reinforcement ratios, such as the stirrup strain profile along the depth of a beam and the development and growth of plastic hinges in the longitudinal reinforcement along the length of a beam. Reinforcement cages were instrumented with DFOS using Rayleigh backscattering along the stirrups and the longitudinal reinforcement as seen in Figure 2-36. The shear reinforcement ratios for specimens JP-1, JP-2, and JP-3 were 0.11%, 0.22%, and 0.33%. The longitudinal reinforcement ratio was kept constant at 1.47% for all beams.

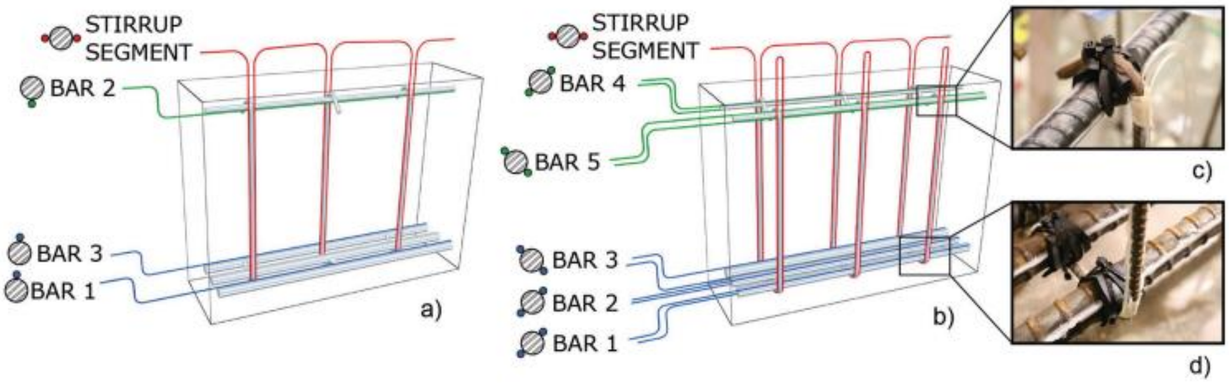

Figure 2-36. DFOS Layout on Reinforcement Cages (Poldon et al., 2021)

The DFOS installed along the longitudinal reinforcement provided insights regarding the structural performance of the RC beams. This included the identification of cracks, the formation of plastic hinges, as well as induced bending in compression reinforcement from stirrups. Figure 2-37 illustrates how cracking is exhibited in longitudinal reinforcement, where jumps in the strain gradient signify the occurrence of a crack. It was also evident that longitudinal reinforcement strains were similar (within ±100με) for a given load stage. Furthermore, when assessing the behaviour of the compression reinforcement, the compressive stresses decreased in locations corresponding to stirrups. This is because of the significant force transfer from the bar to concrete at points of intersection with the stirrups owing to the clamping action they exert on the bars.

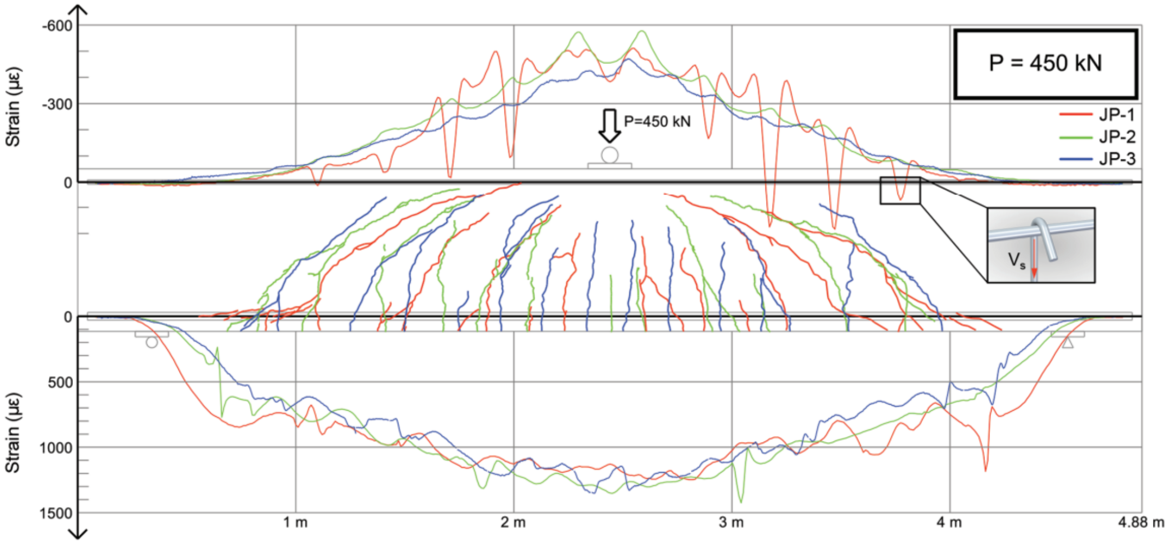

Figure 2-37. Plot of Longitudinal Reinforcement Strain (Poldon et al., 2021)

Strains along the shear reinforcement were measured, which revealed the non-uniform strain distribution along stirrup depths and across adjacent stirrups under a given shear force. Similar to the longitudinal reinforcement, increases in the strain gradient along the depth of the transverse reinforcement signified the occurrence of shear cracks (Figure 2-38).

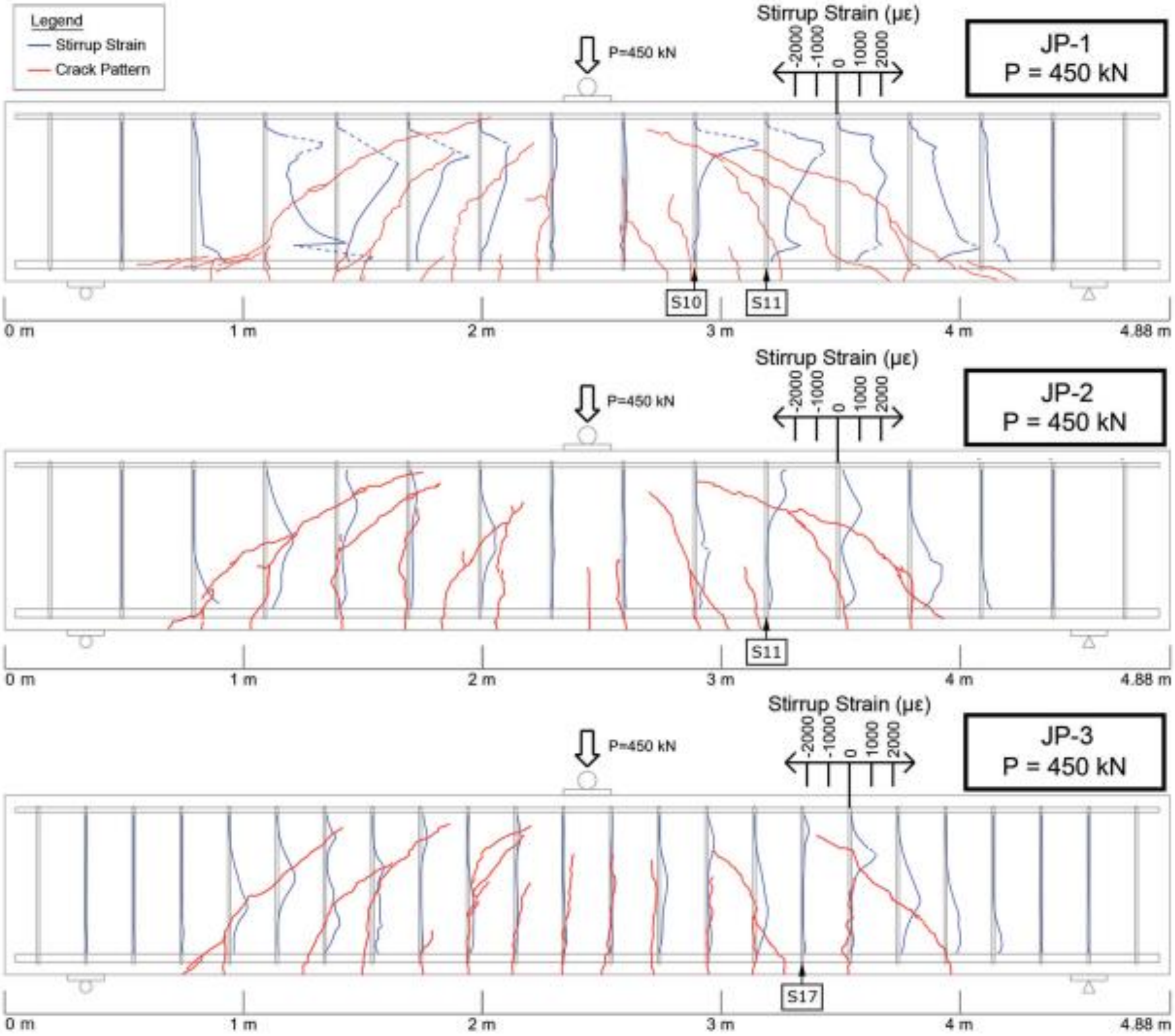

Figure 2-38. Plot of Transverse Reinforcement Strain (Poldon et al., 2021)

2.9 Research Gaps

The effect of varying fibre content and reinforcement ratio on the displacement ductility of UHP-FRC has been extensively studied using tradition point sensors such as strain gauges and external surface sensors such as DIC, not fully capturing the spatial nature of the interaction between UHP-FRC matrix and steel reinforcement. Studies have shown the capabilities of DFOS to provide distributed strain data along the steel reinforcement encased in conventional concrete. DFOS have not been extensively utilized to study the effects of varying fibre content and reinforcement ratio on the spread of elasticity, strain penetration, and displacement ductility of UHP-FRC beams in flexure. This could fill the gaps in data obtained by using multiple strain gauges along the length of the steel reinforcement by taking advantage of the 2.6mm gauge length of the DFOS, which is essentially similar to having a strain gauge installed at every 2.6mm.

Chapter 3: Experimental Methodology and Testing for Material Properties

An experimental program was designed to test the effects of reinforcement ratio and volumetric fibre content on the flexural behaviour of UHP-FRC beams. A total of four beam specimens were fabricated and tested under symmetric four-point loading to provide data for the investigation. Two different fibre contents and two longitudinal reinforcement ratios (Figure 3-1 a) and b)) were considered for the experimental program as seen in Table 3-1. A parallel test program was conducted to carry out material characterization of the two different UHP-FRC concretes used in the study. Figure 3-2 shows the specimen identification (ID code) used for the beam specimens; the numeral after the initial B corresponds to the sample number; R (for Longitudinal Reinforcement ratio) is followed by the percentage, and after the dash (-) is the volumetric fiber content.

Table 3-1. Beam Specimen Variables

Variable	**B1R2.3-1**	**B2R2.3-3**	**B3R1.5-3**	**B4R1.5-1**
ρ (%)	2.3 (20M bars)	2.3 (20M bars)	1.5 (15M bars)	1.5 (15M bars)
Fibre content (%)	1	3	3	1

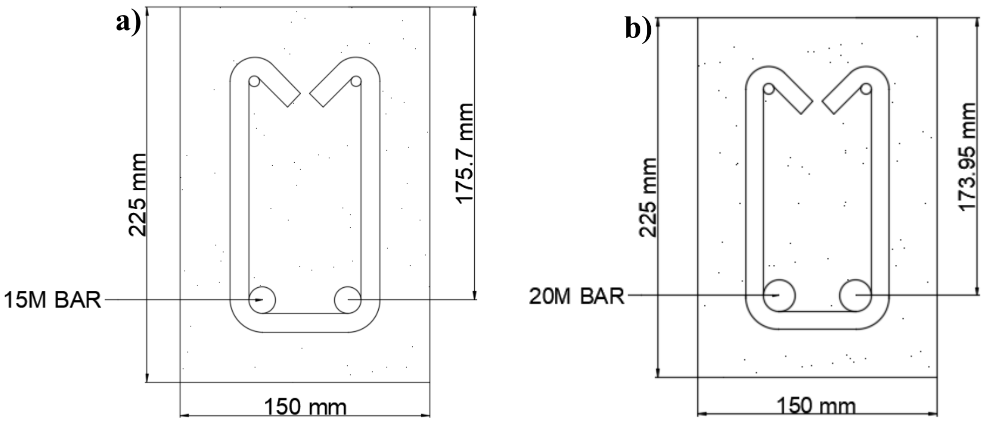

Figure 3-1. a) 1.5% Reinforcement Ratio Specimen and b) 2.3% Reinforcement Ratio Specimen

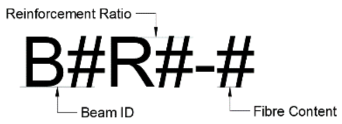

Figure 3-2. Specimen Identification Scheme

The experimental program consisted of four phases, as seen in Table 3-2Phase 1 consisted of fabricating the cages and instrumenting them with strain gauges and DFOS to then be implemented in Phase 2, which was the casting of the beam specimens. Phase 3 was then able to be implemented once the appropriate curing period was achieved to conduct material characterization tests in compression at 28-days and compression tests on the day of testing of the beam specimens. It should be noted that direct tension tests of UHP-FRC prisms were attempted but were unsuccessful due to issues with the testing fixture. Uniaxial tension tests were conducted on coupons of the longitudinal reinforcement used in the beam specimens, to characterize the stress-strain response of the bars. Phase 4 refers to final testing of the beam specimens. This required the modification of the prism testing assembly which was intended to be used to conduct the four-point loading beam test. Phase 4 is discussed in detail in 4.1.

Table 3-2. Experimental Phases

Phase 1: Specimen Preparation	**Phase 2: Casting of Specimens**	**Phase 3: Material Characterization Tests**	**Phase 4: Four-Point Loading Beam tests**
• Cage Fabrication • Sensor Installation	• Casting of beams and characterization specimens • Flowability tests	• 28-day and beam test day compression tests for elastic modulus, Poisson's ratio, and compressive Strength • Uniaxial tension tests of rebar	• Modification of prism testing assembly • Specimen Preparation for tests • Four-point loading beam tests

3.1 Fabrication of Cages

Reinforcing bars used for fabrication of the reinforcement cages were bent using a rotary rebar bender (Figure 3-3). Reinforcement cages consisted of longitudinal steel (15M and 20M) (see Table 3-1), 6mm support wire, and 10M stirrups. The longitudinal reinforcement consisted of 180° bends at the ends and the stirrups consisted of three 90° bends and two 135° bends for sufficient anchorage. Reinforcement cages were assembled using zip ties as opposed to rebar tie wire due to their propensity to cut through the DFOS. A sample rebar cage is present in Figure 3-4.

Figure 3-3. Rotary Rebar Bender

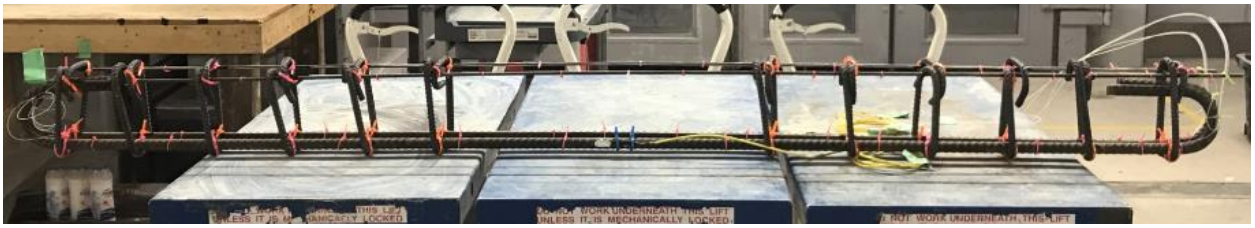

Figure 3-4. Rebar Cage

3.2 Installation of Sensors

Steel reinforcement cages were instrumented with both strain gauges and DFOS to measure reinforcement strain during the experimental campaign for the beam specimens. Strain gauges were used to provide discrete strain readings at midspan on a single bar, and DFOS were used to provide distributed strain readings along the steel reinforcement and top support wire.

3.2.1 Installation of Strain Gauges

Strain Gauges were installed at midspan for each of the four reinforcement cages to measure the tensile strain of steel at a localized point. This was to validate and verify the data obtained from the DFOS.

A belt sander was used to sand a small portion of the longitudinal reinforcement surface to provide a smooth, flat surface for the strain gauge. This required the complete removal of the reinforcement ribs. The smoothened reinforcement surface was wiped with isopropyl alcohol to cleanse it of any debris from sanding the reinforcement. The gauge length was 10mm (SHOWA strain gauges). A strain gauge was applied to the sanded surface using Kapton tape and cyanoacrylate adhesive. Afterwards, a Teflon tape and liquid rubber compound were applied onto the strain gauge to provide a waterproof barrier and protect the strain gauge from damage that could occur during the casting process (Figure 3-5). The strain gauge was then soldered to instrumentation wire which would be used to connect to the DAQ during tests. Additionally, heat shrink tubing was placed around the connected portion of the instrumentation wire to the strain gauge to prevent from the formation of short circuits due to contact with the rebar. The electrical resistance of the strain gauge was measured using a multimeter before and after casting. For the given model of strain gauge, an electrical resistance of 120Ω ± 0.3% was required to deem the strain gauge as being capable of providing acceptable readings.

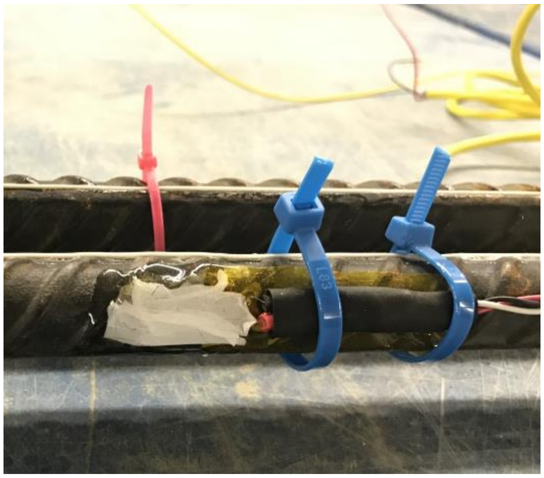

Figure 3-5. Installed Strain Gauge on Rebar

3.2.2 Instrumentation of Distributed Fibre-Optic Sensors

DFOS were installed along the length of the top support wire and along both longitudinal reinforcements to provide continuous strain readings across the entire length of the reinforcement cage in both compression and tension. Both longitudinal reinforcements were instrumented with DFOS due to the possibility of the sensor providing unreliable data due to damage.

Approximately 8 to 12m of fibre-optic cable was used to instrument each of the reinforcement cages. This was to ensure sufficient length accounting for coiling of sensors within beams, measurement length, and external length to be connected to the patch chord. A fibre-optic cable was connected to the longitudinal reinforcement along the longitudinal rib because it provided a smooth, straight surface to which the sensor could be attached (Figure 3-6). First, zip ties were used to connect the fibre-optic cable to the longitudinal reinforcement, ensuring the sensor cable was straight and not shifting. Afterwards, cyanoacrylate adhesive was used to bond the fibre-optic cable to the surface of the longitudinal rib. A similar process was used to instrument the top support wire, apart from using the longitudinal rib for sensor attachment due to the support wire being smooth. “Dead loops”, which is coiling of the fibre-optic sensor in the zone where the sensor transitions between the reinforcement elements, were used to prevent strain transfer between the longitudinal reinforcement and the top support wire (Figure 3-7).

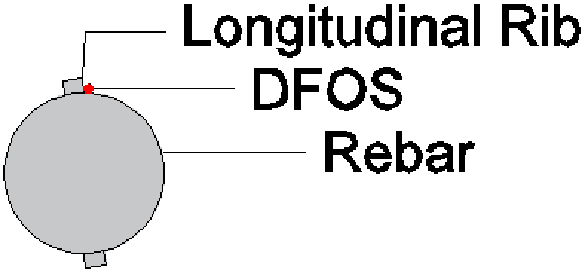

Figure 3-6. DFOS Placement

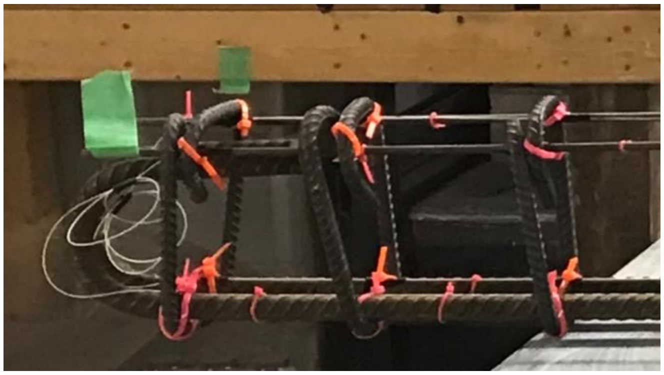

Figure 3-7. Dead Loop

As previously mentioned, sensors were installed on both longitudinal reinforcement and top support wire. On one side, electrical tape was placed on top of the DFOS where the stirrups would be anchored to the longitudinal reinforcement and the support wire, to prevent damage of the sensors. On the other side, consumer-grade silicone was used as a protective layer along the entire length of the fibre-optic sensor as a back-up measure to ensure no damage from concrete pouring and anchoring of stirrups on cages (Figure 3-8 a)). It should be noted that the rebar instrumented with DFOS and a layer of silicone was used during the four-point loading tests of the beams. At the exit locations, sensors passed through rubber tubing to prevent tearing due to the surrounding concrete (Figure 3-8 b)).

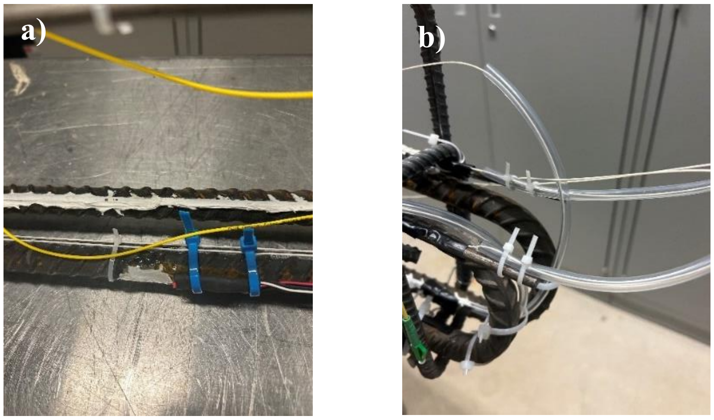

Figure 3-8. a) DFOS on Rebar and b) Protection of DFOS at Exit Point

The fibre-optic cable was spliced and connected to the patch chord which enables the interaction between the fibre-optic sensor and interrogator. With the completion of the splicing process, the sensor was configured to define its measurement length. Key points on the sensor were defined to trace the milestone points for strain measurements. These included top-middle and bottom-middle (points for highest-strain in compression and tension); top-left and top-right defining the sensor length in compression; bottom-left and bottom-right to define the measurement length in tension (Figure 3-9). Table 3-3 shows the distances relative to the connection point of the DFOS cable. It should be noted that the key point locations along specimen B3R1.5-3 were not obtained due to use of the backup sensor which was not keyed in.

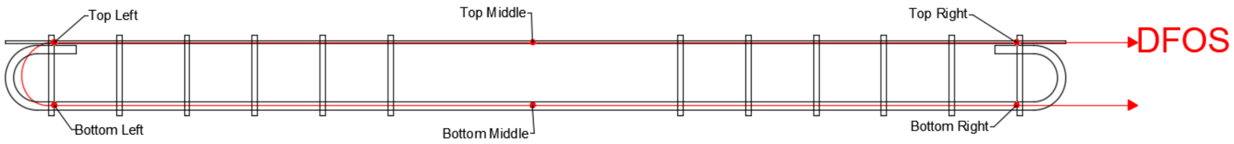

Figure 3-9. Key Points on DFOS along Beam Length

Table 3-3. Key Point Distances along Sensor Length

Location	**Distance (mm)**			
	B1R2.3-1	**B2R2.3-3**	**B3R1.5-3**	**B4R1.5-1**
Top Right	2638.4	5594.6	NA	2225
Top Middle	6418.8	6593	NA	3226
Top Left	4637.8	7594	NA	4227
Bottom Right	7419.8	10511.2	NA	7167.6
Bottom Middle	6418.8	9150.2	NA	6169.2
Bottom Left	5417.8	8511.8	NA	5168.2

3.3 Casting of the Specimens

The mixture proportions and mixing methodology were provided by Sika Canada Inc and strictly followed with the exception of using fibres at two different volumetric ratios. The UP-F3 Poly Premix provided by Sika Canada Inc (Figure 3-10) consisted of a 3% volumetric fibre content, with straight steel fibres with a length of 13mm and a diameter of 0.2mm.

Figure 3-10. Sika Premixture

3.3.1 UHP-FRC Mixture Proportions

Table 3-4 refers to the UHP-FRC mixture consisting of 3% volumetric fibre content and Table 3-5 refers to the UHP-FRC mixture consisting of 1% volumetric fibre content.

Table 3-4. Mix Design for 3% Fibre Content Mix

Constituents	**Weight (kg)**
UP-F3 POLY Premix	200
Fresh Potable Water	16.2
Ice	5.4
Admixture “A”	1.8
Admixture “B”	1.3
Admixture “C”	1.87
Steel Fibres	20.3

Table 3-5. Mix Design for 1% Fibre Content Mix

Constituents	**Weight (kg)**
UP-F3 POLY Premix	200
Fresh Potable Water	16.2
Ice	5.4
Admixture “A”	1.8
Admixture “B”	1.3
Admixture “C”	1.87
Steel Fibres	6.77

3.3.2 Mixing Methodology

All mixtures for the beam and companion characterization specimens were conducted in the mixing room of the High-Bay laboratory at Bergeron Center, York University. Four batches were mixed as the volume was limited by the capacity of the mixer. Each batch was 0.102m^3 and accounted for the volume of one beam, cylinder samples, direct tension prisms, and a possible 10% waste of material. A Creteangle Mixer was used to mix each of the four batches. The mixing methodology in Table 3-6 was followed.

Table 3-6. Mixing Methodology

Steps	**Constituent to Introduce**	**Action**	**Time (Minutes)**
1	1/2 of required bags of UP-F3 Poly Premix	Add 1/2 of required bags of UP-F3 Poly Premix	-
2	N/A	Mix	2.00
3	a) 50% of water + 100% of Admixture "A" & b) 50% of water + 100% of ice	Gradually introduce water, ice, and Admixture "A"	0.50
4	N/A	Mix	2.00
5	a) 1/2 of required bags of UP=F3 Poly Premix & b) 100% of Admixture "B"	Add remaining bags of UP-F3 Poly Premix and gradually introduce Admixture "B"	1.50
6	N/A	Mix	2.00
7	Steel Fibres	Gradually introduce steel fibres	3.00
8	N/A	Mix	3.00
9	N/A	Scrape unmixed constituents	1.00
10	100% of Admixture "C"	Gradually introduce Admixture "C"	1.00
11	N/A	Mix	2.00

12	N/A	Batch completed	-

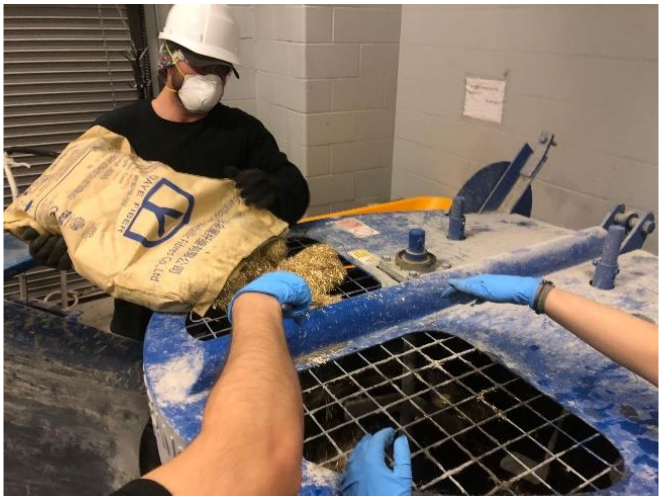

Figure 3-11. Mixing of Steel Fibres

At the end of the mix, the flowability test was conducted to measure the fresh properties of the mixture (Figure 3-12). Four measurements of the diameter were used for the flowability test which was conducted for each batch (Table 3-7).

Figure 3-12. Flowability Test

Table 3-7. Flowability Test Results

Diameter Measurement	Diameter (mm)			
	Batch 1 (3%)	**Batch 2 (3%)**	**Batch 3 (1%)**	**Batch 4 (1%)**
D1	225	238	220	230
D2	235	231	203	223
D3	230	222	239	220
D4	224	230	218	220
Average	228.5	230.25	220	223.5

After the completion of the flowability test, concrete was then transferred from the mixer to plastic buckets to commence the casting of the specimens (Figure 3-13).

Figure 3-13. Removal of UHP-FRC from Mixer

3.3.3 Casting of Specimens

Prior to casting, the forms and cylinder molds were oiled to allow for ease of demolding of the specimens (Figure 3-14). Custom-made 3-D printed chairs were made to secure the required 30mm clear cover (relative to stirrup). The strain gauge instrumentation wire and external portion of the DFOS were placed in plastic bags to prevent any damage during the cage placement and concrete pouring. The plastic bag containing the DFOS was placed within a plastic bucket to provide further protection from movement/commotion during casting.

Figure 3-14. Oiled Formwork

Figure 3-15. Placement of Cage in Formwork

Figure 3-16. Finished Pour of UHP-FRC in Formwork

The casting procedure utilized was consistent with that of ASTM 1856/1856M-17 (2017). Cylinders and direct tension prisms were filled in one layer. Direct tension prisms had concrete poured from one end (Figure 3-17). A similar casting process conducted for the direct tension specimens was applied to casting the reinforced UHP-FRC beam specimens (Figure 3-18) as an attempt to obtain similar fibre alignment in the beam which would reflect that of the prisms, thus maintaining the tensile strength of the material, although the presence of stirrups would most likely affect the fiber flow to a significant extent. It should be noted that concrete was poured from the end of the “dead loop” to prevent any damage or movement of the fibre-optic sensors near their exit point. Concrete was poured into cylinders and prisms using scoops, whereas concrete was poured from buckets into the formwork for the beams. To allow for flow of the UHP-FRC material from one end of the beam to the other, a mallet was used to apply external vibration.

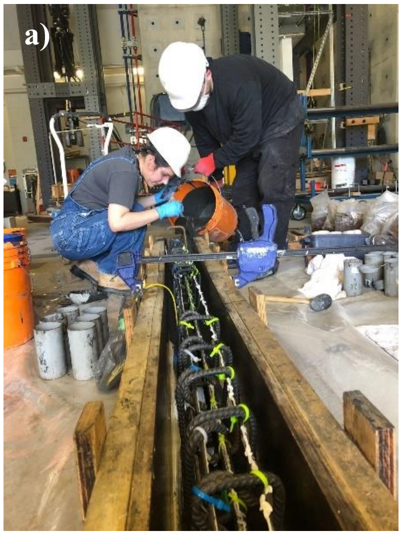

Figure 3-17. Pouring of UHP-FRC into Beam Specimen Formwork

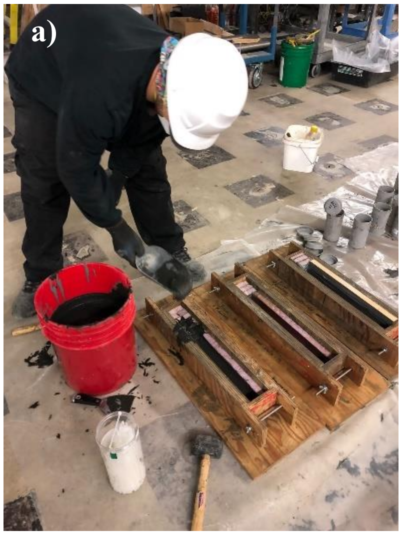

Figure 3-18. Pouring of UHP-FRC into Direct Tension Specimen Formwork

Once the cast was complete, beam specimens had a layer of vapour barrier placed on top to prevent moisture from escaping, along with a plank of form ply over the length of the constant moment region to improve the smoothness of the top surface (Figure 3-19). A vapour barrier was also placed on the direct tension prisms with plexiglass on top to ensure all specimens had a flat surface, maintaining the 50mm x 50mm cross-sectional dimensions.

Figure 3-19. Finished Casting of a beam specimen and accompanying material characterization samples

3.3.4 Curing

Specimens were cured in their forms for 48 hours. Afterwards, they were demolded and prepared for continued curing. Beams were wrapped in wet burlap and covered in vapour barrier to prevent any escape of moisture (Figure 3-20 a)). Direct tension specimens and six cylinders for material characterization were placed in a water tub for the remainder of the 28-day curing period at ambient conditions (Figure 3-20 b)). Three cylinders for each fibre content were placed in wet burlap and wrapped in vapour barrier to mimic the curing conditions of the beams in order to measure the compressive strength which appropriately represents that of the beams, on the test day. This process excluded curing the direct tension prism in wet burlap and vapour barrier due to the ultimate tensile strength occurring after cracking, with its tensile behaviour being primarily controlled by the fibre contribution as opposed to the cementitious matrix. Beams and cylinder specimens wrapped in burlap and vapour barrier were moist cured and were watered weekly until the day of testing.

Figure 3-20. a) Curing of Beam and Companion Specimens and b) Curing of 28-Day Test Material Characterization Specimens

3.4 Compression Tests

Compression tests of UHP-FRC cylinders were conducted to obtain elastic modulus, Poisson's ratio, and compressive strength of the material. Cylinder tests followed the requirements of ASTM C469/C469M-10 (2010) for testing for elastic modulus and Poisson's ratio, and ASTM 1856/1856M-17 (2017) for compressive strength. It should be noted that compression tests were displacement-controlled in order to obtain post-peak behaviour of UHP-FRC in compression. Additionally, cylinder grinding took place prior to compressive tests to ensure smooth/flat end surfaces of the cylinders.

3.4.1 Installation of Strain Gauges on Cylinders

In the absence of a compressometer appropriate for the standard size of UHP-FRC cylinder samples, strain gauges were used to instrument the cylinders. Two Pairs of strain gauges were installed on the lateral surface of the specimens to measure both lateral and axial strain on opposite sides of the cylinders (one vertical and one horizontal strain gauge on each side). Strain gauges were placed at mid-height of the cylinders using cyanoacrylate adhesive on a smooth patch of the lateral surface, avoiding any voids (Figure 3-21). Terminals were used for the strain gauge wires to prevent any movement which would cause damage to the sensors. The strain gauges were the soldered to instrumentation wire which would be connected to the data acquisition system (DAQ).

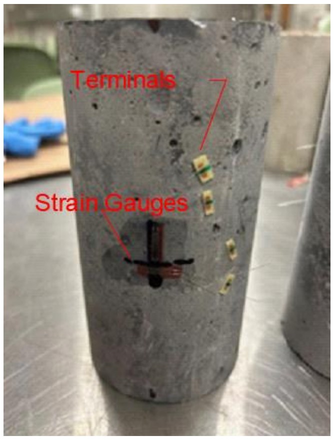

Figure 3-21. Strain Rosette on Cylinder

3.4.2 Compression Test Setup

Compression tests were conducted using the CONTROLS Automax compression device which allowed for both displacement-controlled and load-controlled tests. Cylinders instrumented with strain gauges were placed centrally within the compression tester (Figure 3-22). Strain gauges exited the back of the tester to the DAQ, ensuring that no exposed wires connected to the strain gauges were touching to prevent the formation of short circuits of the strain gauges.

Figure 3-22. Cylinder Instrumented with Strain Gauges in Compression Tester

3.4.3 Elastic Modulus and Poisson's Ratio

Testing for static elastic modulus and Poisson's ratio was done according with ASTM C469/C469M-10 (2010). It is noted that according to this standard, the elastic modulus of concrete is set equal to the slope of the chord to 40% of peak load in the axial stress – axial strain diagram which is obtained from compression testing of standard cylinder samples. Three companion cylinders were first used to measure the reference compressive strength of the material. The cylinders were loaded up to 40% of the reference compressive strength. A displacement rate of 0.1mm/min was used during tests. Once the specimens reached 40% of *f'c* the test was stopped, and the specimens were unloaded. The strain gauges were zeroed upon full removal of the load, and the test would then recommence. During each of the cycles/tests, a preload of approximately 5kN was applied to the specimens, which would then be zeroed, allowing the test to begin. Three loading cycles took place, with the first cycle being used for seating of the specimen, and cycles 2 and 3 being averaged and used to determine static modulus of elasticity and Poisson's ratio. Three successful tests of cylinders were used to determine elastic modulus and Poisson's ratio.

3.4.4 Compressive Strength

Tests to obtain the complete stress-strain of concrete were done at a displacement-controlled loading rate of 0.1mm/min. Longitudinal strain data was obtained through the use of two strain gauges on opposite sides, which were then averaged. Three successful tests of the cylinders were required to characterize the material in compression; a minimum compressive strength of 120MPa is required for the material to be classified as UHP-FRC according with CSA S6:19 Annex A8.1 (2019)and CSA A23.1:19 Annex U (2019).

3.4.5 Results of Compression Tests

Table 2-1 summarizes the results of the 28-day compression tests. Overall, there was a slight increase in compressive strength, elastic modulus, and crushing strain; but a decrease in Poisson's ratio when increasing the fibre content from 1% to 3%. This was due to post-cracking stiffness induced by the crack bridging capacity of the fibres and added confinement effects at higher fibre contents which delay the onset of failure due to excessive lateral dilation. Regarding the stress-strain response, all specimens demonstrated a near linear response up to peak load where a brittle failure was encountered as seen in Figure 3-23 and Figure 3-24. Furthermore, delamination of the cylinder was demonstrated for all cylinders, regardless of fibre content as seen in Figure 3-26.

Table 3-8. Summary of Material Characterization Tests in Compression

Fibre Content	**Cylinder**	**Diameter (mm)**	**Area (mm^2)**	**Height (mm)**	**E_c (MPa)**	**Poisson's Ratio**	**ε_{co}**	**f'c (MPa)**
1%	**C1-1**	76.0	4536.5	147	41061	0.23	0.0044	153.1
	C2-1	77.5	4714.9	147	40572	0.25	0.0041	146.8
	C3-1	77.2	4683.6	148.13	40476	0.24	0.0039	143.4
	Mean	**-**	**-**	**-**	**40703**	**0.24**	**0.0041**	**148**
	Standard Deviation	**-**	**-**	**-**	**313.9**	**0.011**	**0.00029**	**4.9**
	Characteristic Value	**-**	**-**	**-**	**-**	**-**	**-**	**140.9**
3%	**C1-3**	77.1	4668.7	149.0	43756	0.23	0.0039	148.99
	C2-3	77.6	4734.4	148.9	37586	0.19	0.0052	145.15
	C3-3	76.2	4559.2	149.4	41958	0.22	0.0041	153.06
	Mean	**-**	**-**	**-**	**41100**	**0.22**	**0.0044**	**149.06**
	Standard Deviation	**-**	**-**	**-**	**3173**	**0.02**	**0.0007**	**3.96**
	Characteristic Value	**-**	**-**	**-**	**-**	**-**	**-**	**143.5**

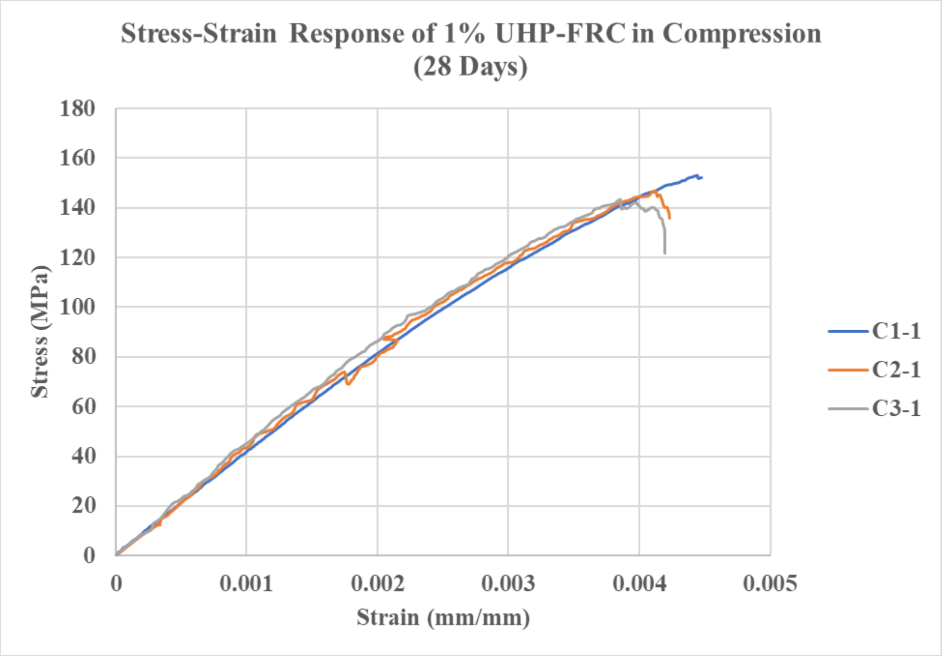

Figure 3-23. Stress-Strain Response of 1% UHP-FRC in Compression at 28 Days

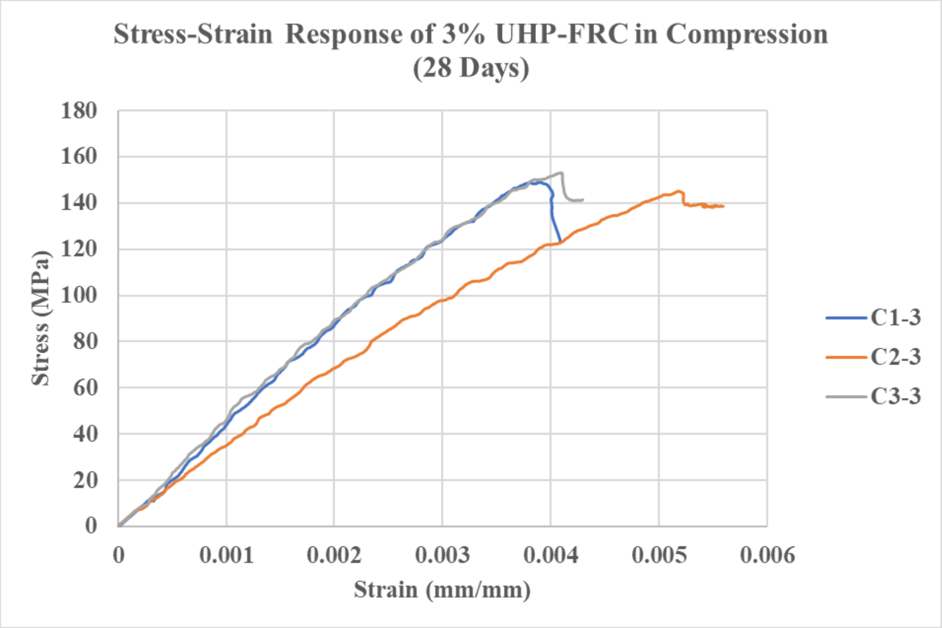

Figure 3-24. Stress-Strain Response of 3% UHP-FRC in Compression at 28 Days

The full compressive response of a 3% fibre content specimen (C2-3) is displayed in Figure 3-25, which was the only successful cylindrical specimen of the 3% fibre content batch to exhibit post-peak behaviour. The post-peak behaviour of C2-3 was captured using the strain due to the movement of the actuator head, which was then combined with the strain captured by the strain gauge in the ascending branch of the response in compression. This was due to failure of the strain gauge almost immediately after failure. The post-peak response was brittle, with a sharp decrease in the compressive stress to 51% of the peak stress. Afterwards, an almost linear decrease in stress is exhibited towards the end of the response.

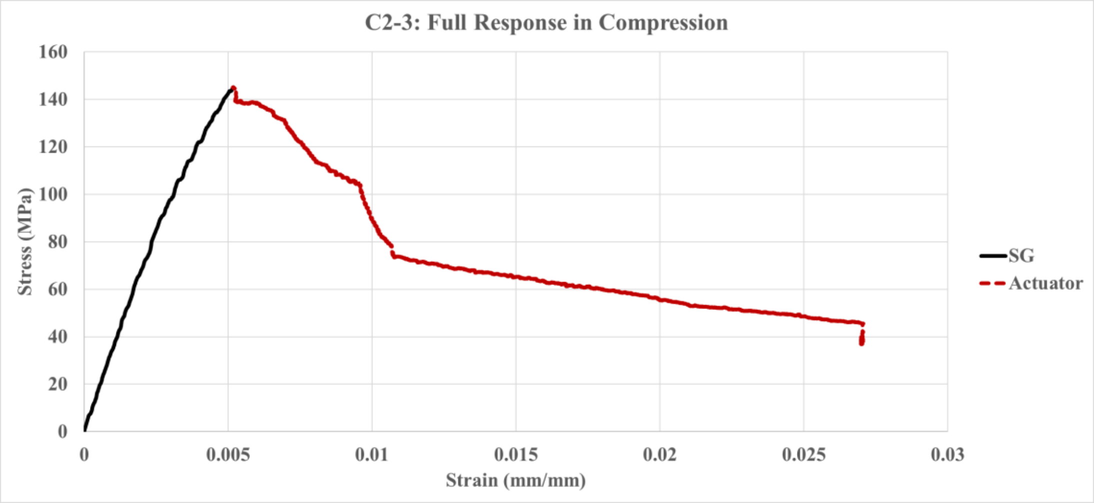

Figure 3-25. Full Compressive Response of 3% Fibre Content Specimen (C2-3)

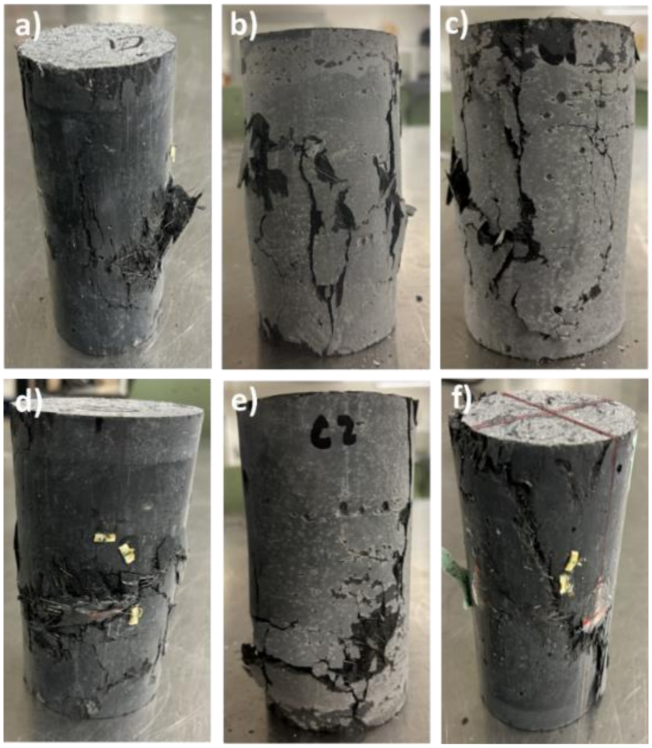

Figure 3-26. Cracking Patterns of UHP-FRC Cylinders a) C1-1, b) C2-1, c) C3-1, d) C1-3, e) C2-3, and f) C3-3

3.5 Uniaxial Tension Tests of Reinforcing Bars

Uniaxial tension tests were performed on each of the bar sizes (15M and 20M) used as longitudinal reinforcement in the beam specimens to determine the yield properties and ultimate tensile strength of the rebar used in fabricating the beams. The tests followed the provisions of ASTM E8/E8M-16; a minimum of three successful tests per bar size were required (Figure 3-27).

Figure 3-27. Reinforcement Specimens

3.5.1 Sizing of Reinforcing bar coupons

Sizing of the bar coupons was determined through the required gauge length and grip length. ASTM E8/E8M-16 (2016) suggests using a gauge length of five times the diameter of the bar being tested. This value was increased to 210mm to account for the size of the extensometer which was used to measure displacement with a total grip length of 90mm (Table 3-9).

Table 3-9. Measured Dimensions of Rebar Specimens

Specimen	**Size**	**D_b (mm)**	**Grip Length (mm)**	**Gauge Length (mm)**	**Total Length (mm)**
R1	15M	15.25	90	210	300
R2	15M	15.19	90	210	300
R3	15M	15.11	90	205	295
R4	20M	18.87	90	205	295
R5	20M	19.52	90	205	295
R6	20M	18.55	90	205	295

3.5.2 Test Setup and Execution

A servo-controlled, closed loop universal testing machine (UTM) by MTS was used to conduct the uniaxial tension tests of the rebar specimens (Figure 3-28 a)). Specimens were placed within the grips of the UTM, and a 50mm gauge length extensometer was placed at mid-height (Figure 3-28 b)).

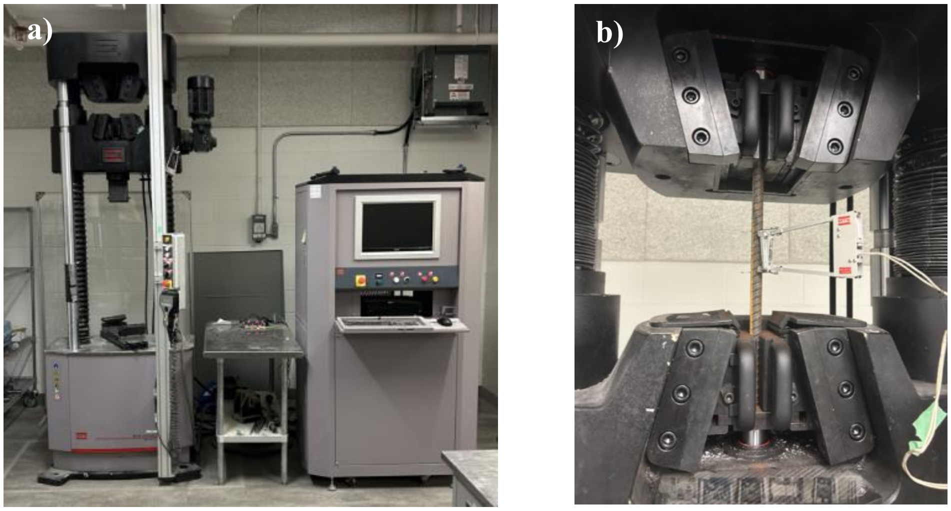

Figure 3-28. a) Universal Testing Machine by MTS and b) Uniaxial Tension Test Setup

The uniaxial tension tests were strain controlled, and were conducted using two loading rates as specified by ASTM E8/E8M-16 (2016)), i.e., a rate of 0.015mm/mm/min until yielding, was increased to 0.05mm/mm/min for the remainder of the test Three coupons were tested for each bar size; only those tests that resulted with bar rupture within the gauge length of the extensometer were considered successful.

3.5.3 Results of Uniaxial Tests on Reinforcing Bars

The material properties of the longitudinal reinforcement obtained through uniaxial tests of the reinforcement bars are summarize in Table 3-10 and Table 3-11. Furthermore, the stress-strain response for both bars sizes can be seen in Figure 3-29 and Figure 3-30. The 20M reinforcement demonstrated a larger ultimate strength but lower ultimate strain in comparison to the 15M reinforcement.

Table 3-10. 15M Reinforcement Properties

Reinforcement	**D_b (mm)**	**A (mm^2)**	**E_s (MPa)**	**F_y (MPa)**	**ε_y**	**ε_{sh}**	**F_u (MPa)**	**ε_u**
15M (Bar 1)	16	200	205143	458.51	0.0022	0.02	561.3	0.21
15M (Bar 2)	16	200	209305	430.53	0.0023	0.01	591.3	0.21
15M (Bar 3)	16	200	203344	392.65	0.00179	0.02	552.0	0.20
Mean			**205931**	**427.2**	**0.0021**	**0.018**	**568.18**	**0.20**

Table 3-11. 20M Reinforcement Properties

Reinforcement	**D_b (mm)**	**A (mm^2)**	**E_s (MPa)**	**F_y (MPa)**	**ε_y**	**ε_{sh}**	**F_u (MPa)**	**ε_u**
20M (Bar 1)	19.5	300	206080	462.6	0.0019	0.016	600.9	0.16
20M (Bar 2)	19.5	300	204801	413.6	0.0023	0.018	563.8	0.17
20M (Bar 3)	19.5	300	193071	428.0	0.0021	0.022	577.9	0.18
Mean			**201317**	**434.8**	**0.0021**	**0.019**	**580.9**	**0.17**

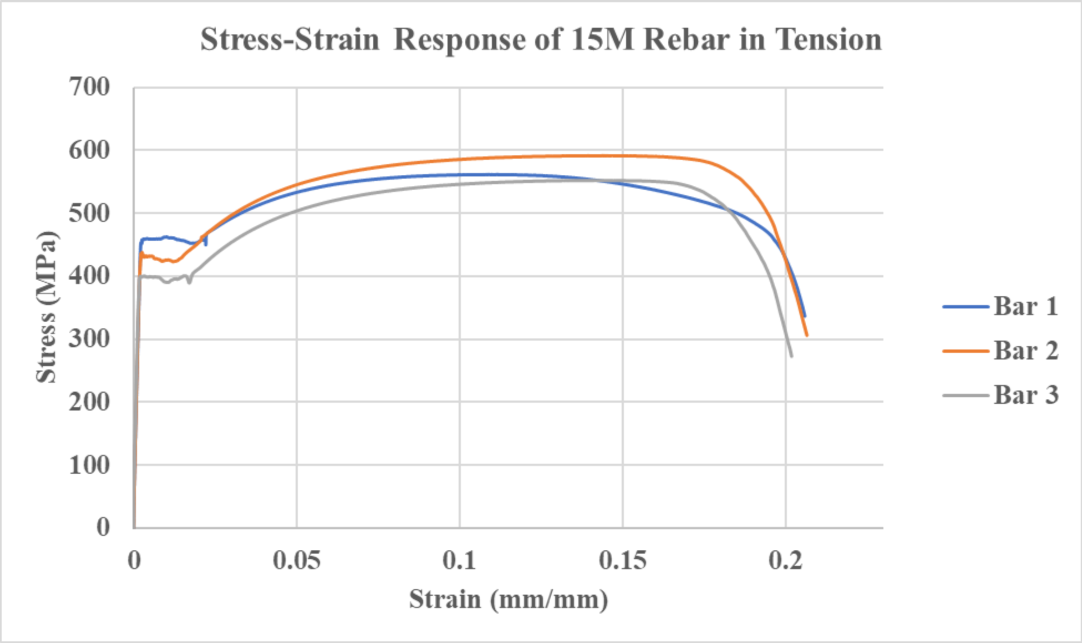

Figure 3-29. Stress-Strain Response of 15M Reinforcement Bar

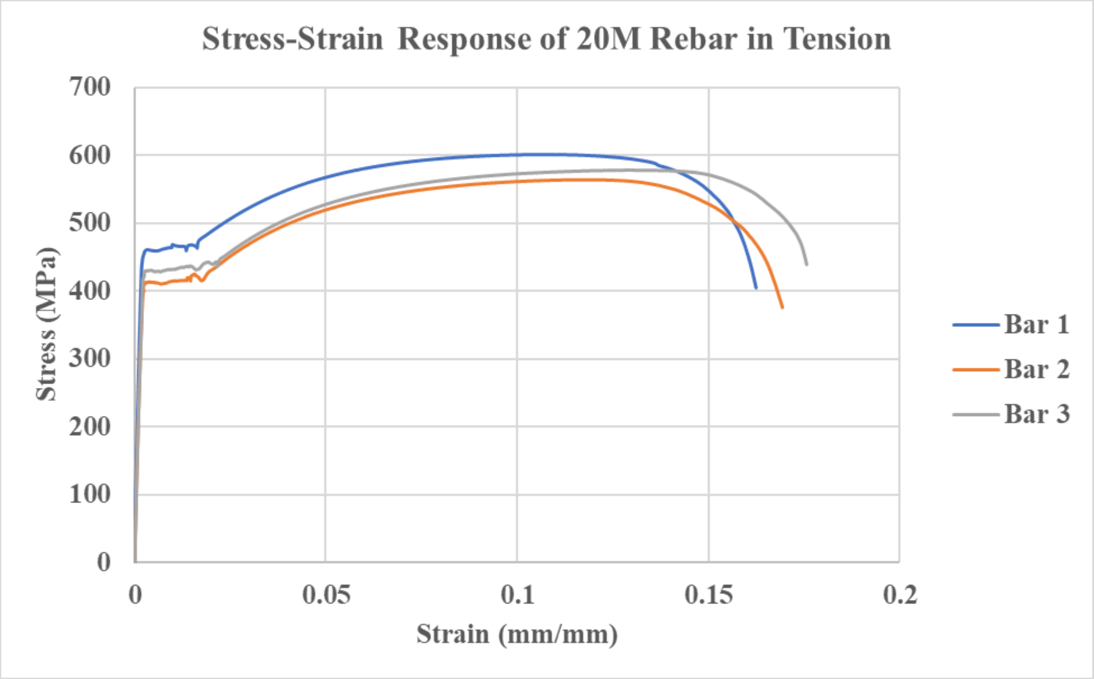

Figure 3-30. Stress-Strain Response of 20M Reinforcement Bar

Chapter 4: Experimental Campaign for UHP-FRC Beams in Flexure

This chapter presents the experimental campaign, results, discussion, and conclusions of the four-point loading beam tests of UHP-FRC beam specimens instrumented with DFOS. Four beams were tested, with two reinforcement ratios (ρ_s=2.3% and 1.5%), as seen in Figure 4-1, and two volumetric fibre contents (3% and 1%), to study the effects of varying fibre content and reinforcement ratio on the displacement ductility of UHP-FRC beams. DFOS were used to capture distributed strains along the longitudinal reinforcement and in the top support wire to provide insights pertaining to plastic hinge formation and strain penetration into the steel reinforcement away from the critical section of the beams. Furthermore, discrete reinforcement strain was measured using strain gauges at midspan to verify the reinforcement strain recorded by the DFOS.

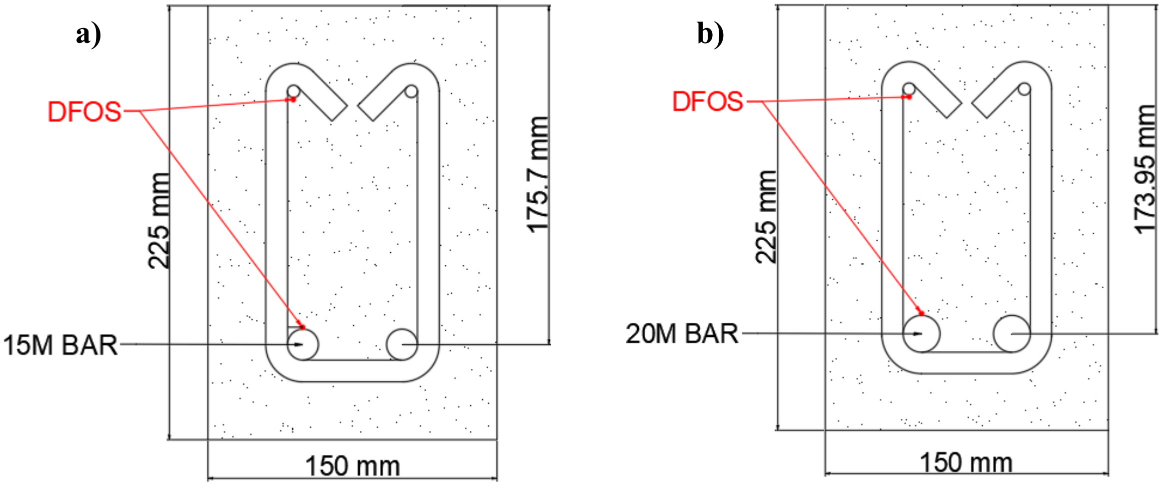

Figure 4-1. Beam Specimen Cross-Sections a) 1.5% Reinforcement Ratio and b) 2.3% Reinforcement Ratio

4.1 Beam Specimen Experimental Campaign

This section focusses on the preparation and execution of the experimental program concerning the testing of the beam specimens. It provides information regarding the prism testing assembly and data acquisition.

4.1.1 Test Frame Modification

The available prism testing assembly (Figure 4-3 a)) was modified to meet the experimental requirements. A W310x107 support beam was attached to the bottom cross beam of the prism testing assembly to support the 2m span of the test specimens during loading. A W360x216 spreader beam was designed to apply load with a minimal 500mm distance between loading points, at 50mm increments (Figure 4-2). To reduce the large unsupported length of the vertical pylons of the test frame intermediate bracing members were installed at mid-height; these were W310x107 steel sections placed on the opposite spans, parallel to the specimen orientation. The final result of the prism testing assembly can be seen in Figure 4-3 b).

Figure 4-2. Spreader Beam

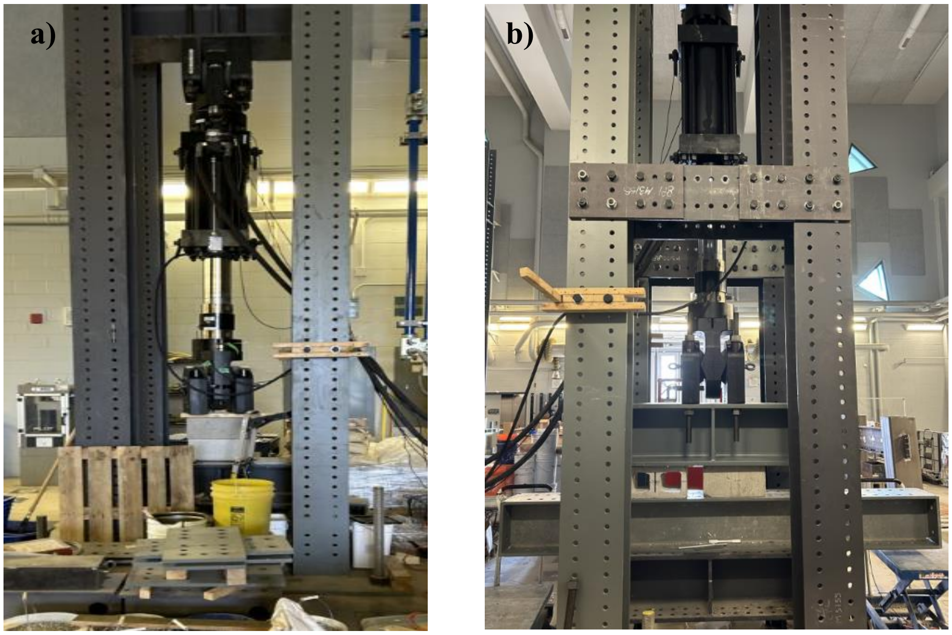

Figure 4-3. a) Prism Testing Assembly and b) Modified Prism Testing Assembly

Since the supports of the beam specimens were located in the cantilevering segments of the support beam, deflections of the supports during the tests were a concern. Deflections were calculated using elastic analysis. Equations 4.1 and 4.2, which refer to Figure 4-4, were used to calculate the deflection beneath the support and at the free end of the support beam. A deflection of 0.01mm was determined to occur beneath the support with a 0.032mm maximum deflection occuring at the free end (Figure 4-5). Due to the small magnitude of the calculated deflections, it was determined that they would not pose a concern during the four-point loading beam tests.

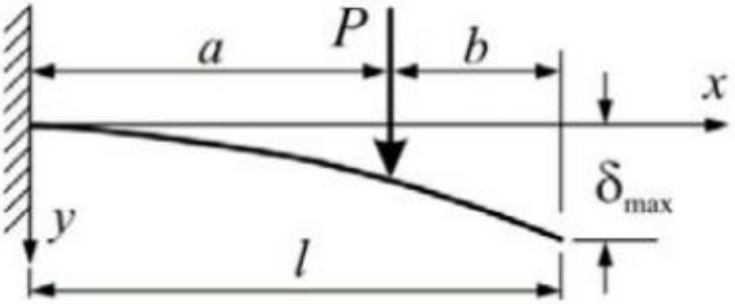

Figure 4-4. Deflection of Cantilever Beam with Point Load along its Length

$$y = \frac{Px^2}{6EI}(3a - x)\ for\ 0 < x < a \tag{4.1}$$

$$y = \frac{Px^2}{6EI}(3x - a)\ for\ a < x < l \tag{4.2}$$

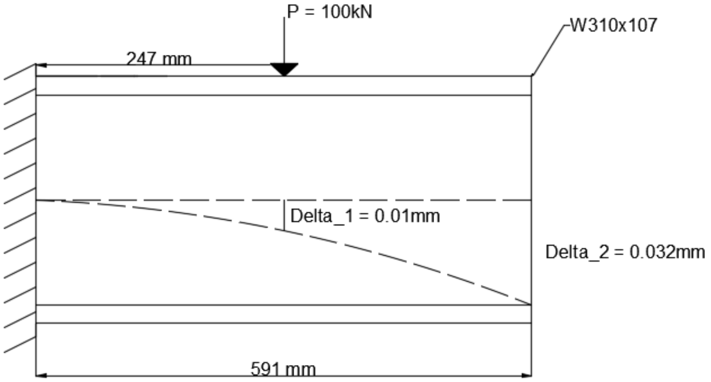

Figure 4-5. Deflection of Support Beam

4.1.2 Beam Specimen Preparation

4.1.2.1 Loading Surface Preparation

Hydrostone gypsum cement was used to smoothen the beam surface under the loading points. The mixture used consisted of 32 parts water to 100 parts plaster. Once the plaster was placed on the top surface of the beam specimens, it was cured for 20 minutes with formwork to ensure a flat, levelled, and smooth-finished surface (Figure 4-6).

Figure 4-6. Plaster Placement on Loading Points

4.1.3 Relative Deflection Testing Fixture

During the loading tests, beam deflections were measured relative to the supports. This required the design and fabrication of a pertinent testing fixture (Figure 4-7); this consisted of two Π-shaped frames that were attached on the beam over the supports at the mid-height of the corresponding beam cross section. A 10mm thick aluminum bar was pinned at one end of the frame support with the other end being free to displace. In this manner the rigid bar defined the chord of the deflecting beam. The bar supported a spring-loaded potentiometer at midspan, measuring the deflection of the beam bottom section as the test proceeded. The potentiometer, with a gauge length of 150mm, was bearing on an L bracket which was attached upside down on the beam surface to measure deflection of the beam specimens relative to the top surface (Figure 4-12).

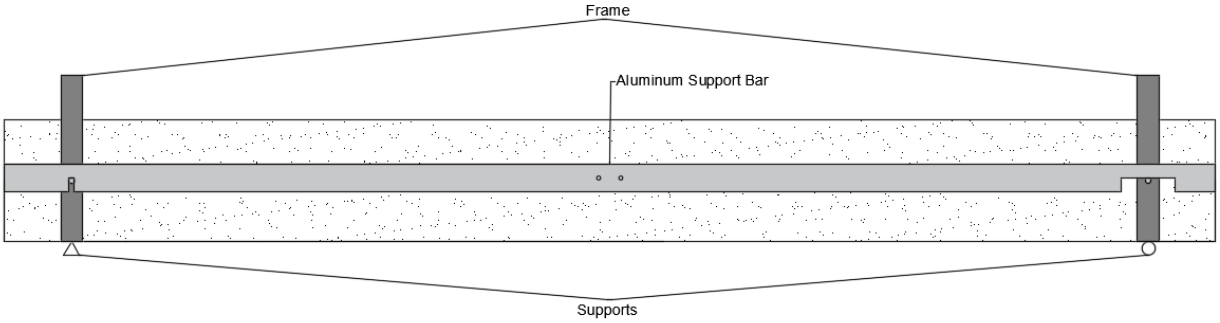

Figure 4-7. Relative Deflection Testing Fixture

4.1.4 Test Setup and Execution

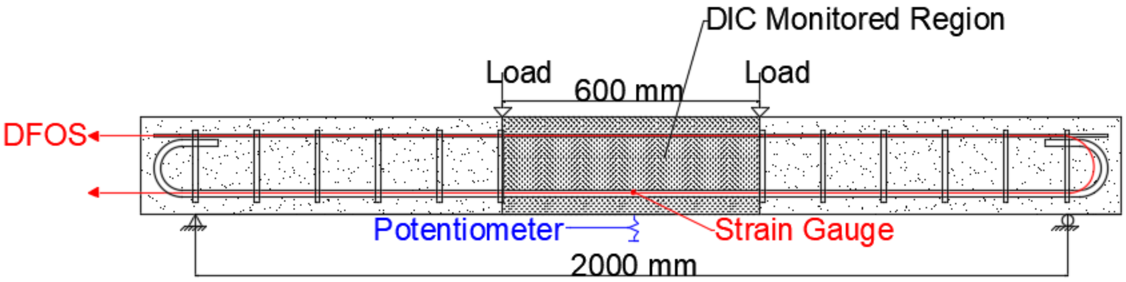

Figure 4-8. Test Setup

The four-point loading beam tests consisted of a clear span of 2000mm and a constant moment region of 600mm (nearly 1/3 of the total span, Figure 29). Two 2-inch rockers were bolted on the spreader beam 600mm apart and another two were clamped to the top of the support beam 2000mm apart - see Figure 4-9 and Figure 4-10. Clamps were used to prevent sliding of the supports during the tests. Steel plates were placed under the support rockers to accommodate for the excessive deflections of the beam specimens during the tests, to provide the necessary clearance between the bottom of the specimen and the top of the support beam.

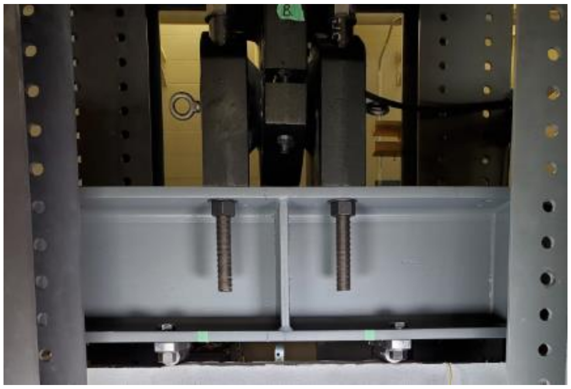

Figure 4-9. Loading Point Setup

Figure 4-10. Support Setup

The front of the beam specimens was used to take images (Figure 4-11 a)) and the back was used for measuring the relative deflection (Figure 4-11 b)). A high-resolution digital camera was used to obtain the images at every ten seconds. LED lights were used to illuminate the surface of the beam specimens to ensure the captured images were clear and visible.

Figure 4-11. a) Front of Beam and b) Back of Beam

Figure 4-12. Deflection Measurement

A Luna ODISI-B (Figure 4-13 a)) was used to obtain the DFOS data for B341.5-3, but due to complications with the interrogator, the remaining tests were conducted using the ODiSI-6104 (Figure 4-13 b)). The system was placed by the test setup to limit the free length of the standoff cable. Alignment of the system was conducted due to movement of the remote module and re-routing of the standoff cable. The alignment process ensures the correct alignment of the internal optical network of the ODISI-B.

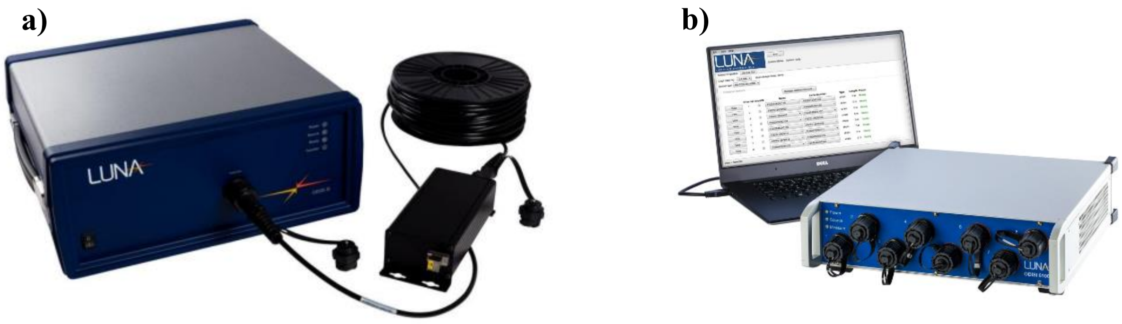

Figure 4-13. a) Luna ODISI-B and b) Luna ODiSI-6104

4.1.4.1 Test Execution and Data Acquisition

The four-point loading beam tests were conducted at a displacement-controlled rate of 0.5mm/min. Data acquisition (DAQ) was conducted through ODISI-B for strain measured using DFOS whereas a Catman DAQ software was used to acquire load, discrete strain, and displacement of the beam specimens. As previously mentioned, a high-resolution digital camera was used to obtain images for DIC. Table 4-1 shows the sampling rates corresponding to each of the measurement entities. For the most part, a sampling rate of 1hz was used to measure load, strain, and deflection. Images were taken every 10 seconds for DIC. A timer was placed above the test specimens to identify the time at which each image was captured. ODISI-B, Catman project, and camera data acquisition were initiated at exactly the same time to ensure synchronization of data.

Table 4-1. Sampling Rate for Measurement Entities

Measurement Entity	**Sampling Rate (hz)**
Actuator Load	1
Actuator Displacement	1
Potentiometer Displacement	1
Strain Gauge	1
DFOS	1
DIC	0.1

4.2 Results

4.2.1 Load-Deflection Curves and Specimen Failure Modes

Four reinforced beams were tested under four-point loading. Two reinforcement ratios of longitudinal reinforcement, ρ_s=1.5% and 2.3% and two volumetric fibre contents of v_f= 3% and

1% were the considered parameters of the study. The load-deflection response was obtained using the applied load from the actuator and the midspan displacement that was measured using a spring-loaded potentiometer. In the remainder of the present report the specimens are identified using the following code: B-N-R-100ρs-100v_f, where N ranging between 1 and 4 was the specimen number in the group; for example, B2R2.3-3 refers to the second beam specimen in the group (B2), containing 2.3% longitudinal reinforcement ratio and 3% steel fiber in the matrix.

The load-deflection response of the beams is shown in Figure 4-14, which demonstrates the effect of varying fibre content and tension reinforcement ratio on the flexural behaviour of UHP-FRC beams. The initial cracking load increased slightly with an increase in the reinforcement ratio but moderately with an increase in fibre content, which can be identified by the change of initial stiffness of the load-deflection response. The yield load was highest for B2R2.3-3 at 213kN and lowest for B1R1.5-1 at 121kN. Similarly, B2R2.3-1 attained the highest load of 241kN, but demonstrated the most brittle response, with failure occurring almost immediately after the peak load. Specimen B3R1.5-3 behaved in a similar manner, but with rupturing of longitudinal reinforcement being delayed in comparison to specimen B2R2.3-1. Beam B4R1.5-1 exhibited the lowest peak load at 157kN. Table 4-2 further highlights the milestone data of the load-deflection response of the four beam specimens. Ductility (μ) was defined as the ratio of the total displacement to the yield displacement taking at yielding of the steel reinforcement at midspan measured by the strain gauge. Table 4-2 shows that specimen B1R2.3-1 attained the highest μ at both peak load and the ultimate condition; with μ_{peak}= 1.89 and μ_{ult}= 5.09 respectively. B2R2.3-3 exhibited the lowest ductility ratio at peak and ultimate of μ_{peak}= 1.35 and μ_{ult}= 3.74, signifying its brittle behaviour. A 66% decrease in fibre content led to nearly a 27% decrease in ultimate load for both reinforcement ratios but a 40% increase in peak ductility for the ρ_s=2.3% specimens and 4.7% increase for the ρ_s=1.5% specimens.

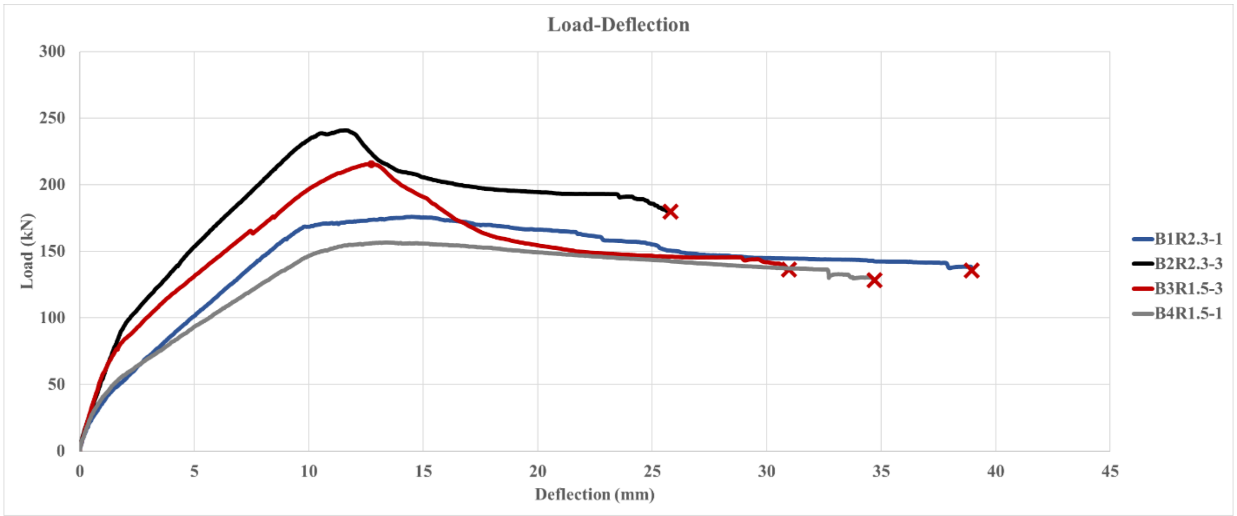

Figure 4-14. Load-Deflection Response of UHP-FRC Beams: X – Rupturing of Longitudinal Reinforcement

Table 4-2. Load-Deflection Response Values

Measurement	**B1R2.3-1**	**B2R2.3-3**	**B3R1.5-3**	**B4R1.5-1**
Yield Load (kN)	141	213	165	121
Peak Load (kN)	176	241	216	157
Δ_{yield} (mm)	7.66	8.58	7.44	7.51
Δ_{peak} (mm)	14.49	11.61	12.69	13.42
$\Delta_{ultimate}$ (mm)	38.95	32.1	30.85	34.73
μ_{peak}	1.89	1.35	1.71	1.79
μ_{Ult}	5.09	3.74	4.15	4.63

By combining the load-deflection response of the UHP-FRC beam specimens with the measured strain in the longitudinal reinforcement at midspan, the strain at different behavioural milestones can be observed. For instance, the yield displacement and load increased with an increase in fibre content and an increase in reinforcement ratio. Furthermore, although not evident for the ρ_s=2.3% reinforcement ratio specimens (B1R2.3-1 and B2R2.3-3), due to failure of the strain gauge prior to peak load, the strain at peak load was higher for B4R1.5-1 than for B3R1.5-3, demonstrating greater strain in the longitudinal reinforcement at midspan for a lower fibre content (Figure 4-15 c) and d)). Higher reinforcement strains at a given load stage prelude the onset of strain hardening in the steel reinforcement, which does not typically occur in UHP-FRC beams. This was evident with a more prolonged increase in the load carrying capacity after yielding and crack localization, in which both specimens B1R2.3-1 and B4R1.5-1 exhibited.

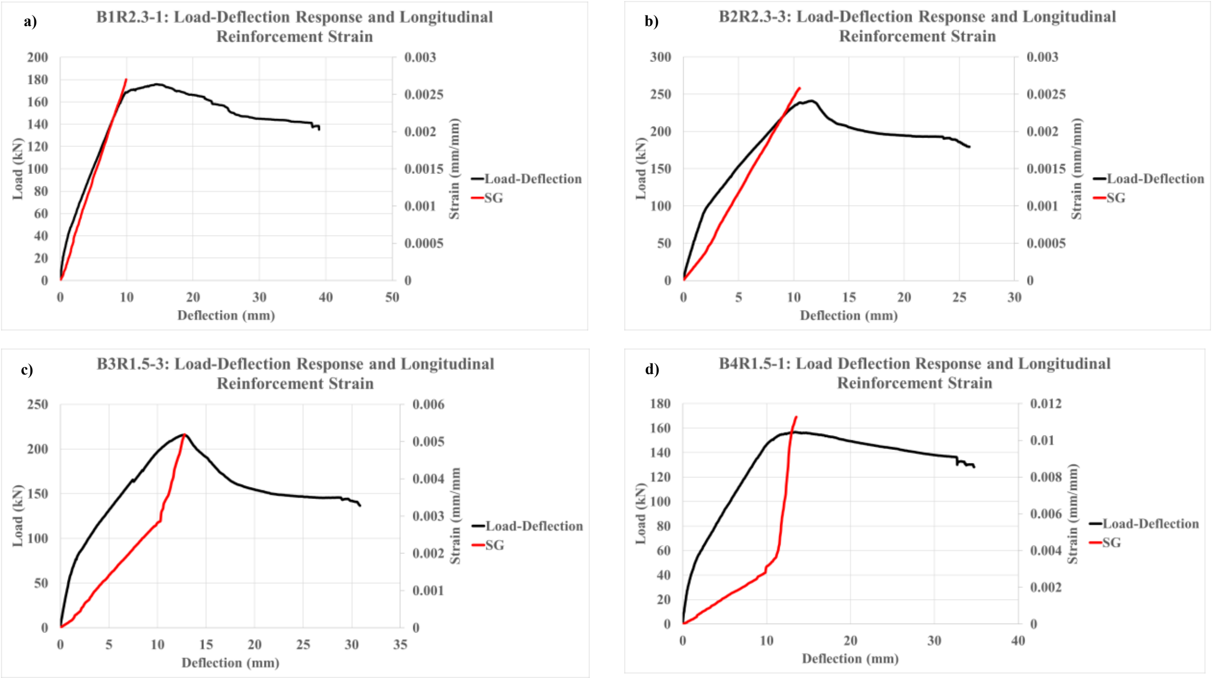

Figure 4-15. Load-Deflection Response of UHP-FRC Beam a) B1R2.3-1, b) B2R2.3-3, c) B3R1.5-3, and d) B4R1.5-1 Combined with Longitudinal Reinforcement Strain at Midspan

4.2.2 Crack Distribution of UHP-FRC Beam Specimens

Figure 4-16 illustrates the crack distribution for each of the beams at the ultimate condition. Figure 4-16 a) shows the crack distribution for B1R2.3-1, which consists of multiple cracking along the length of the beam and two localized cracks forming near the end of the constant moment region. Similar cracking was exhibited in B4R1.5-1 (Figure 4-16 d)). Both B1R2.3-1 and B4R1.5-1 primarily demonstrated flexural cracking within the constant moment region. B2R2.3-3 and B3R1.5-3 (Figure 4-16 b) and c)) both exhibited crack localization with minimal multiple cracking taking place along the length of the beam and larger crack spacing. A localized inclined crack was the major crack which formed in B3R1.5-3 under the left point load. This crack initially grew vertically, but then gradually became inclined towards the right point load. This inclined portion of the crack grew up until the midspan, where it became completely vertical directly splitting the tension zone up to the neutral axis, under the very narrow band of compression zone that developed concrete crushing. This could be a result of the loading conditions or support conditions or fibre distribution. For instance, uneven loading would eliminate the ideal conditions for four-point loading, inducing shear within the constant moment region of the beam, causing a flexure-shear crack to occur. It is noted that the supports used were rockers; therefore, longitudinal expansion of the beam owing to damage was partially restrained, inducing a possible axial load which would interfere in the beam cross-section equilibrium and might cause a mild increase in stiffness and strength. Furthermore, the fibre distribution could influence crack propagation, where cracks would grow in the direction which the UHP-FRC was weakest in tension due to non preferential fibre alignment. B2R2.3-3 had a localized crack beneath the left point load which initially propagated vertically, with a gradual inclination before becoming vertical towards the left point load at which it initially started at. Crushing of the top compression fibre occurred directly above the right localized crack for B1R2.3-1, directly to the right of the left point load for B2R2.3-3, at midspan for B3R1.5-3, and at both of the point loads for B4R1.5-1.

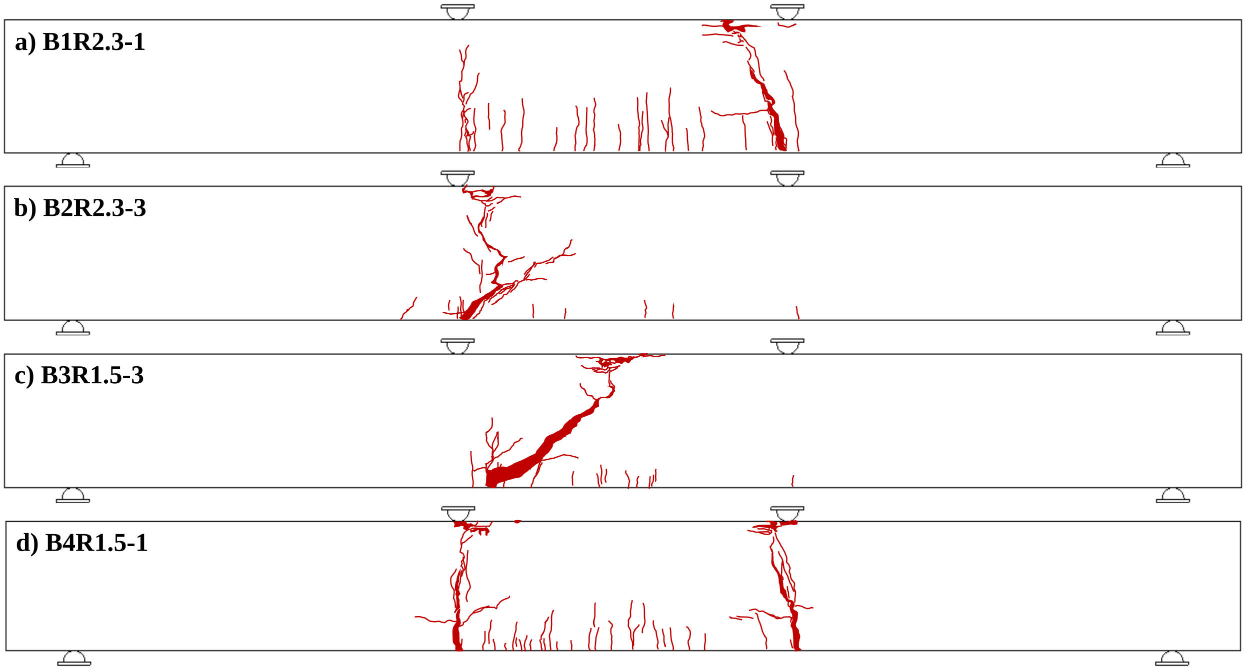

Figure 4-16. Crack Distribution for Beam Specimens a) B1R2.3-1, b) B2R2.3-3, c) B3R1.5-3, and d) B4R1.5-1

Failure of the concrete cover occurred at the bottom of the v_f=1% beam specimens (B1R2.3-1 and B4R1.5-1). This can be seen in Figure 4-17 and Figure 4-18. Bond splitting occurred in the constant moment region, adjacent of the right point load in B1R2.3-1 (Figure 4-17). Similarly, bond splitting occurred within the constant moment region for B4R1.5-1, adjacent to the left point load (Figure 4-18). No bond splitting occurred in the v_f=3% specimens, B2R2.3-3 and B3R1.5-3.

Figure 4-17. Bond Splitting in Bottom Cover of B1R2.3-1

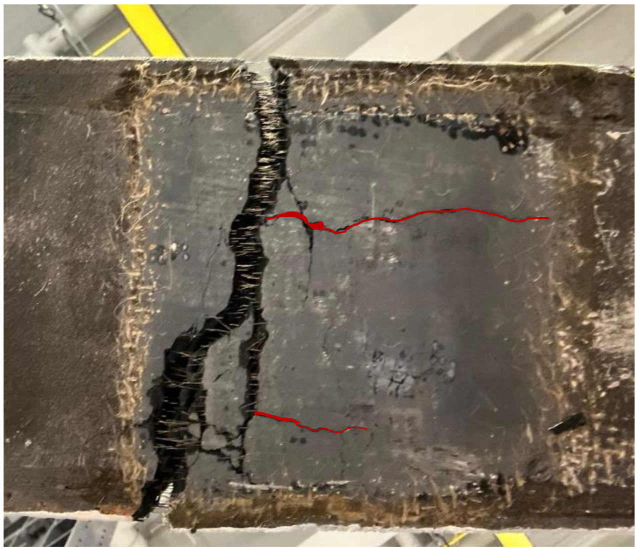

Figure 4-18. Bond Splitting of Bottom Cover of B4R1.5-1

4.2.3 DFOS Data for UHP-FRC Beams in Flexure

Distributed strain was measured along the longitudinal reinforcement and top support wire. The ODiSI-B was used to obtain strain data for B3R1.5-3, but due to complications with the system regarding the quality of strain data being obtained, the strain data for the remaining beams (B1R2.3-1, B2R2.3-3, and B4R1.5-1) was acquired by using the ODiSI 6104. Both hardware utilized Rayleigh backscattering based on OFDR. This section will assess, analyze, and discuss the distributed strain data at milestone points of loading, including the yield load, according with the strain gauge readings and at peak load. It should be noted that the data presented in this section was originally obtained as a frequency shift but was converted to mechanical strain using Equation 4.3, where Δu is frequency shift in GHz. Furthermore, the DFOS strain data consists of a gauge length of 2.6 mm.

$$\varepsilon = 6.67(\mu\varepsilon/GHz)\ \Delta u \qquad 4.3$$

4.2.3.1 Reinforcement Strains at Yielding

The distributed strain in the top support wire and longitudinal reinforcement were measured at yielding of the longitudinal reinforcement at midspan, which was obtained through use of a strain gauge attached to the longitudinal reinforcement at the exterior face at the tipoff horizontal diameter of the bar. Yielding of the reinforcement took place over a distributed length. No signs of significant cracking were evident in the distributed strain data along the longitudinal reinforcement due to the lack of spikes in the strain gradient. This led to a more constant/consistent strain within the length where yielding took place. Therefore, the onset of the development of plasticity was spread along a length rather than occurring at a localized point. The reinforcement strain at yielding was highest for B3R1.5-3, with a strain of 0.00225mm/mm (Figure 4-21) and lowest for B1R2.3-1 (0.00185mm/mm) (Figure 4-19). The ρ_s=1.5% and v_f=1% combination led to a higher longitudinal reinforcement strain at bar yielding. Yielding of reinforcement was not limited to the constant moment region where higher curvatures were expected, but penetrated in the shear span. Furthermore, at the yield load, the shape of the strain distribution of the top support wire was near trapezoidal and similar to the shape of the bending moment diagram consistent with four-point loading (Figure 4-19, Figure 4-20, Figure 4-21, and Figure 4-22). Due to the relatively lower magnitude (10 times smaller than strain in tension) of the compressive strain in the top support wire, it was evident that the yielding of reinforcement occurred much prior to the crushing of concrete in the extreme compression fibre. At this point of loading, its was evident that the left point load was applying more load than the right. This was identified by there being a decrease in compressive strain in all four beams near the left load (Figure 4-23).

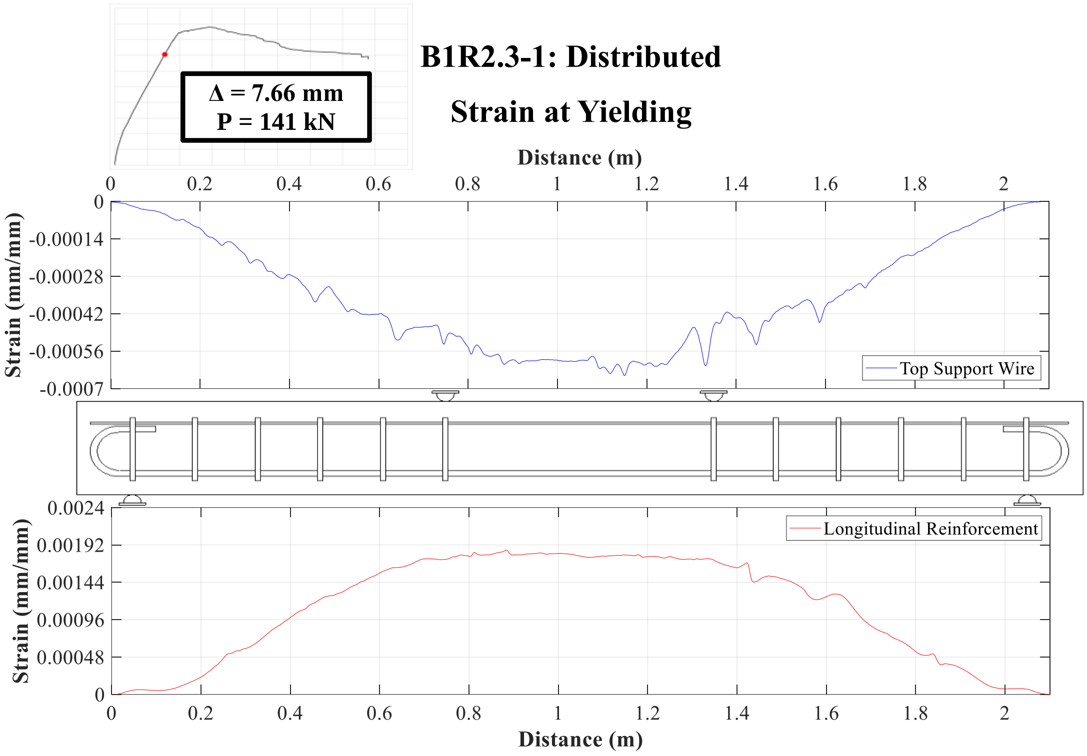

Figure 4-19. B1R2.3-1: Distributed Reinforcement Strain at Yielding

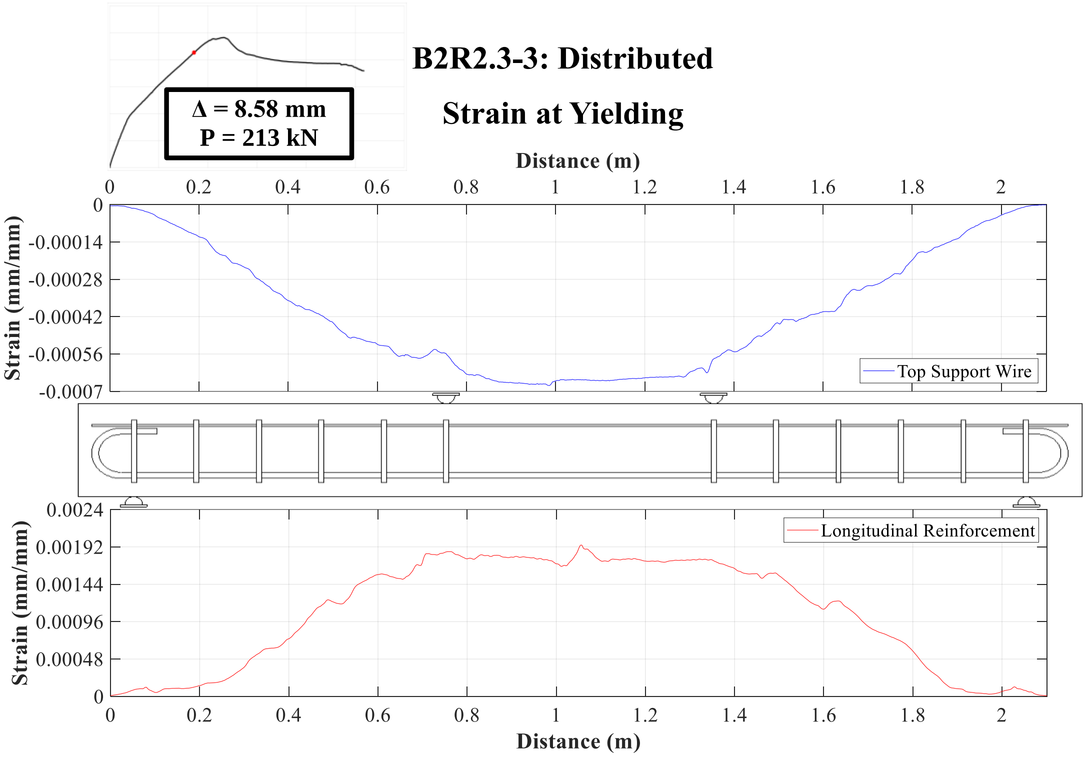

Figure 4-20. B2R2.3-3: Distributed Reinforcement Strain at Yielding

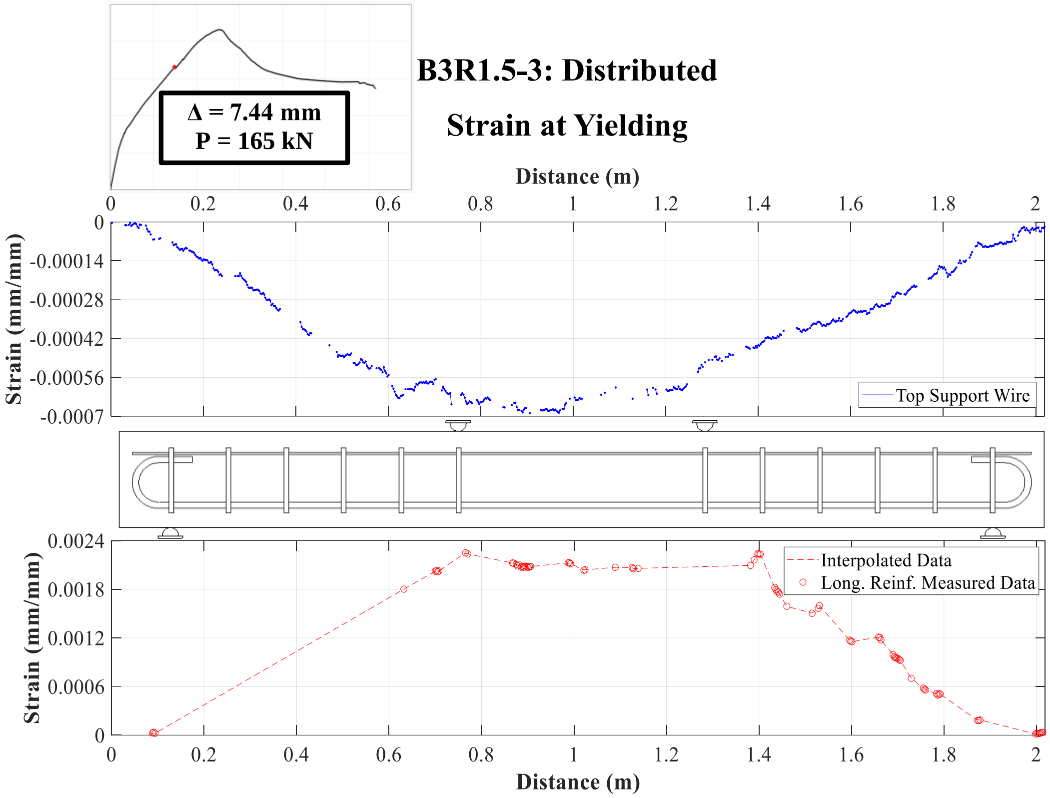

Figure 4-21. B3R1.5-3: Distributed Reinforcement Strain at Yielding

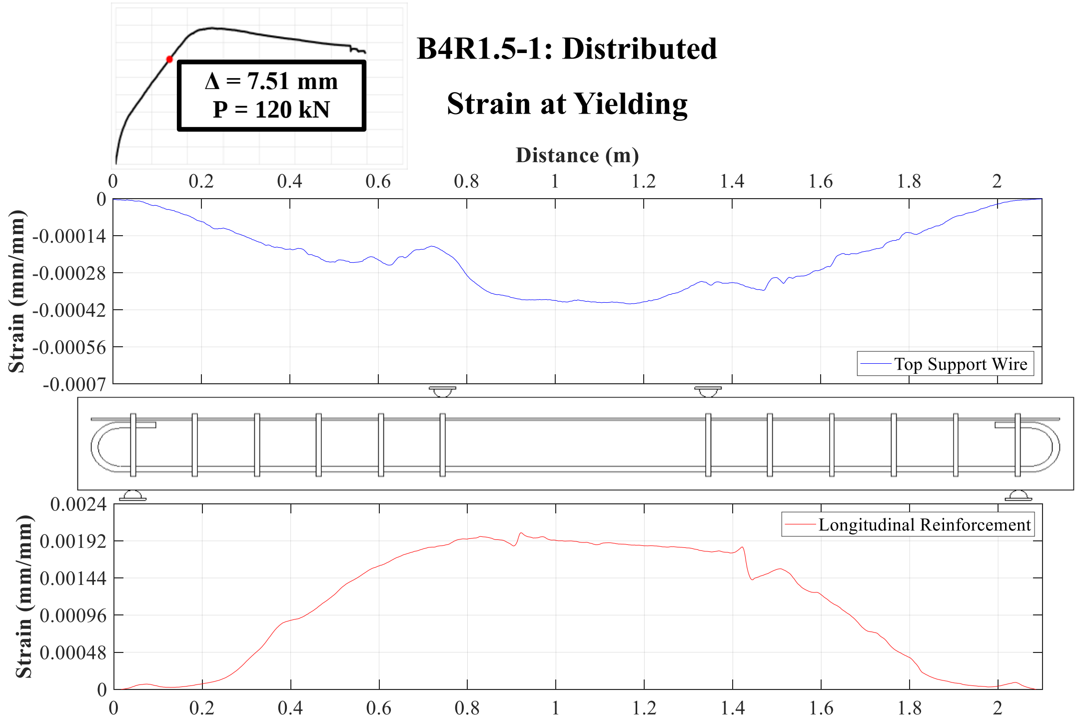

Figure 4-22. B4R1.5-1: Distributed Reinforcement Strain at Yielding

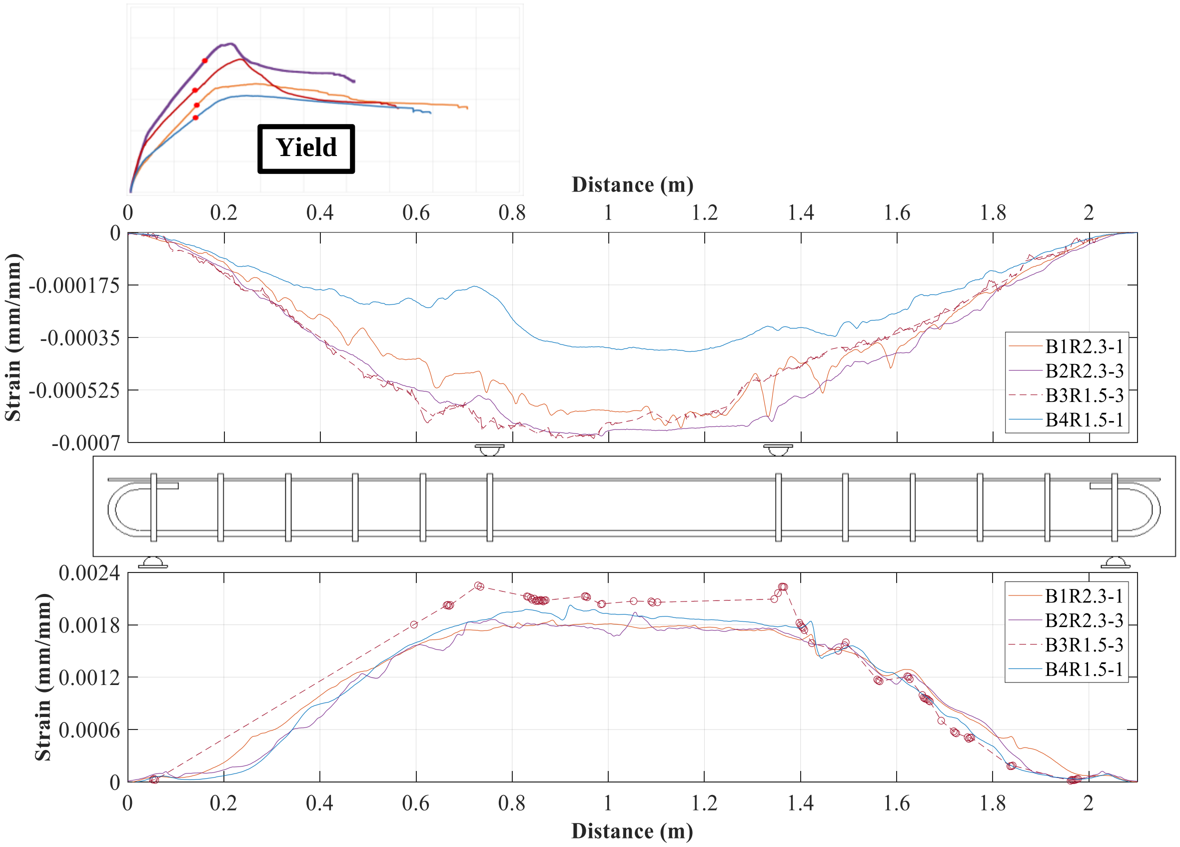

Figure 4-23. Comparison of Distributed Strain at Yield Load

The length of yielding varied between beam specimens. This was defined by the region(s) at which the longitudinal reinforcement strain exceeded that of yielding. A decrease in fibre content and reinforcement ratio led to an increase in yield length. For instance, the yield length was highest for B4R1.5-1 (746.2 mm) and lowest for B2R2.3-3 (5.2 mm). With a portion of the reinforcement demonstrating strains that exceeded the yield strain, it was evident that yielding of reinforcement occurred at a lower load and did not necessarily initiate at midspan. This is summarized in Figure 4-24.

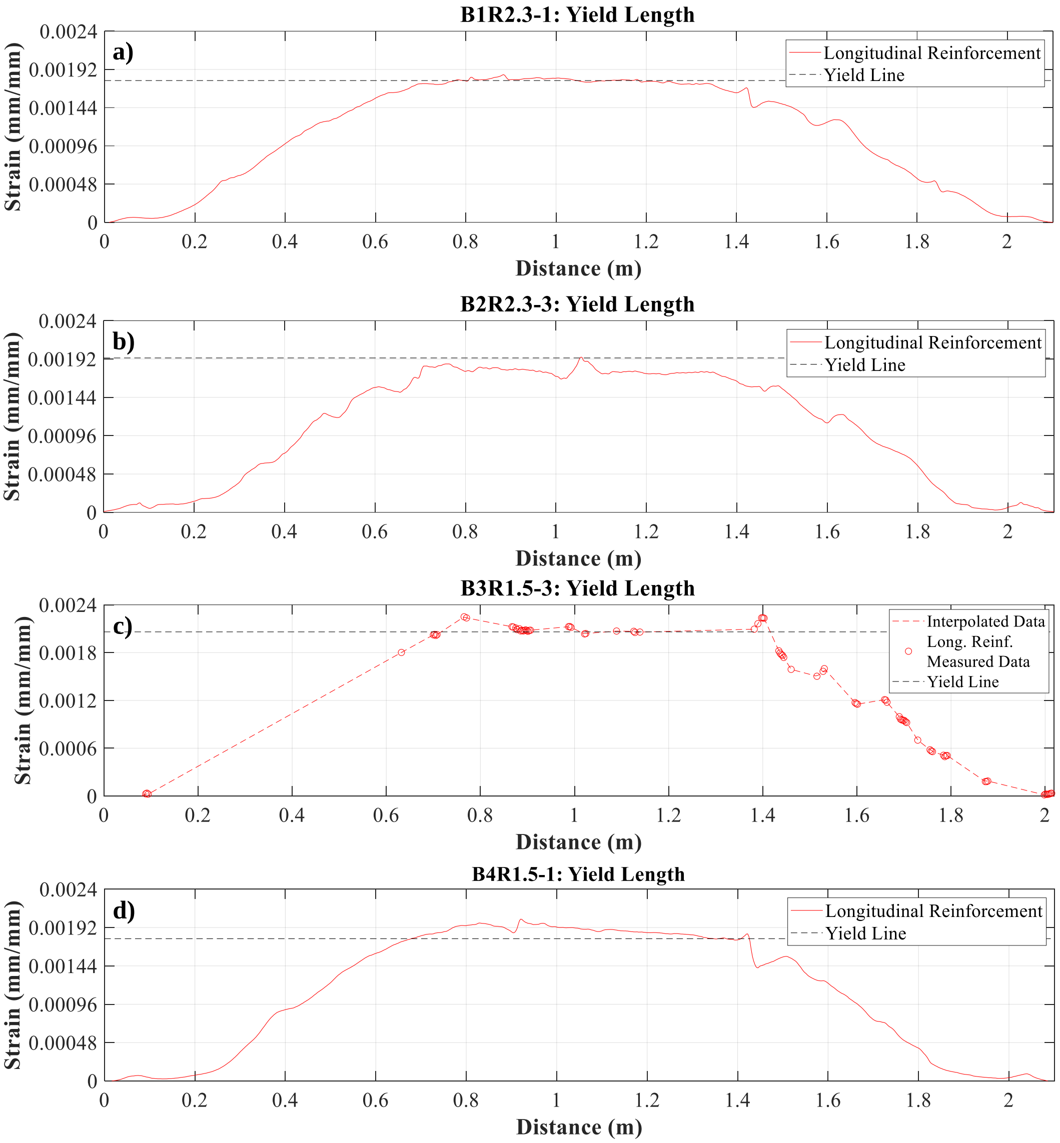

Figure 4-24. Yield Length for a) B1R2.3-1, b) B2R2.3-3, c) B3R1.5-3, and d) B4R1.5-1

4.2.3.2 Reinforcement Strains at Peak Load

At the point of the peak load, much of the longitudinal reinforcement was within the plastic range of elongation for each of the beams, but to different extents depending on the specimen characteristics. For B1R2.3-1 (Figure 4-25), much of the longitudinal reinforcement strain exceeded the yield strain. Cracking could be identified through sharp increases in the strain gradient of the rebar in tension leading to a maximum strain in tension of 0.00755mm/mm near the right point load. This would eventually become the location at which longitudinal reinforcement rupturing took place. At this point in loading, there was no evidence of compressive crushing especially due to the lower magnitude of the top support wire strains. The distributed strain in the top support wire decreased in compression where the sharp increases in the strain gradient occurred in the bottom longitudinal reinforcement. B2R2.3-3 (Figure 4-26) demonstrated significantly lower strains at peak load in comparison to B1R2.3-1, with a maximum strain of 0.00386mm/mm. There were fewer spikes in the strain gradient, signifying less cracking in comparison to B1R2.3-1 due to the increase in fibre content. The corresponding strain in the top support wire exhibited a peak strain of -0.000762mm/mm. There was a decrease in compressive strain at the location corresponding to the highest strain in tension in the longitudinal reinforcement, which was a result of shifting of the neutral axis, where cracking caused the neutral axis to shift upwards. This increased the strain in tension but decreased the DFOS strain in compression, owing to the greater proximity of the DFOS to the neutral axis. Similar behaviour in compression was exhibited in B3R1.5-3 (Figure 4-27), where the compressive strain in the top support wire decreased in compression at the location corresponding to the localized crack. Due to a lack of reliable strain data in the longitudinal reinforcement, the limited data which could be obtained was plotted with linear dashed segments which interpolate the values in between known data points. Therefore, for this case, the tensile strain distribution along the longitudinal reinforcement was not representative of the true distribution which might actually be demonstrated by the bar in tension. For instance, in Figure 4-16. c), it is evident that there is a major localized crack under the left applied point load. It would be reasonable to assume that there would be a spike in the strain gradient at the location of the crack, but this could not be captured by the lack of data. Therefore, by the strain in the top support wire decreasing at the crack location, it signifies that the maximum tensile strain would be taking place at the crack location. Furthermore, upon inspection of B3R1.5-3, this was the location of rupturing of the rebar, confirming that reinforcement strain at the localized crack was the highest along the entire length of the beam. With the lack of distributed strain data along the length of the longitudinal reinforcement for B3R1.5-3, there was still evidence of limited plasticity in the known data points, with a maximum measured value of tensile strain of 0.00298mm/mm. B4R1.5-1 (Figure 4-28) demonstrated a maximum tensile strain of 0.00568mm/mm near midspan. A significant increase in the strain gradient was evident under the left applied point load where a major localized crack formed, but its plateau was not captured due to the loss of strain data, which was a result of higher strain gradients, signifying this being the likely location of the maximum tensile strain. The corresponding top support wire strain at the location of the left major crack goes into tension, signifying that the depth of the neutral axis is above the top support wire at this location, and thus verifying a sharp increase in strain. This location also corresponds to the location of rupturing of the longitudinal reinforcement, further confirming the strain would be highest at the localized crack and not near midspan. A decrease in fibre content led to more locations along the length of the longitudinal reinforcement exhibiting higher strains in comparison to a single sharp increase in strain at a localized point due to crack localization. Between bar sizes, it was evident that larger bar sizes demonstrated lower reinforcement strains along the bar length in comparison to the smaller bar size.

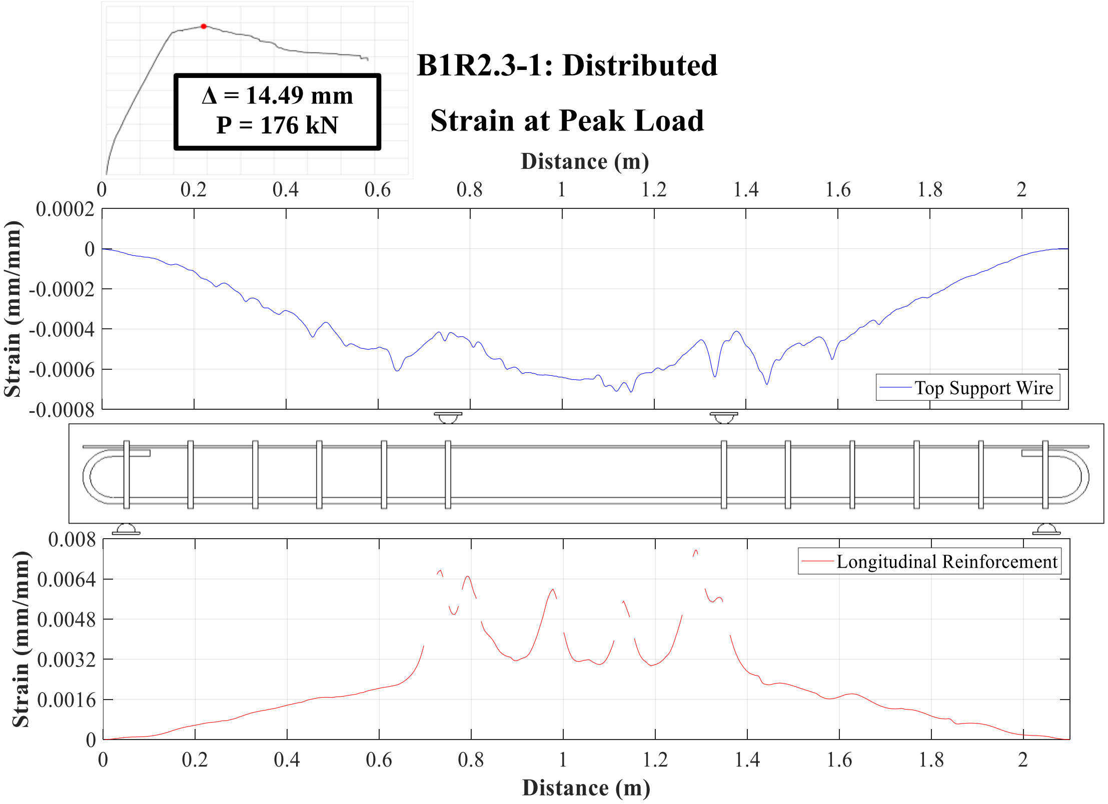

Figure 4-25. B1R2.3-1: Distributed Strain at Peak Load

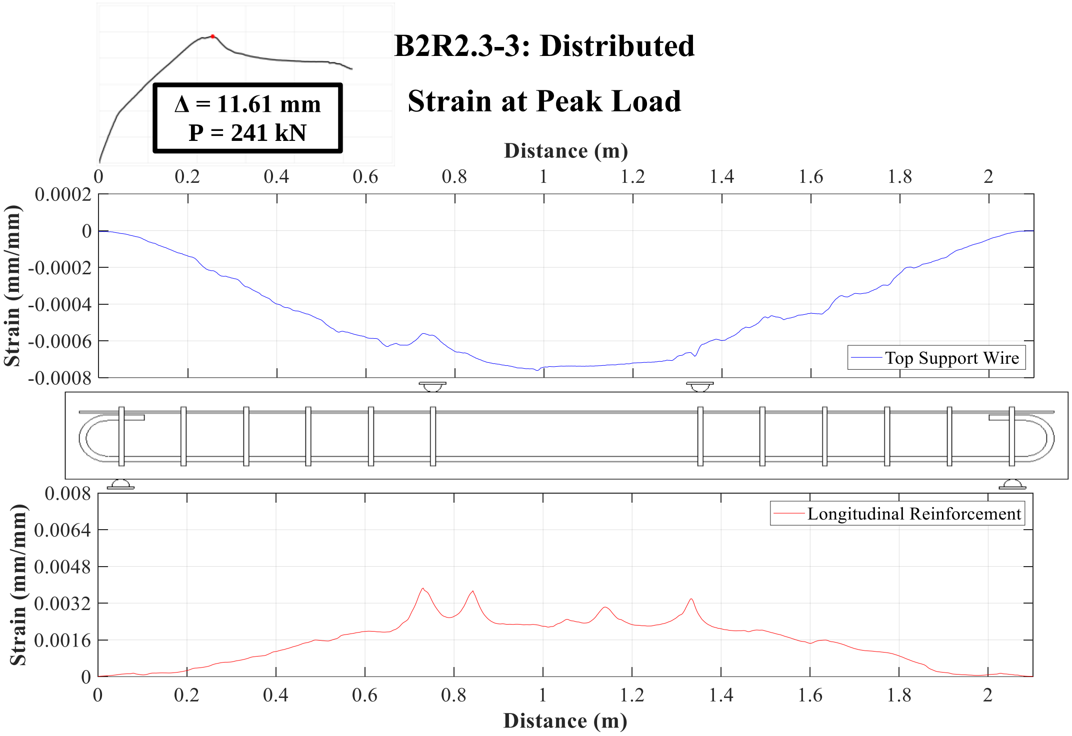

Figure 4-26. B2R2.3-3: Distributed Strain at Peak Load

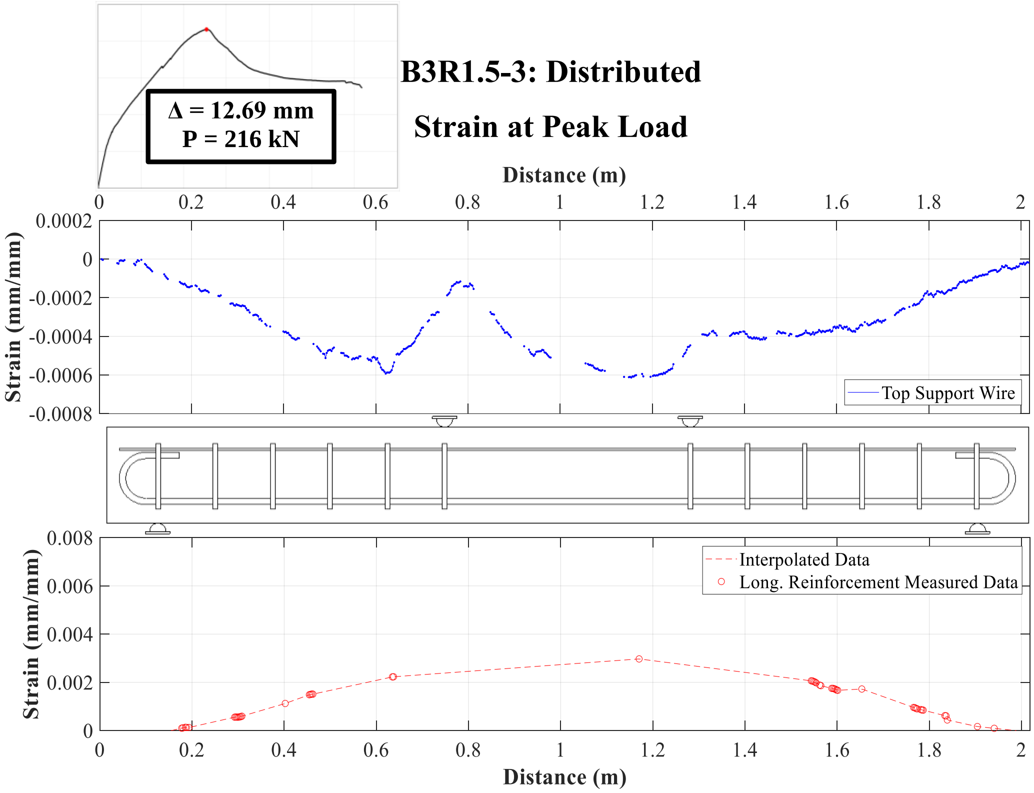

Figure 4-27. B3R1.5-3: Distributed Strain at Peak Load

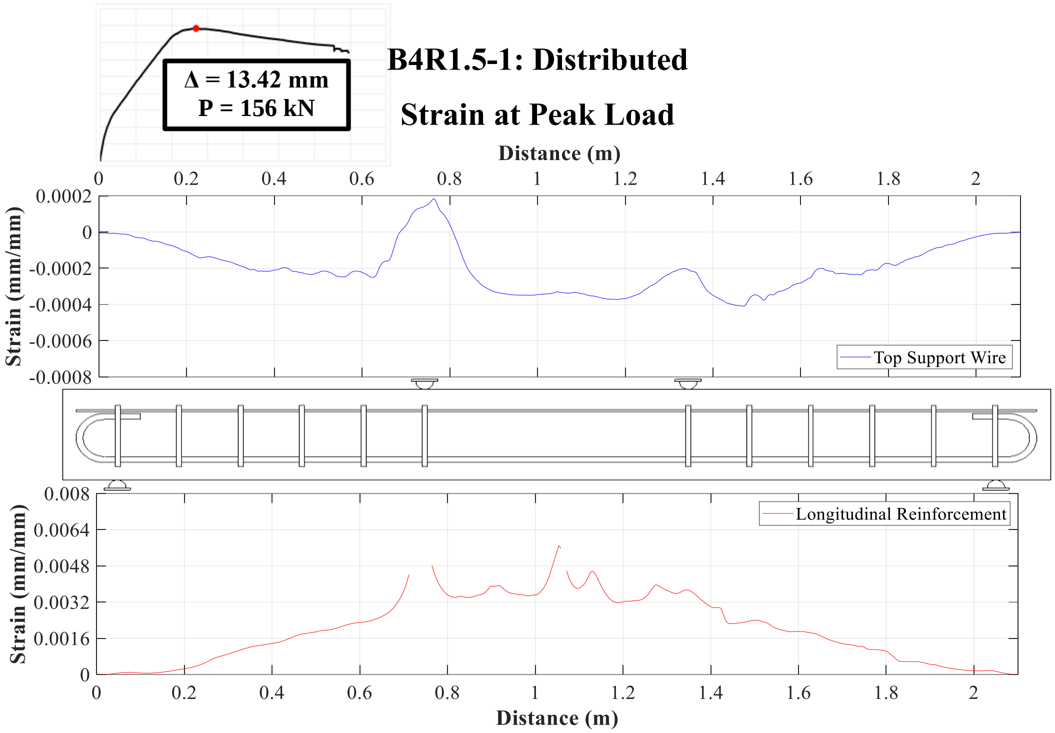

Figure 4-28. B4R1.5-1: Distributed Strain at Peak Load

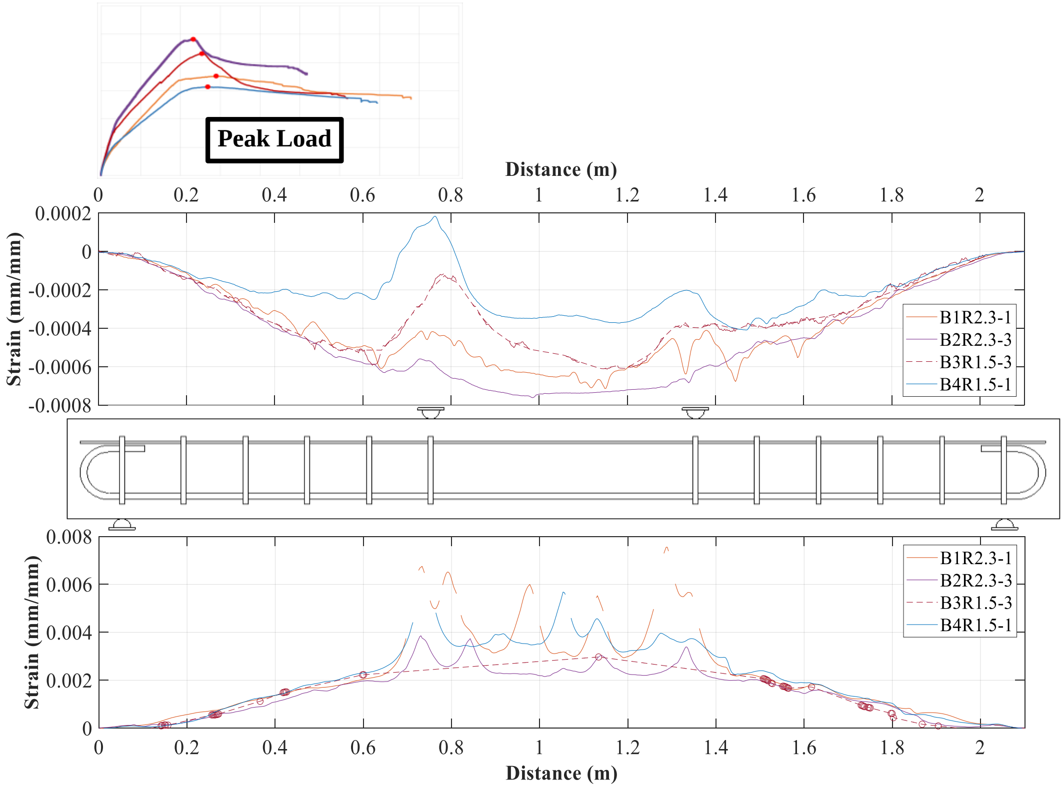

Figure 4-29. Comparison of Distributed Strain at Peak Load

4.2.3.3 Curvature and Depth of the Neutral Axis along Beam Length at Peak Load

The curvature along the length of the beam specimens was calculated by subtracting the top wire strain from the bottom longitudinal reinforcement strain and dividing by the distance between the top and bottom DFOS. Due to a lack of strain data along the longitudinal reinforcement for B3R1.5-3, the curvature could not be calculated. Figure 4-30 illustrates the curvature along each of the beam specimens, where B1R2.3-1 (Figure 4-30 a)) demonstrated the highest peak curvature and B2R2.3-3 (Figure 4-30 b)) demonstrated the lowest peak curvature. Similar to the effects of cracking on longitudinal tensile strains, the curvature distribution demonstrated sharp increases in curvature at the cracks. The curvature distribution was identical to the strain distribution of the longitudinal reinforcement. Table 4-3 provides the average curvature along the length of the beam specimens, where B1R2.3-1 demonstrates the highest average curvature of 7.98x10^{-6}mm^{-1}, signifying overall greater rotations and thus displacements. Adversely, B2R2.3-3 demonstrates a lower average curvature of 5.9x10^{-6}mm^{-1}, signifying lower rotations and deflection.

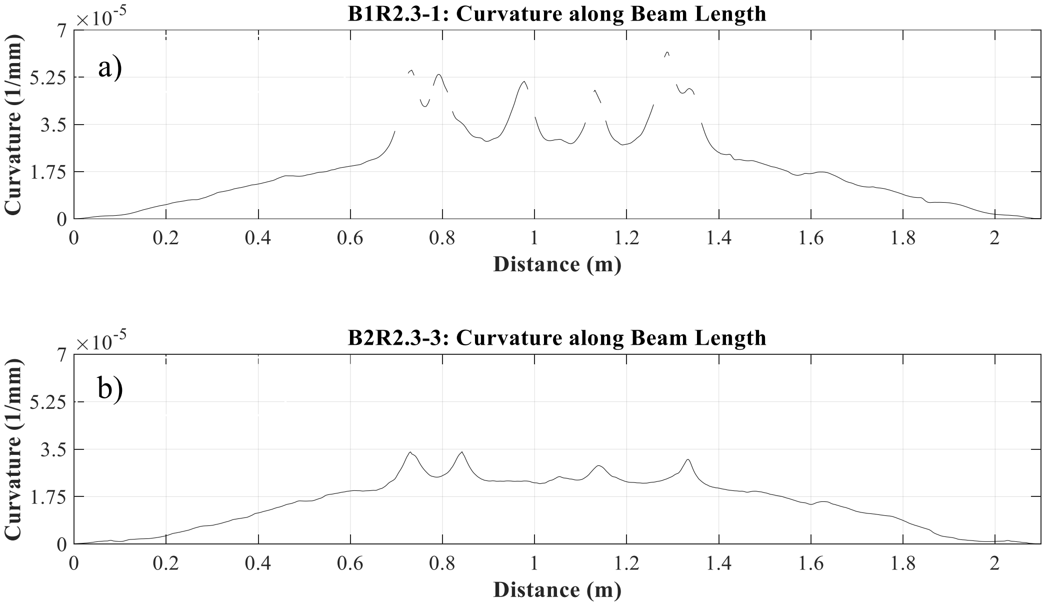

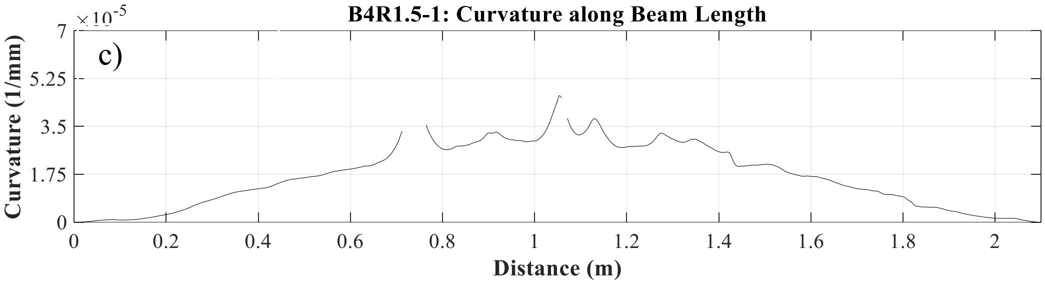

Figure 4-30. Curvature along Beam Length a) B1R2.3-1, b) B2R2.3-3, and c) B4R1.5-1

Table 4-3. Average Curvature of Beam Specimens

Specimen ID	**B1R2.3-1**	**B2R2.3-3**	**B3R1.5-3**	**B4R1.5-1**
Average Curvature (1/mm)	7.98E-06	5.9002E-06	N/A	7.0731E-06

The depth of the neutral axis was calculated by subtracting the ratio of the bottom longitudinal reinforcement strain to the curvature from the effective depth of the beam specimen. Again, due to the lack of strain data for B3R1.5-3, the depth of the neutral axis could not be calculated. Overall, there were no significant changes in the depth of the neutral axis along the length of the beam specimens, with the neutral axis falling between 40mm and 75mm within the constant moment region for the three beams. Figure 4-31 plots the depth of the neutral axis for each of the beam specimens. The depth of the neutral axis was closest to the top compressive fibre in the constant moment region where much of the cracking took place. Near the location of the supports, the depth of the neutral axis shifted downwards to the bottom tension fibre. for B2R2.3-3 (Figure 4-31 b)) and B4R1.5-1 (Figure 4-31 c)). B4R1.5-1 exhibited the highest depth of the neutral axis at peak load. Furthermore, the depth of the neutral axis peal load was lowest for B2R2.3-3. Slight decreases in the depth of the neutral axis signify the transitioning between cracked and uncracked sections along the length of the beams. Where the neutral axis is closest to the top compressive fibre at the location of a crack and closest to the bottom tension fibre at locations between cracks.

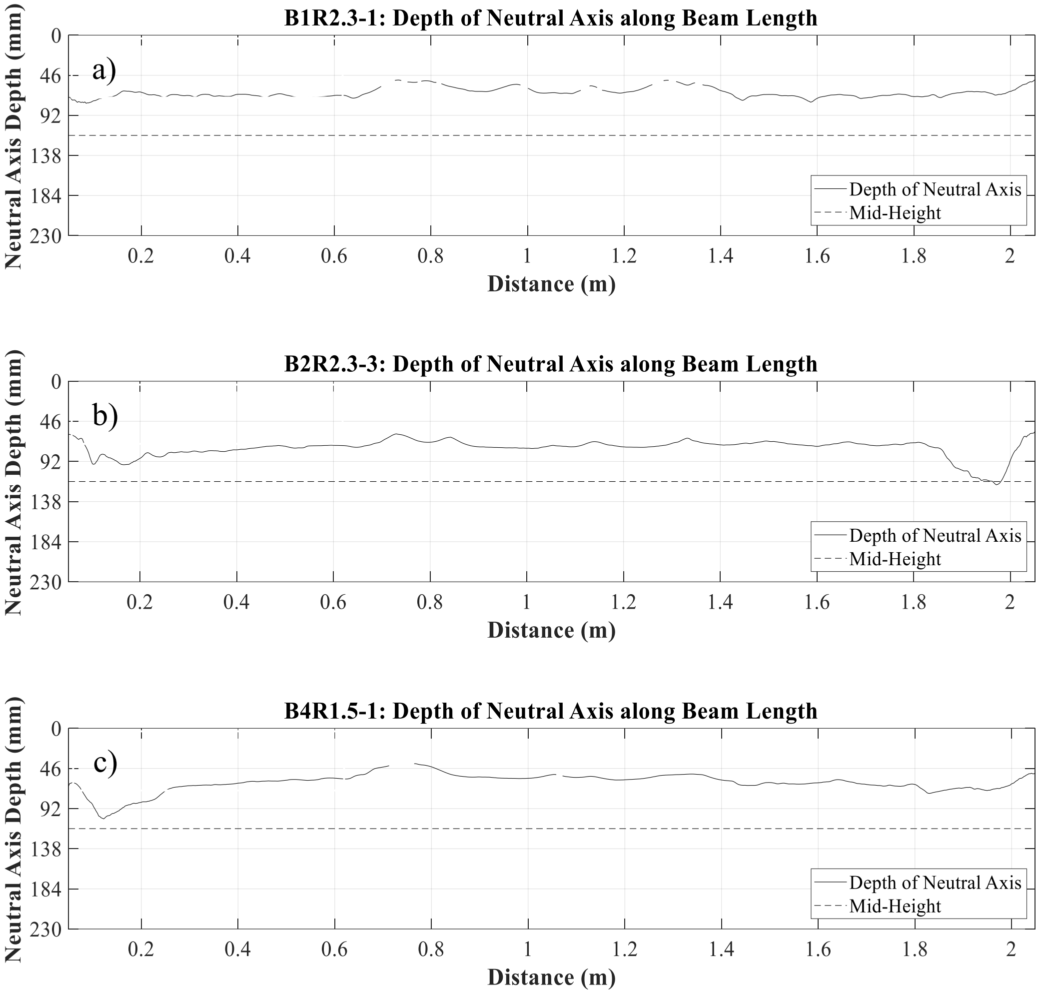

Figure 4-31. Position of the Neutral Axis at Peak Load a) B1R2.3-1, b) B2R2.3-3, and c) B4R1.5-1

4.2.4 Strain Gauge-DFOS Comparison at Midspan

Longitudinal Reinforcement strain at midspan was measured using a strain gauge to verify the strain being measured at midspan with the DFOS. Differences in the midspan strain measured by the strain gauge and DFOS are observed in Figure 4-32, Figure 4-33, Figure 4-34, and Figure 4-35. As time increases, there is a nearly linear increase in the difference in strain measured by the DFOS and strain gauge, which corresponds to higher deflections. At lower deflections, the strain measured by the DFOS and strain gauge were near identical, but as the deflections increased, so did the strain difference. This strain difference was induced by the increase in curvature as the beam specimens were loaded, which can be calculated by multiplying the difference in vertical position between the DFOS and strain gauge with the curvature at a given instance in time. When increasing the bar size from 15M to 20M, there is a slight increase in strain difference due to curvature which results from the increase in the vertical distance between the locations of the DFOS and strain gauge. It should be noted that due to the lack of distributed strain data for the longitudinal reinforcement for B3R1.5-3, the strain difference due to curvature was not obtained in Figure 4-34. Figure 4-36 demonstrates the difference in strain due to curvature. When comparing the strain difference calculated from curvature with the values obtained by subtracting the DFOS-measured strain from the strain gauge-measured strain, it is evident that they both follow an identical linear trend.

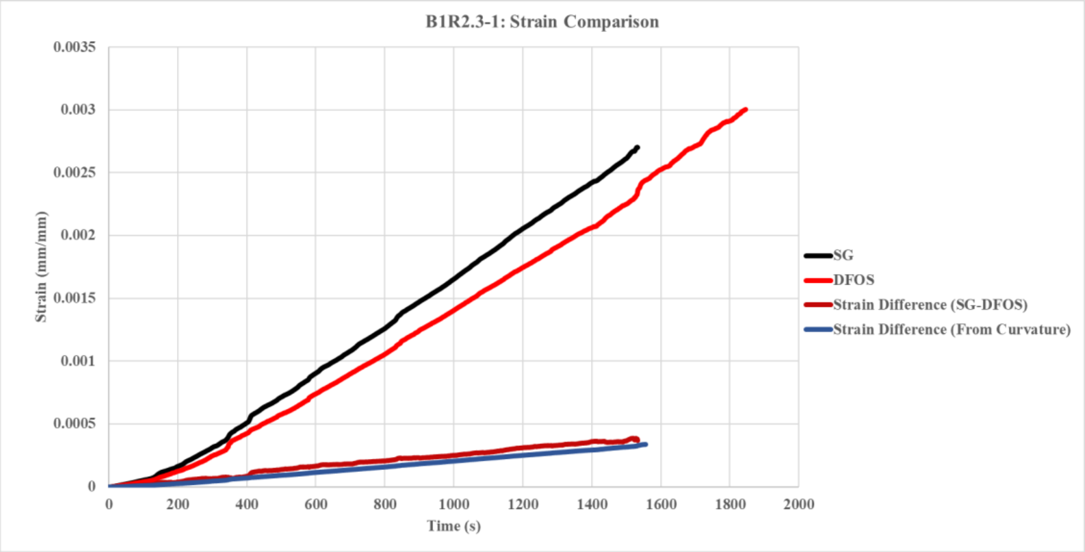

Figure 4-32. B1R2.3-1 Strain Comparison

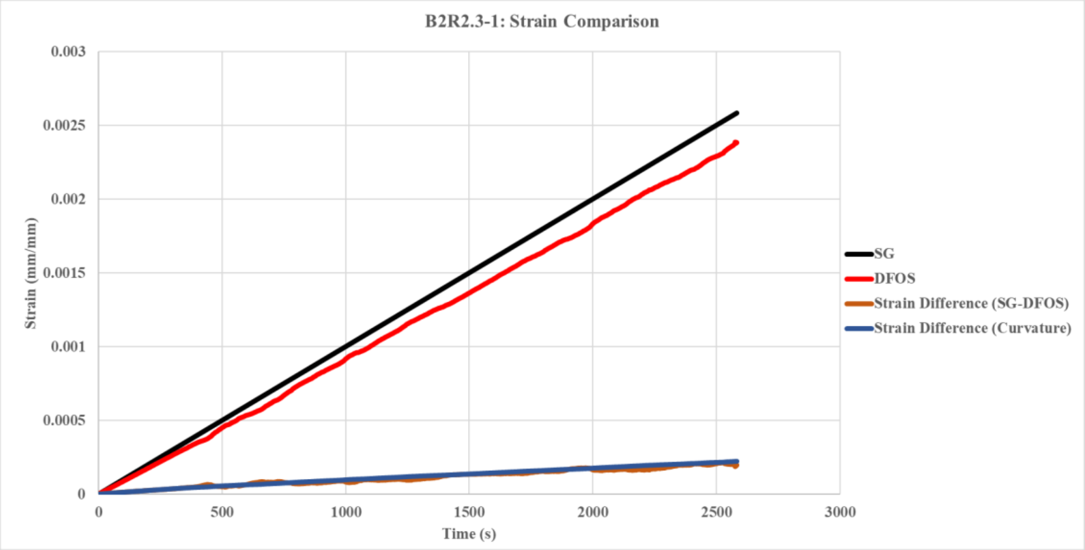

Figure 4-33. B2R2.3-3 Strain Comparison

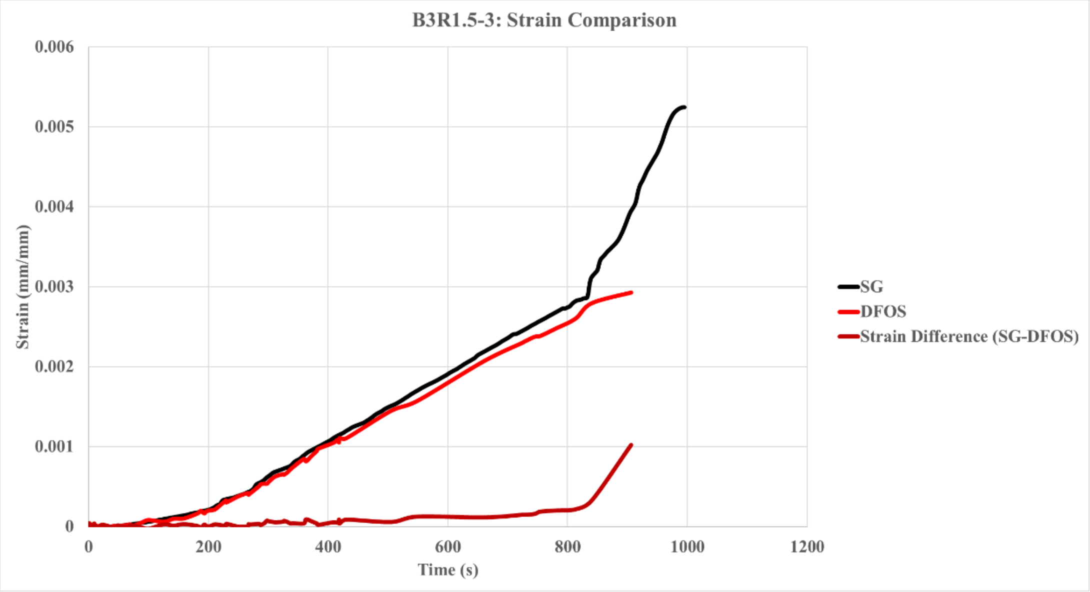

Figure 4-34. B3R1.5-3 Strain Comparison

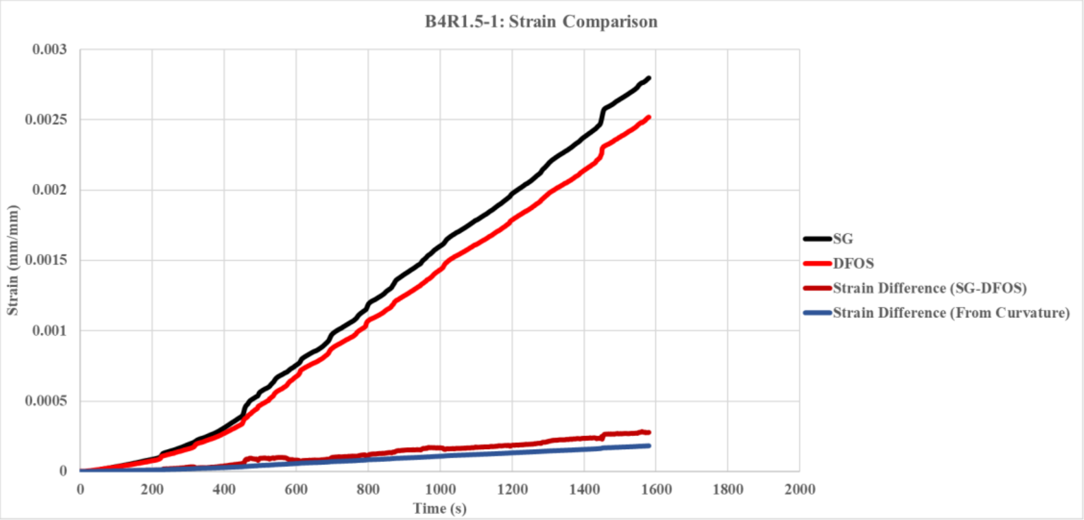

Figure 4-35. B4R1.5-1 Strain Comparison

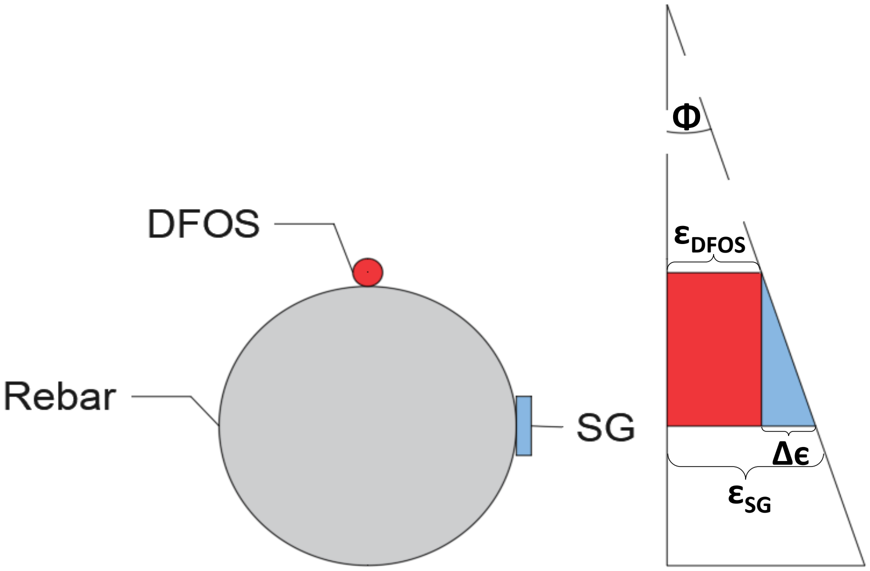

Figure 4-36. Strain Difference due to Curvature

4.2.5 Plastic Length and Strain Penetration of Steel Reinforcement

The structural definition of a plastic hinge is the region of a reinforced concrete beam where the bending moment in the beam is greater than that of the yield moment, causing plastic rotation to develop. The plasticity length is the length where reinforcement strains exceed the yield strain. The plastic length of the reinforcement in the beams was defined from the distance over which the measured distributed strains in the reinforcement exceeded that of the yield strain. Due to the difference in strain measured from the DFOS and strain gauge, the DFOS strain which corresponded to the yield strain measured by the strain gauge was used to define the yield line. The yield strain of 0.0021 mm/mm was determined by the uniaxial tension tests conducted on the rebar used for the longitudinal steel in the beam specimens as presented in 3.5.3.

The reinforcement plastic length was measured at the peak load for each of the four beam specimens. This is demonstrated in Figure 4-38, Figure 4-40, Figure 4-42, and Figure 4-44. When assessing the difference in plastic length of the reinforcement between different bar sizes, there was a decrease in plastic length for the 20M bar size. This was consistent for both fibre contents. For instance, B4R1.5-1 had a measured plastic length at peak load of 1177.8 mm, whereas B1R2.3-1 had a measured plastic length at peak load of 1014 mm; a 13.9% decrease in plastic length. B3R1.5-3 has a measured plastic length of 950.9 mm and B2R2.3-3 has a 2.9% decrease in plastic length with a value of 923 mm. Between varying fibre contents for a given bar size, the v_f=1%

specimens, B1R2.3-1 and B4R1.5-1 demonstrated greater plastic lengths than the v_f=3% specimens B2R2.3-3 and B3R1.5-3, with a 9.9% increase in plastic length for ρ_s = 2.3% and a 23.9% increase in plastic length for ρ_s = 1.5%. Decreasing the fibre content by 66.7% had a more pronounced impact, increasing the plastic length.

The plastic length defined by the distance in which the bending moment exhibited by the beam exceeds that of the yield moment is displayed in Figure 4-37, Figure 4-39, Figure 4-41, and Figure 4-43. It should be noted that the yield moment was defined the by load corresponding to the time instance at which the strain gauge at midspan measured a yield strain of 0.0021 mm/mm. Between fibre contents with a consistent reinforcement ratio, there was an increase in the total plastic length from 761.6 mm (v_f=3%) to 878.7 mm (v_f=1%) for ρ_s = 2.3%, consistent with the reinforcement plastic length measured by the DFOS. But, for ρ_s = 1.5%, there was a slight decrease in plastic length when transitioning from a fibre content of 3% to 1%, which is opposite to what was observed in the reinforcement plastic length measured by the DFOS. This inconsistency can be due to the lack of distributed strain data in the DFOS at the longitudinal reinforcement. Since the lack of data in B3R1.5-3 required the use of linear interpolation between known data points, the plastic length cannot be accurately determined due to the true shape of the strain distribution along the length of the beam not being captured by the DFOS.

When comparing the plastic length measured by the DFOS with that defined by $M>M_Y$, the plastic length measured by the DFOS was larger for each beam specimen. The structural definition of the plastic length was determined through statics, by utilizing the bending moment diagram of the beam specimen and observing the length at which it exceeds the yield moment of the beam specimen. The plastic length measured by the distributed strains of the longitudinal reinforcement was a materials-based approach, which relied on the material properties of the steel reinforcement and considered the interaction between the cementitious matrix and steel reinforcement, which was heavily influenced by varying fibre contents in UHP-FRC.

Table 4-4. Measured Plastic Length

Measurement	**B1R2.3-1**	**B2R2.3-3**	**B3R1.5-3**	**B4R1.5-1**
Total Reinforcement Plastic Length (mm)	1014	923	950.9	1177.8
Total Structural Plastic Length ($M>M_Y$) (mm)	876.6	761.6	926.4	922

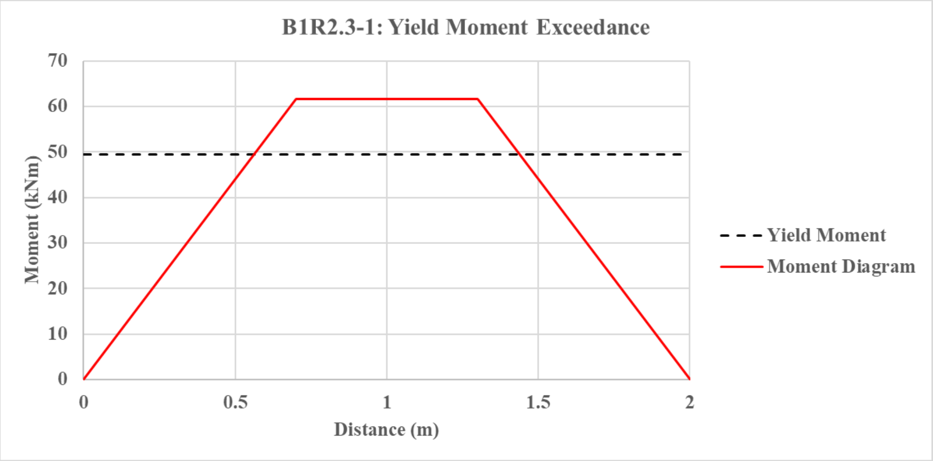

Figure 4-37. B1R2.3-1: Structural Plastic Length

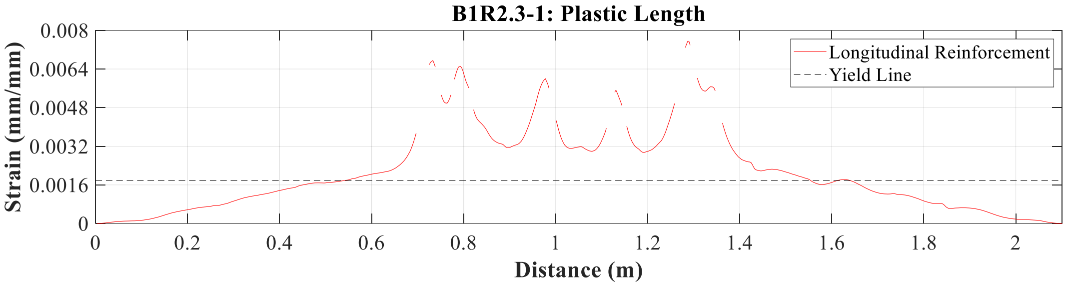

Figure 4-38. B1R2.3-1: Reinforcement Plastic Length

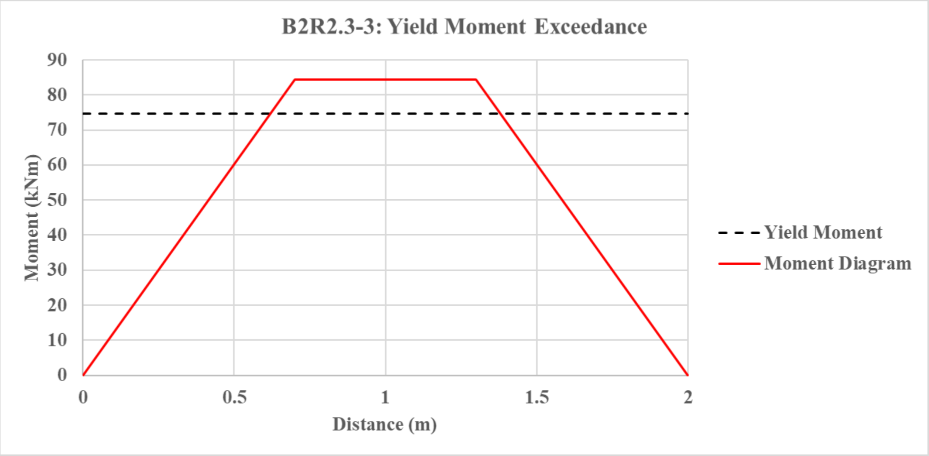

Figure 4-39. B2R2.3-3: Structural Plastic Length

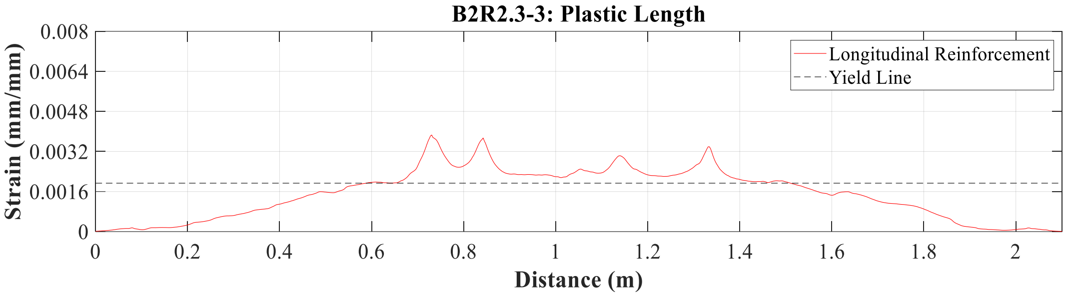

Figure 4-40. B2R2.3-3: Reinforcement Plastic Length

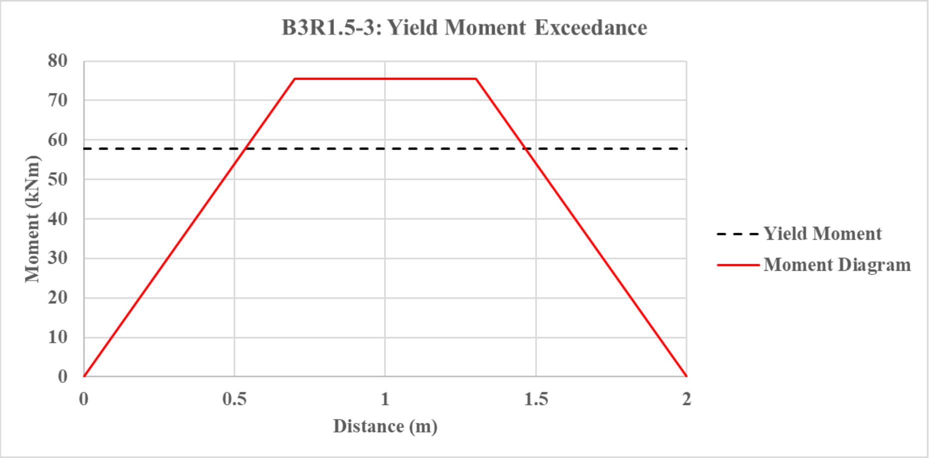

Figure 4-41. B3R1.5-3: Structural Plastic Length

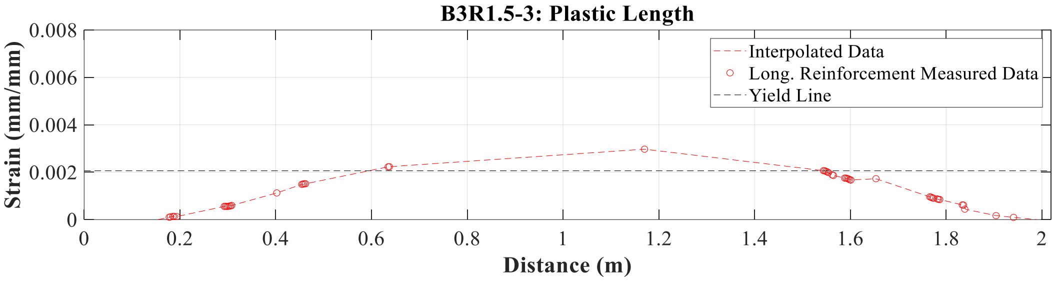

Figure 4-42. B3R1.5-3: Reinforcement Plastic Length

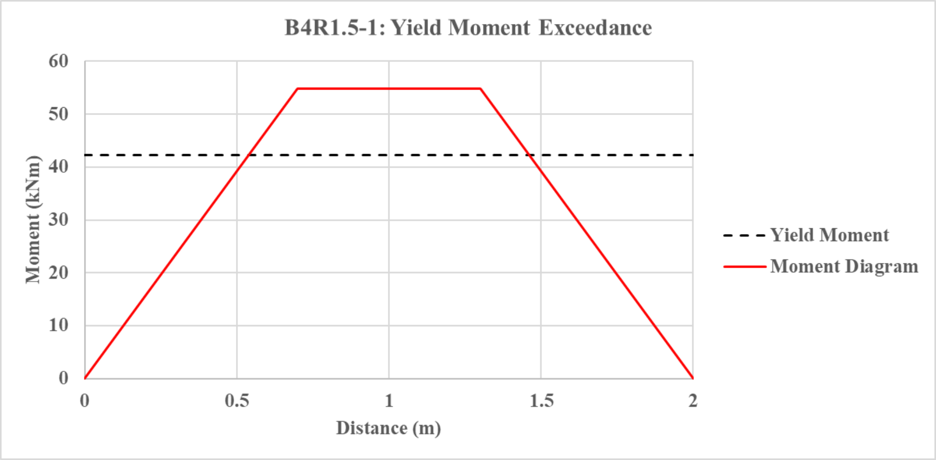

Figure 4-43. B4R1.5-1: Structural Plastic Length

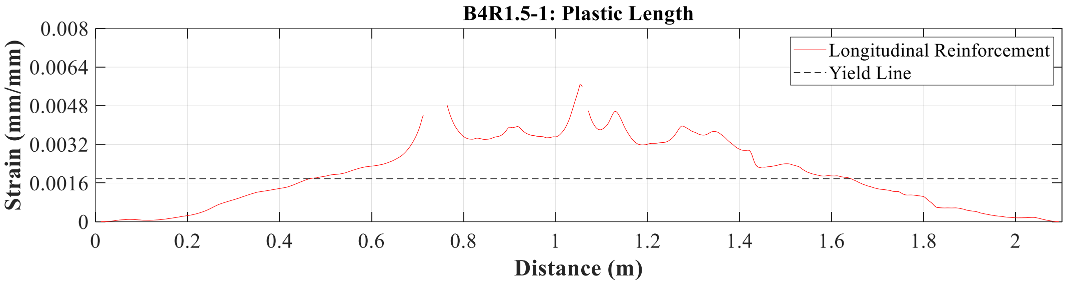

Figure 4-44. B4R1.5-1: Reinforcement Plastic Length

4.3 Discussion

The effect of reducing the fibre content and increasing the steel reinforcement ratio effectively increased the displacement ductility of UHP-FRC beams subjected to four-point loading at the expense of the ultimate load. This is evident in Figure 4-14 which displays the load-deflection response of the beam specimens and Table 4-2 which highlights the change in load and ductility of the beams. B1R2.3-1 exhibited the highest ductility at both peak load and the ultimate response which is defined to be at rupturing of the steel reinforcement. The increase in ductility was found to be a result of the strains in the longitudinal reinforcement being within the plastic range where there is more elongation of the reinforcement for a given increase in stress. Although crushing of the top compressive fibre occurred well before the rupturing of longitudinal reinforcement, there were no severe drops in the load response of the beams. This is consistent behaviour with the work done by Shao & Billington (2022). Specimens B2R2.3-3 and B3R1.5-1 both demonstrated a brittle response after crack localization and the peak load. A single localized crack formed for each both B2R2.3-3 and B3R1.5-1 (Figure 4-16 b) and c)). This single localized crack (Figure 4-16 b)) was the location of the highest strain for B2R2.3-3 Figure 4-26 and can only be inferred as the location of highest reinforcement strain in B3R1.5-3 due to the lack of distributed strain data as evident in Figure 4-27. But since the localized crack was the location of reinforcement rupturing, it is plausible to assume this to be the location of highest reinforcement strain for B3R1.5-1 as well. B3R1.5-1 exhibits an inclined localized crack which initial started vertical, became inclined to midspan, where it became vertical again. Looking at Figure 4-23, it is evident that more load is being applied at the location of the left point load due to a noticeable decrease in compressive strain for all beams under the left point load. In order for an inclined crack to form towards the right load from the bottom of the left load, a compressive strut is required, which is not the case here. Due to this, it is suggested this inclined crack is related to the fibre orientation at midspan of the beam. The beams were cast from the left side, which would have more of a preferential alignment of the fibres. If cored and tested to gather the tensile properties of the material, the location with the most preferential fibre alignment would have the highest tensile strength. The beams did not have stirrups in the constant moment region, but did have adequate stirrups in the shear span. Once the fresh UHP-FRC that was once travelling through a confined space and then entering a region with no confinement the fibre changed, which impacted the growth of the localized crack as seen in Figure 4-16 c).

At the onset of yield as defined by the strain measured by the strain gauge at midspan, it is evident that the yield length varies between specimens. At this stage of loading, the effects of crack formation were not evident due to cracks not propagating to the height of the sensor. The yield length was greatest for B4R1.5-1 and lowest for B2R2.3-3. The reduction in fibre content decreased the tensile strength of UHP-FRC after cracking, reducing the overall contribution of UHP-FRC in tension to tensile force component. This increases the load the longitudinal reinforcement to resist. Higher distributed strains in the longitudinal reinforcement are a result of limited bond strength in the cover; due to this, at yielding, the length at which the longitudinal reinforcement demonstrates yielding increases at a lower reinforcement ratio. This similar behaviour is evident at the peak loading stage. The length at which the strains in the longitudinal reinforcement demonstrate yielding increases with a decrease in fibre content and decrease in reinforcement ratio. This increase in plastic length due to a decrease in fibre content is consistent with the results provided by the tests conducted by Pokhrel et al (2021), where the plastic length of UHP-FRC beams with varying fibre contents was measured with strain gauges. The decrease in bond strength due to a reduction of the tensile strength of UHP-FRC and reduction of bar size enables strain to penetrate into the steel reinforcement away from the cracks, thus increasing the plastic length. Although there is a decrease in plastic length for B1R2.3-1 in comparison to B4R1.5-1, a greater displacement ductility is evident at both ultimate and peak load (Table 4-2). With a slight decrease in plastic length, there is still an increase in displacement ductility. This increase in ductility was a result of the occurrence of more severe increases in the strain gradient in B1R2.3-1 in comparison to B4R1.5-1, with an overall increase in peak strain. The higher strains in B1R2.3-1 induce a greater curvature of $7.98\text{x}10^{-06}$ mm^{-1}, rotation, and thus, displacement of B1R2.3-1 in comparison to B4R1.5-1; increasing the displacement ductility of the B1R2.3-1.

The demand on the compressive strains induced by flexure is highest at a higher reinforcement ratio and fibre content. When taking equilibrium of forces in the x-direction along the cross-sectional height, an increase in the tensile force component due to a greater contribution of concrete in tension occurs, to satisfy equilibrium requirements. Due to crack propagation, as the neutral axis shifts upwards, more so due to lower tensile strengths of UHP-FRC with a reduction of fibre content, the top compressive strain decreases, delaying the onset of crushing. Compressive crushing occurs closest to the peak load for the 3% fibre content specimens, rather than closer to rupturing of steel reinforcement. Since there were no severe drops in the load carrying capacity of B1R2.3-1 and B4R1.5-1 and a lack of spalling due to crushing, the impact of crack localization on tension strain localization had a more pronounced effect of the load carrying capacity of the beams when the material exhibited tension-hardening behaviour. Similar behaviour was exhibited by the UHP-FRC beams tested by Shao & Billington (2019), where they concluded that avoiding failure after crack localization leads to a better utilization of the compressive strength of UHP-FRC.

The midspan strain measured in the DFOS differs from that measured by the strain gauge. The strain difference between the DFOS and strain gauges are a result of increasing curvature as load increases, causing a gradual linear increase in strain difference in time. The effects of curvature on strain are due to the height difference of the attached DFOS and strain gauge. The DFOS was attached to the top of the longitudinal reinforcement, whereas the strain gauge was attached at mid height. Due to this, the curvature is higher at mid height of the bar where the strain gauge is located and lower at the top of the bar where the DFOS is located. The difference in strain when subtracting the DFOS strain from the strain gauge strain nearly follows that obtained from curvature, verifying that the DFOS is accurately measuring strain.

4.4 Summary

The four-point loading beam tests performed on UHP-FRC steel-reinforced beams with varying degrees of fibre content and tension reinforcement ratio, while instrumented with DFOS presented in this chapter demonstrated the following:

- The peak load was highest at a higher v_f of 3% and higher reinforcement ratio of ρ_s=2.3% (B2R2.3-3) with a peak load of 241 kN.
- UHP-FRC beams with a v_f=3% volumetric fibre content demonstrated a brittle failure after crack localization, far before compressive crushing.
- Displacement ductility at peak load increased with a decrease in v_f and an increase in reinforcement ratio (B1R2.3-1) with a peak load ductility of 1.89.
- More localized cracks formed at a lower v_f of 1% in comparison to the single localized crack which formed for v_f=3% fibre content beam specimens, causing more spikes in the strain gradient.
- A decrease in fibre content resulted in bond splitting, in which its effects on strain alleviation in the longitudinal reinforcement was not captured at peak load due to it taking place after failure of the DFOS.
- The plastic length of longitudinal reinforcement is highest at a lower fibre content and reinforcement ratio, which may be the result of a decrease in bond parameters due to a smaller bar diameter and tensile strength of UHP-FRC.
- Overall, lower longitudinal reinforcement strains and top support wire strains were evident at a lower fibre content of $v_{f=}$1%, which delayed the onset of compressive crushing and rupturing of longitudinal reinforcement.
- An overall increase in strain peaks in the longitudinal reinforcement resulted in an increase in curvature which increased the displacement ductility of the beams.
- The plastic length measured by the DFOS was greater than that obtained by the distance where the bending moment in the beam exceeded the yield moment.
- The strain measured by the DFOS and strain gauge are similar, but experience an increase in strain difference over time due to the increase in curvature that induces a higher strain

being measured by the strain gauge due to it being located at mid height of the longitudinal reinforcement in comparison to the DFOS being located at the top of the longitudinal reinforcement.

Chapter 5: Finite Element Modelling of UHP-FRC Beams

Prior to testing the UHP-FRC beams, detailed analysis was undertaken to anticipate the response. The reasons for this study were two-fold – first to support the test setup (expected force magnitudes and expected demands of the instrumentation) but also in order to develop a point of reference for testing the underlying hypothesis used in designing the specimens. This chapter presents the methodology, results, and findings of the finite element model (FEM) of the specimens. To this end, a plane-stress nonlinear finite element analysis was conducted in ATENA-GID. The model is considered a preliminary study in the sense that it provides predictions; it provides a basis for calibration of the important design parameters of the UHP-FRC material (e.g., effect of tensile strength, localization strain, reinforcement ratios, and fracture energy on the strength and mode of failure). This model used the geometry of the beam shown in Figure 5-1.

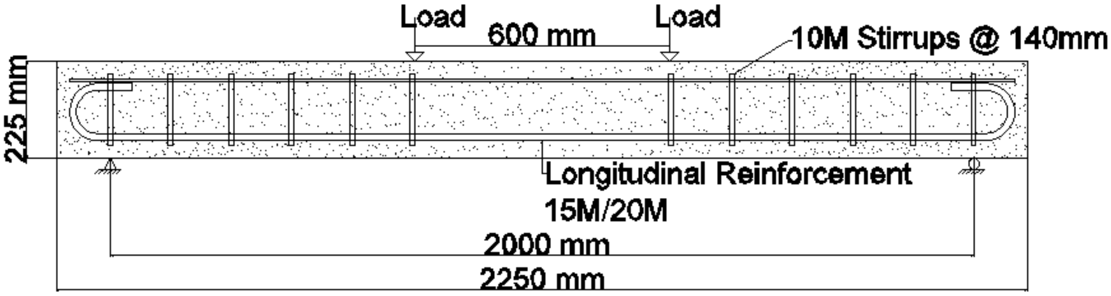

Figure 5-1. Reference Beam for Finite Element Model

5.1 Methodology

The general methodology undertaken to develop the finite element model consisted of defining the geometry of the model using macroelements, inputting material parameters for concrete and steel, defining the boundary and loading conditions considering the symmetry of the model, and defining an appropriate mesh. The following sections will discuss their implementation in detail.

5.1.1 Macroelements

The plane-stress FEM was composed of an assembly of geometrical objects/macroelements as seen in Figure 5-2. These included surface elements for steel loading plates at the support and loading points, 1-dimensional truss elements for transverse and longitudinal reinforcement, and a surface element for the UHP-FRC beam. A half beam was modelled due to the symmetry of the problem and to reduce the computational effort. Loading plates were applied to the model to prevent the influence of load concentrations on compressive crushing due to an applied point load.

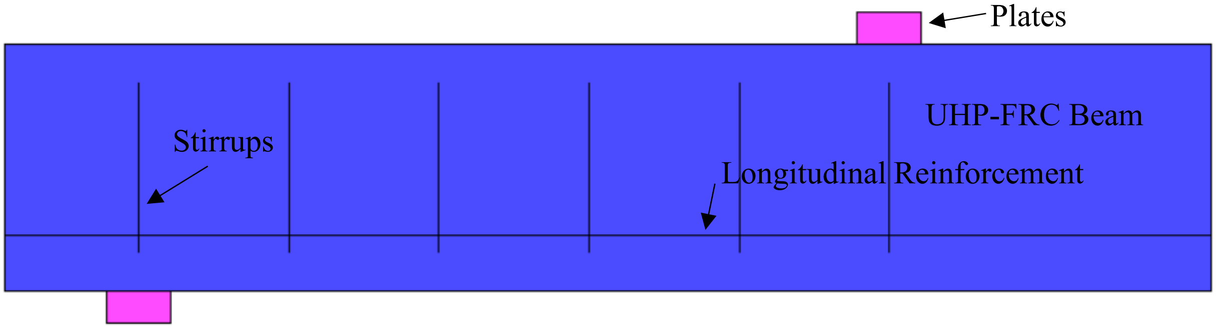

Figure 5-2. Macroelements

5.1.1.1 Material Definition and Input Parameters

The material properties for UHP-FRC as presented in 3.4.5 and 3.5.3 were used as material input parameters for the finite element model. The nominal concrete properties at 28-days were used and are summarized in Table 5-1. These included compressive strength (f’c), elastic modulus (E_c), stress at the onset of crushing/nonlinear behaviour (f'_{co}), fracture energy (G_f) (Figure 5-3 a)), which is the area under the stress-crack width domain, plastic strain at peak compressive strength ($\varepsilon_{pl} = \varepsilon_{co} - f'_c/E_c$) (Figure 5-3 b)), tensile strength (f_{Fu}), critical compressive displacement (w_d) (Figure 5-3 c)), which is the axial shortening at the end of the softening phase in compression, and Poisson’s ratio (ν). It should be noted that a characteristic length (L_c) of 10mm was used for the model. The finite element model utilized a smeared crack approach, where the tensile strains responsible for the crack formation are considered uniformly distributed within a given element. Additionally, a fixed crack model was assumed for the modelling of the beams, where the orientation of cracking is set parallel to the direction of the principle tensile strain when crack initiation takes place. As further loading takes place, this direction remains fixed.

Table 5-1. Concrete Material Properties

Material Property	**3%**	**1%**
f'_c (MPa)	149.1	148.2
f'_{co} (MPa)	9.77	9.73
E_c (MPa)	41100	40703
f_{Fu} (MPa)	12.82	5
G_f (N/mm)	14.32	6.3
ε_{pl} (mm/mm)	0.00077	0.00046
w_d (mm)	0.218	0.182
ν	0.22	0.24

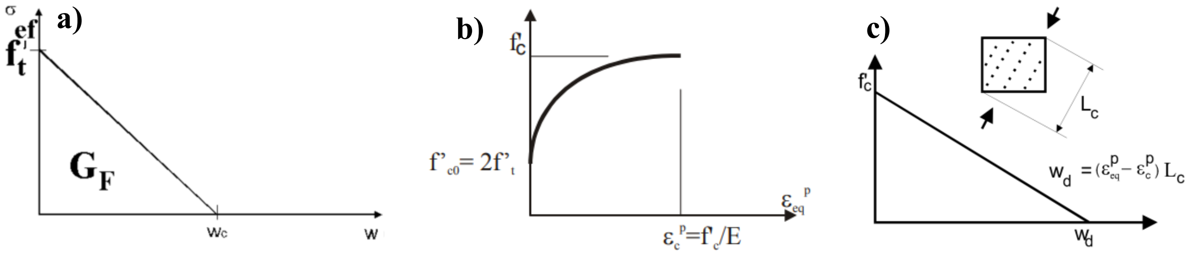

Figure 5-3. a) Fracture Energy, b) plastic strain, and c) Critical Compressive Displacement (Červenka et al., 2021)

The tensile properties of the same UHP-FRC premix with 3% fibres, measured in earlier studies were used in the model. Ralli (2022) conducted flexural tests with inverse analysis on UHP-FRC prisms to obtain the tensile properties for Sika's UP-F3 Poly premix (Figure 5-4) which was used to cast the UHP-FRC beam specimens of this study. In substitution of the 1 % fibre content tensile properties, Shao & Billington (2022) provided the tensile properties of Sika's UP-F2 premix (with $f_{Fu} = 5$MPa, fracture energy value $G_f = 6.3$N/mm, and a localization strain of 0.02mm/mm), which was Sika's proprietary mix prior to its UP-F3 Poly premix.

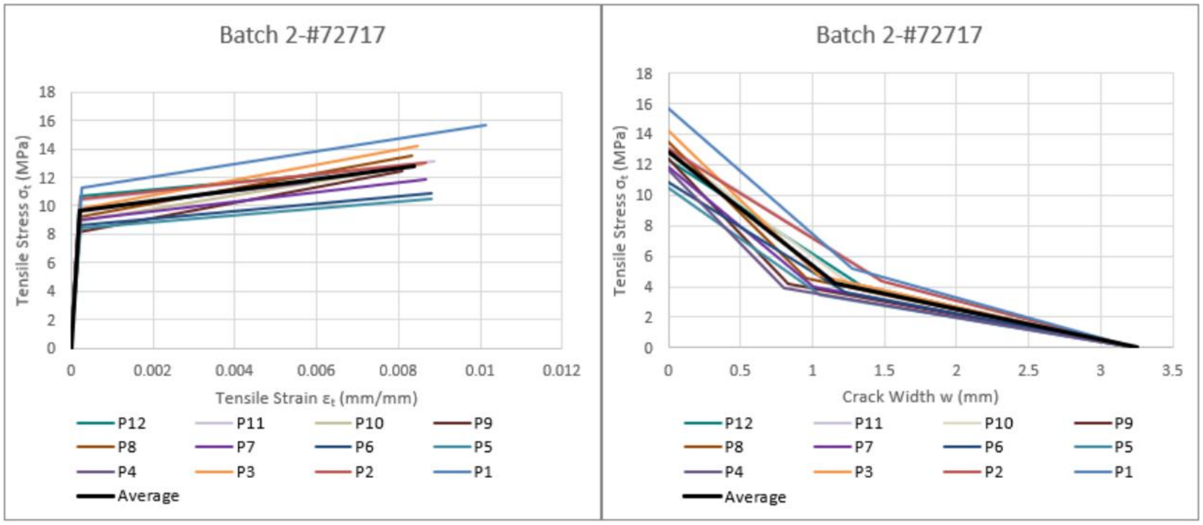

Figure 5-4. Linearized Stress-Strain Curve in Tension (Ralli, 2022)

The transverse and longitudinal reinforcement were defined as 1-dimensional truss elements. Due to the 2-dimensionality of the model, the two longitudinal bars and two vertical legs of the stirrups were modelled using two profiles for the bar diameters. The steel reinforcement properties were input using a multilinear function, with seven linear segments as seen in Figure 5-5 a) and b) for the longitudinal reinforcement. These included one segment in the elastic range, one segment for the yield plateau, four segments to define the strain hardening zone, and one segment for ultimate, which was represented as a plateau. The segments within the strain hardening phase were defined by the average of the strain taken at every quarter between the strain at the onset of strain hardening and the strain at ultimate strength for the three specimens tested per bar size in 3.5.3. Furthermore, the transverse reinforcement was modelled as an elastic-perfectly plastic material, with an elastic modulus of 200GPa and a yield strength of 400MPa. Perfect bond was assumed for the reinforcement, regardless of the fibre content used in each specimen. This assumption implicitly assumes that the bond stress supported by the UHP-FRC cover is significantly high to prevent relative slip of the bars. It should be noted that no area reduction was applied to the modelled reinforcement to account for the loss of area of the reinforcement at midspan due to the installation of strain gauges. Furthermore, the loading plates consisted of solid elastic material properties with and E = 200GPa.

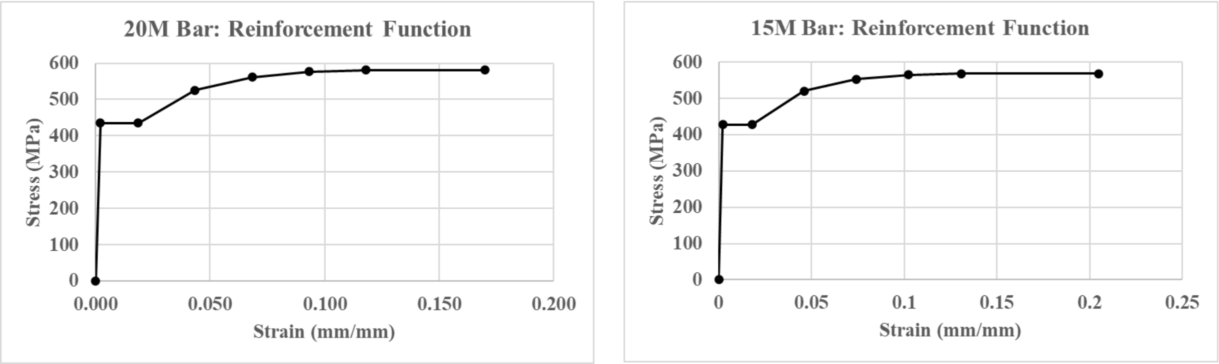

Figure 5-5. Reinforcement Function a) 20M Bar and b) 15M Bar

5.1.1.2 Boundary and Loading Conditions

Figure 5-6 shows the boundary conditions and loading conditions implemented in the finite element model. The boundary conditions were defined according to the symmetry of the experiment. Displacements in the y-direction (u_y) were restrained at central point of the plate, representative of roller behaviour. A line restraint for the x-direction (u_x) was used to set the horizontal displacements along the height of the beam at the vertical line of symmetry at midspan to zero. Fixed line constraints were placed at the interface of the steel plates and the concrete beam using the "master-slave" condition to eliminate the relative deformation between the two macroelements. An incremental displacement with a 0.1mm step size was applied to the model at the central point of the top loading plate. The iterative solution algorithm for the model consisted of the standard Newton-Raphson method with line search. A monitoring point was placed at the location of the applied displacement to record the reaction force and another monitoring point was placed at the bottom corner of the vertical line of symmetry to record the vertical displacement of the model at midspan.

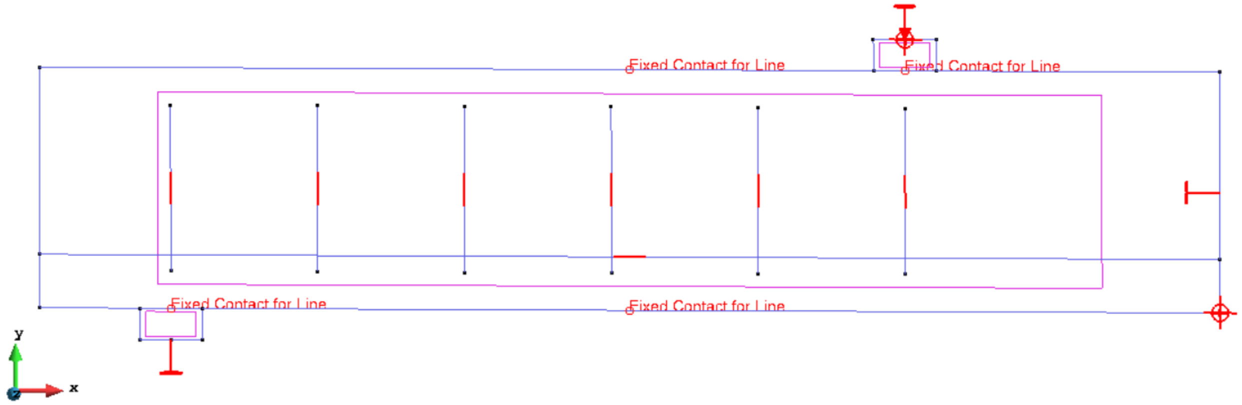

Figure 5-6. Condition Data for FEM Beam Model

5.1.1.3 Mesh Definition

A fine quadrilateral mesh of 10mm x 10mm mesh (element aspect ratio of 1) was used for the beam model as seen in Figure 5-7. This mesh size was used to have at least twenty elements in the smallest direction of the model. The use of a finer mesh in the study was intended to provide detailed description of the expected strain patterns and crack disposition.

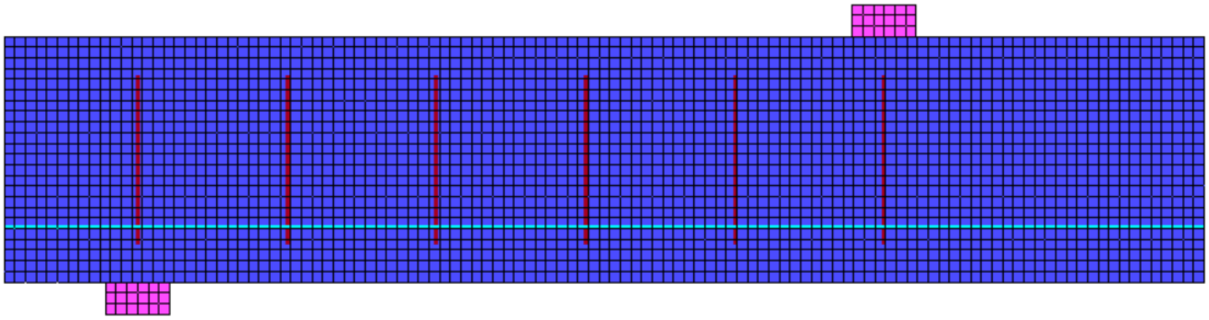

Figure 5-7. Modelled Beam with Mesh

5.1.2 Results

The FEM beams demonstrated similar behaviour in comparison to their experimental counterparts. This was particularly true for the 3% fibre content beams but not the 1% fibre content beams. Figure 5-8 provides the load-deflection response of the FEM beams. B2R2.3-3 and B3R1.5-3 both demonstrated a brittle failure after peak load, with eventual rupturing of the longitudinal reinforcement. B1R2.3-1 and B4R1.5-1 both demonstrated a sustained load after a slight drop in from peak load. Figure 5-9 a) shows that the modelled and experimental responses for B1R2.3-1 are similar up to peak load, but after failure, instead of a gradual decrease in the load carrying capacity of B1R2.3-1, there is a sustained load which was not exhibited in the experimental tests. The same could be said for B4R1.5-1 (Figure 5-9 d)). Both B2R2.3-3 (Figure 5-9 b)) and B3R1.5-3 (Figure 5-9 c)) demonstrated similar behaviour to the experimental beams. There was an overall decrease in load for the numerical beams in comparison to the experimental beams; it is hypothesized that the discrepancy was due to use of the nominal 28-day concrete properties in the analysis instead of the values obtained at the time of testing. The peak loads for the modelled beams B1R2.3-1, B2R2.3-3, B3R1.5-3, and B4R1.5-1 went as follows: 160.5kN, 217.3kN, 183.9kN, and 124.9kN.

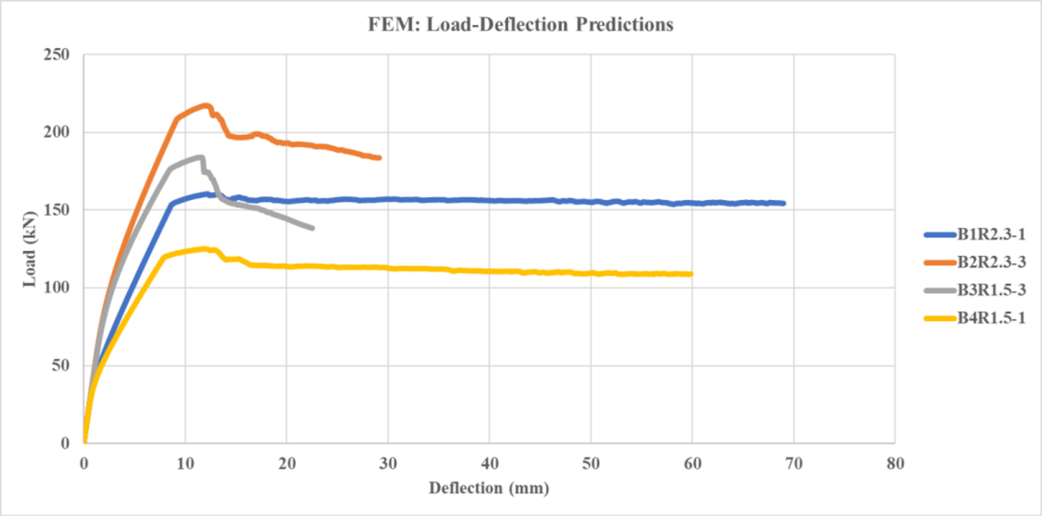

Figure 5-8. FEM: Load-Deflection Predictions

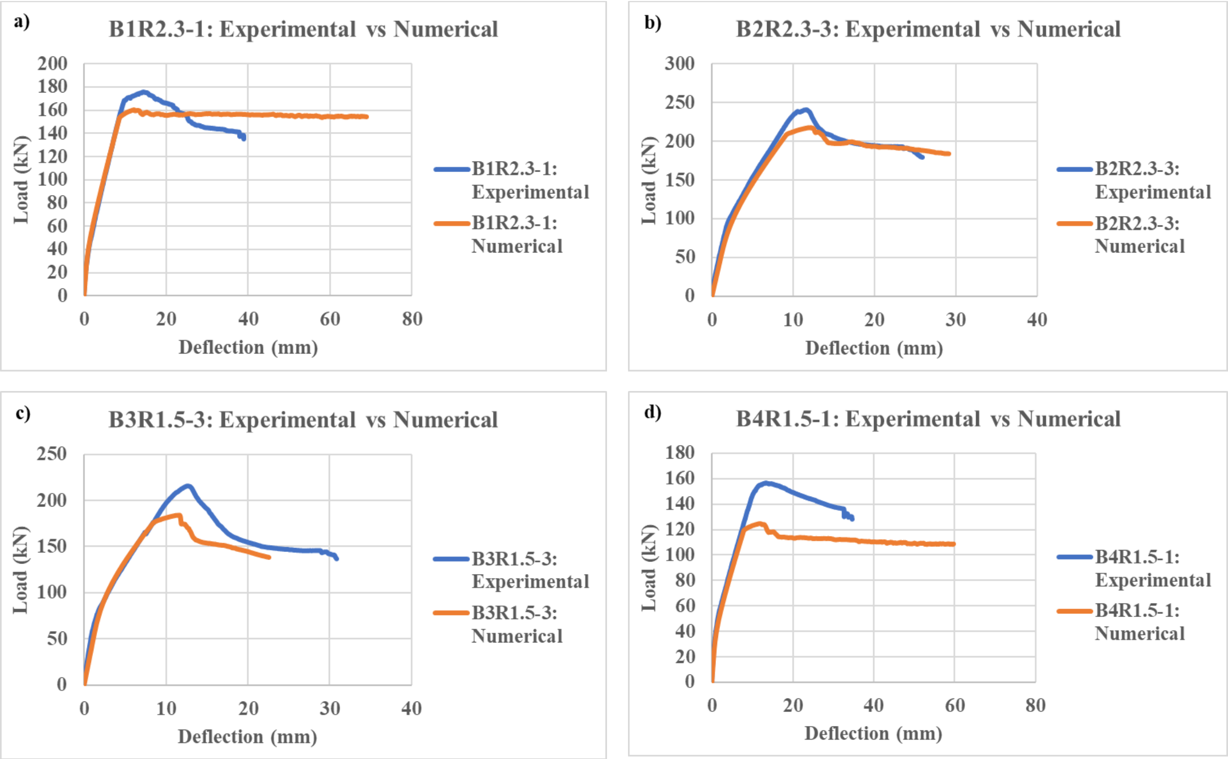

Figure 5-9. Comparison of Experimental and Numerical Results for a) B1R2.3-1, b) B2R2.3-3, c) B3R1.5-3, and d) B4R1.5-1

All four modelled beams demonstrated a localized crack near the applied point load, similar to the experimental beams. Figure 5-10 illustrates the crack patterns at ultimate failure of the beams. B1R2.3-1 (Figure 5-10 a)) and B4R1.5-1 (Figure 5-10 d)) both exhibited side-cracking along the length of the reinforcement. This was not observed in B2R2.3-3 and B3R1.5-3. Furthermore, crushing was evident for all four beams near the locations of the point loads.

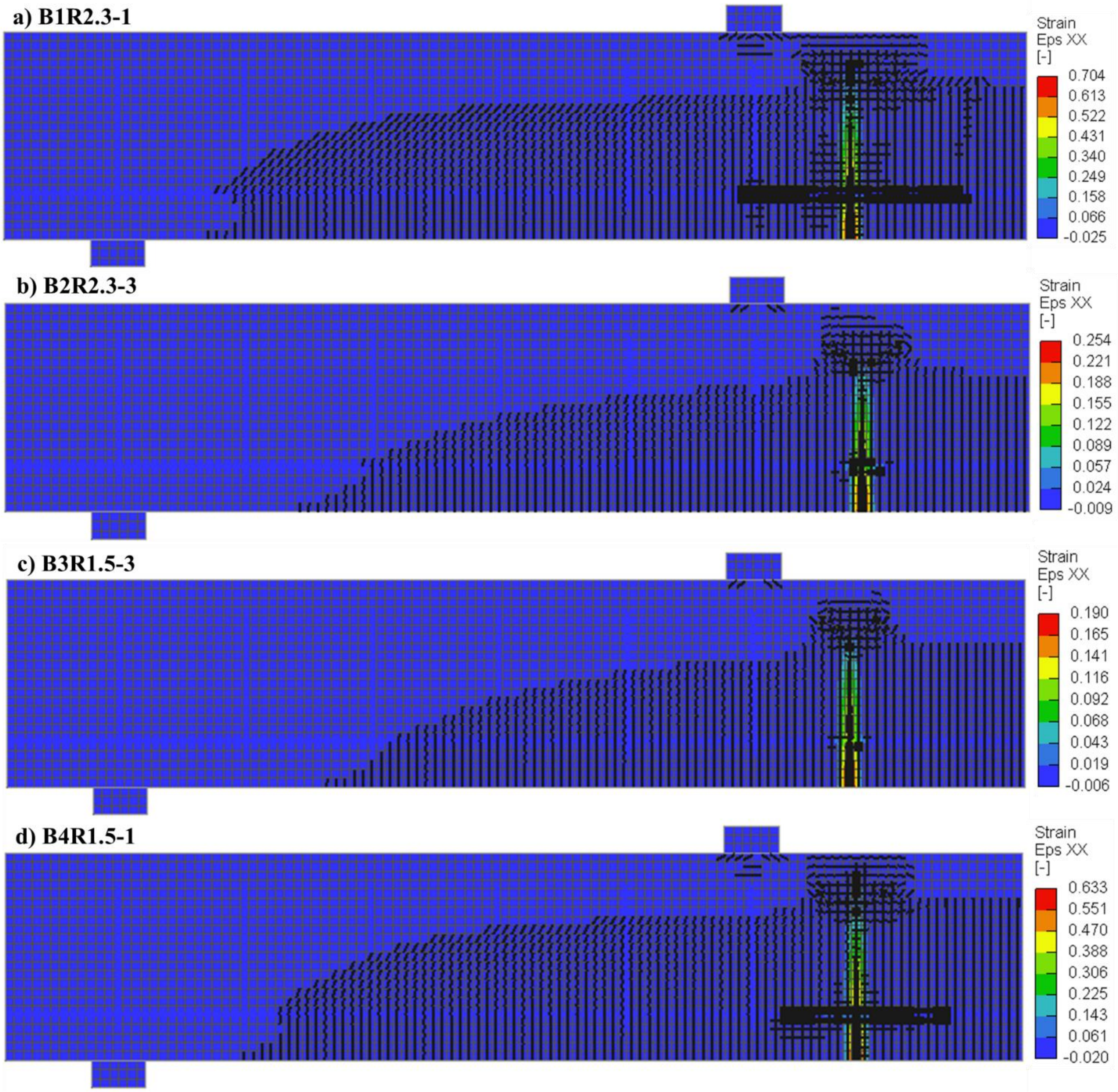

Figure 5-10. Cracking in Modelled Beams at Failure

5.1.3 Discussion

The values of the tensile properties of the UHP-FRC materials had a pronounced effect on the load-deflection response of the modelled beams. It is noted that in the present investigation the tension post cracking resilience of the 1% mix was most likely overestimated when using the results of Shao & Billington (2022) who reported an unrealistically high localization strain of 0.02. For 1% fibers the premix used would most likely exhibit tension softening response. After through cracking and localization of the dominant crack in the tension zone, Specimens B1R2.3-1 and B4R1.5-1 would be expected to demonstrate a loss of strength consistent with the experimental evidence, considering that after loss of tensile strength the load that was shed by the cracked tension zone should be redistributed to the reinforcement. The amount of strength loss would be quantified by comparing the flexural strength provided by the UHP-FRC tension zone, with the flexural strength provided by the reinforcement at yielding, in an identical beam comprising plain concrete in the tension zone. Note that the contributed moment calculated about the centroid of the cross section by the UHP-FRC in the tension zone is estimated as (1/2)×5MPa×150mm×190×0.85×(225-(190/3))mm = 9.7kNm, whereas the flexural strength provided to the beam by the rebars upon yielding (neglecting the action of concrete in tension) is: A_sf_y×0.85×(225-40)=37.4kNm for 20M and 25.1kNm for 15 M bar cases (i.e., a contribution by the UHP-FRC in tension equal to 20% and 27%, respectively of the total estimated resistance). In this calculation, 190mm is the estimated depth of the tension zone upon full penetration of the cracks, 40mm is the concrete cover, and the 1/3 factor accounts for the fact that the tension stress block is approximately triangular along the height. The F.E. calculation estimated a nearly constant resistance for displacements beyond the peak load, after through opening of the localized crack in the tension zone; a finding that is not supported by the experiment – it is believed that this discrepancy is owing to the overly optimistic assumption of tension strain ductility after cracking of the 1% fibre mixes. Note that prior to the peak load, both B1R2.3-1 and B4R1.5-1 demonstrate a similar response to their experimental counterparts, with a similar initial stiffness and cracking load. On the other hand, specimens B2R2.3-3 and B3R1.5-3 both behaved similarly to their experimental counterparts, even with the use of the 28-day nominal properties for UHP-FRC – this may suggest that the concrete strength was not exhausted near failure in these cases and therefore the provided additional material strength was not used. B2R2.3-3 demonstrated the highest load of 212kN where B4R1.5-1 demonstrated the lowest load of 121kN. Furthermore, B1R2.3-1 exhibited the greatest displacement ductility.

The crack patterns displayed in Figure 5-10 are similar to those demonstrated by the experimental beams, with a localized crack occurring near the location of the applied point load. The modelled B2R2.3-3 and B3R1.5-3 do not demonstrate any inclined cracks like their experimental parts. The formation of cracking along the longitudinal reinforcement signified splitting of the concrete cover, thus enabling spreading and penetration of strain over a large part of the central region of the specimens and beyond the loading points. Splitting of the cover in the underside of the beams with 1% fiber content could not be reproduced in the plane-stress model; however, side-cracking effectively represents the same type of behavior – cover splitting enables spreading of bar strains over large segments leading larger deflections and therefore a more compliant, ductile response. A corollary to this is that in the absence of strain penetration, localization of strain would limit the deflection and accelerate bar rupture.

Further calibration of the finite element models would be required to interpret the experimental responses obtained from the beam tests. Three-dimensional modelling would be a first priority in order to be able to reproduce the splitting of cover in the underside of the beams, whereas the obtained stress-strain models would be updated to the experimental mean values at the time of testing.

5.1.4 Conclusions

The finite element modelling of the UHP-FRC beam specimens provided predictions of beam behaviour with nominal 28-day properties. The following can be summarized in this section:

- The nominal 28-day properties provide a conservative response of beam behaviour – since the beams were tested past the 28-day limit.
- The tensile properties used to model the 1% fibre content beam specimens were not sufficient and require further investigation and/or material characterization tests to generate the appropriate material properties of the 1% UHP-FRC mix.
- Similar trends in behaviour demonstrated in the experimental beams were evident in the modelled beams, with the 3% fibre content specimens exhibiting a brittle response and the 1% fibre content specimens demonstrating a more ductile response. Furthermore, B2R2.3-3 demonstrated the highest peak load and B4R1.5-1 demonstrated the lowest peak load.
- The peak loads for the modelled beams B1R2.3-1, B2R2.3-3, B3R1.5-3, and B4R1.5-1 went as follows: 160.5kN, 217.3kN, 183.9kN, and 124.9kN; with the corresponding percent differences of 8.8%, 9.8%, 14.7%, and 20.3%.
- Bond splitting was evident along the longitudinal reinforcement for B1R2.3-1 and B4R1.5-1 which resulted in a near constant load with increasing displacement.

- Crack patterns in the modelled beams were similar to those observed in the experimental beams, with a localized crack forming near the applied point load. The inclined cracks demonstrated by B2R2.3-3 and B3R1.5-3 were not reproduced by the model.
- Further modelling of the beams using the test-day material properties of the UHP-FRC material is required to improve the model, so it is more representative of the experimental testing of the UHP-FRC beams.
- Revision of the F.E. model to account for the 3-dimensionality of the problem and to conduct a sensitivity study that would identify the effect of material tension hardening or tension softening characteristics in the overall response of the structural component are the highest priority for future research.

Chapter 6: Conclusions, Challenges, and Future Work

The work presented in this thesis aimed to study the flexural response and the effects of reinforcement in the form of bars and distributed fibers on the flexural behavior and mode of failure of slender beams. Two factors differentiate the behavior of UHP-FRC structural components from that of identically reinforced beams of conventional concrete. These are, a) the significantly higher bond strength provided by the UHP-FRC cover on the bars and b) the participation of the concrete in the tension zone to sectional equilibrium. The high bond enables development of bar stresses over very short distances; this means that strain penetration away from cracks is significantly mitigated particularly in the case of mixes that demonstrate tension hardening behaviour after cracking (usually fibre contents ≥ 2% are needed for this type of response).

The results of the investigation provide insights regarding the extent of strain penetration and the spread of plasticity in the longitudinal reinforcement of UHP-FRC beams undergoing four-point loading with varying fibre contents and reinforcement ratios using optical fibres, DFOS. This required the installation of DFOS along the longitudinal reinforcement and top support wire, the casting of UHP-FRC beam specimens and companion specimens, conducting four-point loading beam tests, and conducting a finite element analysis of the beam specimens in order to predict their behaviour and to develop a preliminary finite element model which could be used to do a parametric study by varying the tensile parameters of UHP-FRC. Many challenges occurred during the execution of the experimental program including the non-functioning fibre interrogation system ODiSI-B and the persistent damage to the DFOS. Complete understanding and interpretation of the results will be further assisted by the completion of some outstanding tension characterization experiments as well as the completion of processing of DIC data collected during the tests. The findings of this thesis could be incorporated in other research projects consisting of UHP-FRC structural members and inform the formation of design provisions for design of structural components in flexure.

6.1 Summary of the Thesis

This thesis primarily focused on the effect of varying fibre content and reinforcement ratio on the displacement ductility of UHP-FRC beams in flexure. It utilized DFOS to measure the distributed reinforcement strains along the longitudinal reinforcement and top support wire. This was to generate insights regarding the spread of inelastic strains in the reinforcement, the distribution of curvatures along the length of the beams, and the shifting of the neutral axis between cracked and uncracked sections. This was conducted to study the condition of the longitudinal reinforcement and the relationship between the strains measured with the DFOS, calculated curvature, and displacement ductility of the beams. A greater displacement ductility was not necessarily due to an increase in plastic length, but more so due to a higher overall peak strain and average curvature. B1R2.3-1 demonstrated the highest peak strain, average curvature, and displacement ductility; B2R2.3-3 exhibited the highest peak load and most brittle response; B3R1.5-3 consisted of a lack of strain data along the longitudinal reinforcement limiting any valuable findings from the measured distributed strain; and B4R1.5-1 demonstrated the largest plastic length.

Finite element analysis was conducted for each of the four beam specimens in order to predict the behaviour of the beams using the nominal 28-day properties of UHP-FRC in tension and compression. The finite element models demonstrated a similar load-deflection response for B2R2.3-3 and B3R1.5-3 as they consisted of the material properties in tension and compression corresponding to the UHP-FRC material used in casting the beams. The same was not evident for B1R2.3-1 and B4R1.5-1, as the tension properties of the material for 1% fibre ratio and the same premix reported in the literature do not consistently estimate the post-cracking softening characteristic of lightly reinforced mixes – which has been reported to occur in characterization studies of similar fibre content ratios of UHP-FRC. Overestimating the tensile strain resilience of the material led to an inaccurate load-deflection response for B1R2.3-1 and B4R1.5-1. Similar cracking was exhibited in all of the four beams with a localized crack forming near the location of the applied point load, but the correct inclination of the crack was not captured in the model.

6.2 Conclusions

6.2.1 Material Characterization of UHP-FRC

Decreasing the volumetric fibre content had a minimal effect on compressive strength, crushing strain, and elastic modulus, but had a noticeable affect on Poisson’s ratio. The inclusion of fibres slightly increased the mean compressive strength from 148 MPa to 149 MPa when transitioning from a 1% fibre content to a 3% fibre content. Similarly, the elastic modulus demonstrated a slight increase from a 1% fibre content to a 3% fibre content, increasing the stiffness of the material from 40703 MPa to 41100 MPa. Furthermore, the compressive ductility of the material increased from an ultimate strain of 0.0041 to 0.0044, moderately exceeding the assumed design value in most design codes of 0.0035. Finally, due to the confinement effects induced by the steel fibres, lower lateral dilation was evident for the 3% fibre-content cylinders, reducing Poisson's ratio from 0.24 to 0.22. The effect of fibres on UHP-FRC in compression was evident, but minimal.

6.2.2 Effect of Fibre Content and Reinforcement Ratio on the Flexural Response of UHP-FRC Beams

It was observed that a reinforcement ratio of 2.3% and fibre content of 1% led to a more deformable response of UHP-FRC beams in flexure. This was concluded due to the displacement ductility of B1R2.3-1 being the highest of all the beams, with a value of 1.89 at peak load and 5.09 at the ultimate condition which was defined at the rupturing of longitudinal reinforcement. B2R2.3-3, which consisted of the same reinforcement ratio, but higher fibre content demonstrated the lowest displacement ductility, but the highest peak load of 241 kN. Both B2R2.3-3 and B3R1.5-3 exhibited a brittle failure nearly after crack localization and the peak load. Whereas B1R2.3-1 and B4R1.5-1 exhibited gradual strain hardening after crack localization, the zone at which larger axial strains occur at lower stresses in the longitudinal reinforcement, leading to greater deflections. More localized cracking was evident at a lower fibre content for both B1R2.3-1 and B4R1.5-1, which exhibited two localized cracks under the locations of the applied point load. A single localized crack was evident for both B2R2.3-3 and B3R1.5-3, both of which were inclined possibly due to fibre alignment in the UHP-FRC matrix. Furthermore, failure of the concrete cover was evident for both B1R2.3-1 and B3R1.5-1, with splitting occurring at the bottom side of the beams within the constant moment region. Compressive crushing did not result in any severe drops in the load carrying capacity of the beams in comparison to crack localization and rupturing of longitudinal reinforcement. In general, a lower fibre content and higher reinforcement ratio led to a more ductile response of UHP-FRC beams in flexure.

6.2.3 Spread of Plasticity for Varying Fibre Contents and Reinforcement Ratios

Distributed strains along the longitudinal reinforcement and top support wire were measured with DFOS. Issues were encountered with B3R1.5-3 due to the presence of severe scattering and lack of reliable strain data. The data obtained by the DFOS was used to generate insights regarding the spread of inelastic strain, distributed curvature, and shifting of the neutral axis along the beam length. It was evident that lower fibre content and lower reinforcement ratio led to a greater plastic length, with B4R1.5-1 demonstrating a plastic length of 1177.8 mm. B2R2.3-3 exhibited the lowest plastic length of 923 mm. B1R2.3-1 exhibited the highest observed peak strain of 0.00755 mm/mm. More spikes in the strain gradient were evident for both B1R2.3-1 and B4R1.5-1, with B1R2.3-1 demonstrating the occurrence of a larger number of cracks owing to the lower tensile stress and bond strength. However, even though B4R1.5-1 had the longest plastic length, it did not demonstrate the greatest displacement capacity. Since B1R2.3-1 had more pronounced increases in the strain gradient, this resulted in greater overall curvatures along the length of the beams. Due to this, the average curvature was highest for B1R2.3-1, with a value of $7.98\text{x}10^{-6}$ mm^{-1}. This would then lead to greater rotations and thus larger deflections. There was a noticeable difference in the strain measured by the DFOS and the strain gauge at midspan. This was due to the DFOS being installed on top of the longitudinal bar and the strain gauge being installed at mid-height. As the beam test continued, the difference in strain between the DFOS would increase, with the DFOS measuring smaller strain values at midspan in comparison to the strain gauge. This was a result of the height difference and curvature, which caused the difference in strain between the two instruments, at greater deflections. The strain difference measured by subtracting the DFOS measured strain from strain gauge strain and the strain difference induced by curvature follow a similar linear trending. Due to this consistent trend, it was determined that the DFOS and strain gauge would measure similar strains if installed at the same height.

6.2.4 Finite Element Modelling of UHP-FRC Beams

A finite element analysis was conducted for the four beam specimens in order to predict the behaviour of the experimental beams using nominal properties. Overall, the finite element models for B2R2.3-3 and B3R1.5-3 demonstrated similar behaviour to their experimental counterparts but were more brittle with a lower load capacity. Regarding B1R2.3-1 and B4R1.5-1, the load-deflection response was similar to that of the experimental beams up until the peak load, whereas a load plateau occurred with an increase in deflection. This was due to splitting which resulted from the weaker tensile strength used as input in the model. Splitting caused the longitudinal reinforcement to exhibit strains within the yield plateau, causing a near constant load for an increase in deflection. The lack of tensile data from direct tension characterization tests to be used as input in the finite element model proved to be an issue, due to the questionable material properties collected from the literature and used in the model. Furthermore, due to the 28-day nominal properties of the UHP-FRC material and the beam tests taking place nearly six months after casting, the results in the finite element model would not be representative of the experimental testing which took place. Improvements in the finite element models are required to provide accurate results which correlate better those of the experimental beams. This requires different approach to meshing the specimens (e.g., a 3-D model), a better representation of the bar (as a solid) including the rib profiles, and modelling of bond along the bars and concrete (particularly relevant for the top auxiliary bars which had a smooth profile). Also critical is the correct representation of the material stress-strain laws – particularly in tension - extracted from pertinent characterization tests for the mixes studied.

6.3 Challenges

Several challenges accompanied the research presented in this thesis. Most notable issues include:

- The inability to test UHP-FRC prisms under direct tension due to a faulty testing fixture which would crush the specimens at the grips, not demonstrating the appropriate behaviour of the specimens. This resulted in the lack of tensile material properties to be used in the finite element model, leading to use of reported values for the same premix from the literature.
- The ability to achieve the post-peak behaviour of UHP-FRC in compression was quite challenging due to the inadequate stiffness of the Controls Automax. Only few tests were able to measure the post-peak behaviour with reliance on the displacement of the actuator head to determine strain due to failure of the strain gauges attached to the cylinder specimens.
- The installation of DFOS along steel reinforcement proved to be challenging due to their propensity to damage. For instance, typical wire ties could not be used in assembling the reinforcement cage, due to the wires cutting into the DFOS, fracturing the sensor. Additionally, the placement of the DFOS had an impact on the distributed strain readings, with the DFOS being installed along the longitudinal rib, which led to differences in the strain measured by the strain gauge at midspan and the DFOS. Furthermore, casting UHP-FRC with DFOS attached to rebar could also lead to damage of the sensor or tugging of the loose portion of the sensors due to the high flowability of UHP-FRC.

- Ensuring a preferential fibre alignment in UHP-FRC beam specimens is difficult even when pouring the fresh UHP-FRC from one side of the formwork. Therefore, the fibre alignment in the beams could not mimic the fibre alignment used in specimens of characterization tests, owing to the presence of steel reinforcement and the cross-sections of the formwork.
- The fibre-optic interrogator ODiSI-B malfunctioned due to a non-functioning motor. This caused great delays in the attempt to resolve the malfunction before we transitioned to the ODiSI-6104, which provided improved strain readings.

6.4 Future Work

Future tests will be conducted to improve the confidence in the material properties – particularly the tensile response - of the UHP-FRC mixes used in the beams. Further finite element modelling is required to improve the calibration of the beam models as a prerequisite for conducting the necessary parametric analysis. This parametric analysis would consist of manipulating the tensile properties of UHP-FRC and analysing their effect on the load-deflection response under four-point loading, including the deformation capacity, and the spread of inelastic strains over the longitudinal reinforcement, and crack distribution.

The effect of varying plasticity and reinforcement ratio is not limited to beams undergoing four-point loading but can also be applied to columns undergoing lateral and axial loading. The interaction between reinforcement ratio, fibre content, and axial load ratio could be studied with the use of DFOS and generate insights regarding development of bar inelasticity in the tension resilient cover presented by the UHP-FRC matrix. Furthermore, due to the intrinsic confinement effects induced by the fibres, DFOS could also be installed on transverse reinforcement to study the load demand of stirrups with varying degrees of reinforcement ratio and fibre content. Possible findings could provide insights regarding the transverse reinforcement quantities required in the shear design of columns undergoing axial and transverse loading.

References

AASHTO T397. (2022). *Standard Method of Test for Uniaxial Tensile Response of Ultra-High Performance Concrete*.

Abed, M. A., Alkurdi, Z., Kheshfeh, A., Kovács, T., & Nehme, S. (2021). Numerical evaluation of bond behavior of ribbed steel bars or seven-wire strands embedded in lightweight concrete. *Periodica Polytechnica Civil Engineering*, *65*(2), 385–396. https://doi.org/10.3311/PPci.16689

ACI 239. (2018). *Emerging Technology Report (ETR) The Structural Design of Ultra-High*.

AFNOR NF P 18-470. (2016). *French Standard: Concrete — Ultra-high performance fibre reinforced concrete — Specifications, performance, production and conformity*.

AFNOR NF P 18-710. (2016). *French Standard: National addition to Eurocode 2-Design of concrete structures: specific rules for Ultra-High Performance Fibre-Reinforced Concrete (UHPFRC)*.

Ahmed, T., Elchalakani, M., Karrech, A., Dong, M., Mohamed Ali, M. S., & Yang, H. (2021). ECO-UHPC with High-Volume Class-F Fly Ash: New Insight into Mechanical and Durability Properties. *Journal of Materials in Civil Engineering*, *33*(7). https://doi.org/10.1061/(asce)mt.1943-5533.0003726

Akeed, M. H., Qaidi, S., Ahmed, H. U., Emad, W., Faraj, R. H., Mohammed, A. S., Tayeh, B. A., & Azevedo, A. R. G. (2022). Ultra-high-performance fiber-reinforced concrete. Part III: Fresh and hardened properties. *Case Studies in Construction Materials*, *17*. https://doi.org/10.1016/j.cscm.2022.e01265

Amran, M., Huang, S. S., Onaizi, A. M., Makul, N., Abdelgader, H. S., & Ozbakkaloglu, T. (2022). Recent trends in ultra-high performance concrete (UHPC): Current status, challenges, and future prospects. In *Construction and Building Materials* (Vol. 352). Elsevier Ltd. https://doi.org/10.1016/j.conbuildmat.2022.129029

ASTM 1856/1856M-17. (2017). Standard Practice for Fabricating and Testing Specimens of Ultra-High Performance Concrete. *American Society for Testing and Materials*. https://doi.org/10.1520/C1856_C1856M-17

ASTM C469/C469M-10. (2010). Standard Test Method for Static Modulus of Elasticity and Poisson's Ratio of Concrete in Compression. *American Society for Testing and Materials*. https://doi.org/10.1520/C0469_C0469M-10

ASTM E8/E8M-16. (2016). Standard Test Methods for Tension Testing of Metallic Materials. *American Society for Testing and Materials*. https://doi.org/10.1520/E0008_E0008M-16

Berrocal, C. G., Fernandez, I., & Rempling, R. (2021). Crack monitoring in reinforced concrete beams by distributed optical fiber sensors. *Structure and Infrastructure Engineering*, *17*(1), 124–139. https://doi.org/10.1080/15732479.2020.1731558

Červenka, V., Jendele, L., & Prague, J. Č. (2021). *ATENA Program Documentation Part 1 Theory*.

Chao, S.-H., Kaka, V., & Shamshiri, M. (2019). *Toward A Non-Prestressed Precast Long-Span Bridge Girder Using UHP-FRC*.

Chao, S.-H., & Naaman, A. (2010). *Local bond stress-slip models for reinforcing bars and prestressing strands in high-peformance fiber-reinforced cement composites*. https://www.researchgate.net/publication/286810030

CSA A23.1:19 Annex U. (2019). Ultra-High-Performance Concrete, Annex-U. *Canadian Standards Association*.

CSA S6:19 Annex A8.1. (2019). Canadian Highway Bridge Design Code. *Canadian Standards Association*.

CSA S6:19 Annex A8.1 Commentary. (2019). Canadian Highway Bridge Design Code. *Canadian Standards Association*.

Culshaw, B., & Kersey, A. (2008). Fiber-optic sensing: A historical perspective. *Journal of Lightwave Technology*, *26*(9), 1064–1078. https://doi.org/10.1109/JLT.0082.921915

FHWA. (2018). *Properties and Behavior of UHPC-Class Materials - FHWA-HRT-18-036.*

fib. (2010). *fib Model Code for Concrete Structures*.

Graybeal, B. A. (2006). *Material Property Characterization of Ultra-High Performance Concrete*.

Graybeal, B. A. (2013). *Ultra-High Performance Concrete: A State-of-the-Art Report for the Bridge Community*. https://www.researchgate.net/publication/259438585

Graybeal, B. A., & Baby, F. (2013). Development of Direct Tension Test Method for Ultra-High-Performance Fiber-Reinforced Concrete. In *ACI Materials Journal* (Vol. 110, Issue 2).

Habel, K. (2004). *STRUCTURAL BEHAVIOUR OF ELEMENTS COMBINING ULTRA-HIGH PERFORMANCE FIBRE REINFORCED CONCRETES (UHPFRC) AND REINFORCED CONCRETE*.

Hung, C.-C., El-Tawil, S., & Chao, S.-H. (2021). A Review of Developments and Challenges for UHPC in Structural Engineering: Behavior, Analysis, and Design. *Journal of Structural Engineering*, *147*(9). https://doi.org/10.1061/(asce)st.1943-541x.0003073

Husain, S. A. B. (2021). *Characterization of UHPFRC Materials for Bridge Construction: An Opportunity to Offset the Need for Prestressing in Bridge Decks*.

Lee, S.-C., Cho, J.-Y., & Vecchio, F. J. (2013). Tension-Stiffening Model for Steel Fiber-Reinforced Concrete Containing Conventional Reinforcement. In *ACI Structural Journal* (Vol. 110, Issue 4).

Market and Markets. (2022). *Concrete Restoration Market | Global Industry Size Forecast*. https://www.marketsandmarkets.com/Market-Reports/concrete-restoration-market-198206216.html#utm_source=LINKEDIN-NL&utm_medium=KS-2023

Micron Optics. (n.d.). *Optical Fiber Sensors Guide*.

Miller, S. A., Horvath, A., & Monteiro, P. J. M. (2018). Impacts of booming concrete production on water resources worldwide. *Nature Sustainability*, *1*(1), 69–76. https://doi.org/10.1038/s41893-017-0009-5

Pelecanos, L., Soga, K., Elshafie, M. Z. E. B., de Battista, N., Kechavarzi, C., Gue, C. Y., Ouyang, Y., & Seo, H.-J. (2018). Distributed Fiber Optic Sensing of Axially Loaded Bored Piles. *Journal of Geotechnical and Geoenvironmental Engineering*, *144*(3). https://doi.org/10.1061/(asce)gt.1943-5606.0001843

Pokhrel, M., Shao, Y., Billington, S., & Bandelt, M. J. (2021). Effect of Fiber Content Variation in Plastic Hinge Region of Reinforced UHPC Flexural Members. *RILEM Bookseries*, *30*, 1042–1055. https://doi.org/10.1007/978-3-030-58482-5_92

Poldon, J. J., Hoult, N. A., & Bentz, E. C. (2021). Understanding reinforcement behavior using distributed measurements of shear tests. *ACI Structural Journal*, *118*(3), 255–266. https://doi.org/10.14359/51730537

Popovics, J. S. (2008). *ACI-CRC Final Report A Study of Static and Dynamic Modulus of Elasticity of Concrete*.

Ralli, Z. (2022). *Report on Tensile & Flexural Characterization of Sika UHPFRC per CSA S6 and ASTM1609ASTM1609*. http://civil.lassonde.yorku.ca/

Shao, Y., & Billington, S. L. (2019a). *Utilizing Full UHPC Compressive Strength in Steel Reinforced UHPC Beams*.

Shao, Y., & Billington, S. L. (2019b). *Utilizing Full UHPC Compressive Strength in Steel Reinforced UHPC Beams*.

Shao, Y., & Billington, S. L. (2022). Impact of UHPC Tensile Behavior on Steel Reinforced UHPC Flexural Behavior. *Journal of Structural Engineering*, *148*(1). https://doi.org/10.1061/(asce)st.1943-541x.0003225

Shehab El-Din, H. K., Mohamed, H. A., Abd El-HakKhater, M., Ahmed, S., Abd El-Hak Khater, M., of Reinforced Concrete, P., & Professor, A. (2016). *Effect of Steel Fibers on Behavior of Ultra High Performance Concrete*.

Voss, M. S., Riding, K. A., Asce, M., Raid, ;, Alrashidi, S., Christopher, ;, Ferraro, C., & Hamilton, H. R. (2022). *Comparison between Direct Tension, Four-Point Flexure, and Simplified Double-Punch Tests for UHPC Tensile Behavior*. https://doi.org/10.1061/(ASCE)MT.1943

Wight, J. K., & MacGregor, J. G. (2012). *Reinforced Concrete Mechanics and Design, 6th Edition*.

Wille, K., El-Tawil, S., & Naaman, A. E. (2014). Properties of strain hardening ultra high performance fiber reinforced concrete (UHP-FRC) under direct tensile loading. *Cement and Concrete Composites*, *48*, 53–66. https://doi.org/10.1016/j.cemconcomp.2013.12.015

Wu, Z., Shi, C., He, W., & Wu, L. (2016). Effects of steel fiber content and shape on mechanical properties of ultra high performance concrete. *Construction and Building Materials*, *103*, 8–14. https://doi.org/10.1016/j.conbuildmat.2015.11.028

Yang, J., Chen, B., Su, J., Xu, G., Zhang, D., & Zhou, J. (2022). Effects of fibers on the mechanical properties of UHPC: A review. In *Journal of Traffic and Transportation Engineering (English Edition)* (Vol. 9, Issue 3, pp. 363–387). Chang'an University. https://doi.org/10.1016/j.jtte.2022.05.001